2021

Analysis of Shallow Water Underwater Noise from Marine Pile Driving Using Computational Fluid Dynamics and Empirical Data Fitting

Moses Bosco
n01460940@unf.edu

ANALYSIS OF SHALLOW WATER UNDERWATER NOISE FROM MARINE PILE DRIVING USING COMPUTATIONAL FLUID DYNAMICS AND EMPIRICAL DATA FITTING

By

MOSES JOHN BOSCO

A THESIS PRESENTED TO THE GRADUATE SCHOOL
OF THE UNIVERSITY OF NORTH FLORIDA IN PARTIAL FULFILLMENT
OF THE REQUIREMENTS FOR THE DEGREE OF
MASTER OF SCIENCE IN CIVIL ENGINEERING

UNIVERSITY OF NORTH FLORIDA

2021

To my mother Adelaida for her unconditional love and support.

ACKNOWLEDGMENTS

I would firstly like to thank my supervisor, Dr. Raphael Crowley for his guidance, support and assistance in accomplishing my thesis and throughout my graduate degree. His help and support were of paramount importance to the accomplishment of this work.

I would also like to thank Dr. Bill Dally, Amanda Schaaf, Dillon Sypulla and Brandon Rivera and Ian Gstalder for all their help in facilitating and during field data collection. Lastly, I would like to thank Dr. Donald Resio for his support and continued dedication as director of the Taylor Engineering Research Institute. Thank you all.

TABLE OF CONTENTS

page

LIST OF TABLES

LIST OF FIGURES

Abstract of ThesisPresented to the Graduate School
of the University of North Florida in Partial Fulfillment of the
Requirements for the Degree of Master of Science in Civil Engineering

ANALYSIS OF SHALLOW WATER UNDERWATER NOISE FROM MARINE PILE DRIVING USING COMPUTAITONAL FLUID DYNAMICS AND EMPIRICAL DATA FITTING

By

Moses John Bosco

December 2021

Chair: Raphael Crowley
Major: Civil Engineering

There has been a growing concern in recent years about the effects of anthropogenic noise due to pile driving on underwater wildlife. Current guidelines for mitigating hydroacoustic effects associated with these geotechnical events are based upon a relatively simple transmission loss formulation known as the Practical Spreading Loss Model (PSLM). This model is easy to implement, but it may produce overly conservative results. Sound data during pile drives from several sites in Florida showed much higher sound attenuation than predicted by the PSLM. The first part of this study focused on explaining this discrepancy using computational fluid dynamics. Specifically, synthetic pile drives were simulated using Siemens' Star-CCM+. These models tracked sound decay from a single hammer blow that was imposed on a modeled pile using site-specific bathymetry data. Results showed that discrepancies between measured transmission loss coefficients and the PSLM could not be explained due to local bathymetry alone. However, if different sound absorption criteria were used at the sites' mudlines, the model was able to replicate results. The data therefore suggest that geotechnical conditions may play a significant role in determining anthropogenic sound loss due to pile driving.

The second part of the study focused on using empirical data fitting to calibrate a physics based semi-empirical model for shallow water acoustics model by Rogers (1981) using a multidimensional curve fitting tool to model the difference between Rogers' predictions and field data as a function of site-specific environment variables. The results produced a slightly improved model for transmission loss prediction but still faced the problem of an overabundance of parameters required for the input field to give reliable results. In an effort to address these issues, a new empirical model was developed to explain transmission loss by leveraging a large sound dataset collected in different sites in Florida and using linear regression to establish a relationship between the transmission loss coefficient and a source level dependent parameter (Ainslie, 2014). Results indicated the tool was able to compute more reliable transmission loss coefficients compared to the one currently in use by the NMFS calculator resulting in more accurate results for ranges with sound pressure levels below the thresholds. However, the new model showed an apparent dependency between sound attenuation and amplitude, and the physics associated with this apparent dependency require further investigation.

CHAPTER 1
INTRODUCTION AND BACKGROUND INFORMATION

1.1 Introduction

Marine pile driving produces very high levels of sound which could be harmful to marine wildlife. Most underwater pile driving in Florida takes place during bridge construction over creeks and rivers which are generally considered very shallow water when compared to typical sound wavelengths. It is therefore necessary to understand sound propagation in very shallow water and be able to reliably predict sound pressure levels (SPL) at various ranges from a pile driving location to ensure they are within the regulatory limits at specified ranges.

1.2 Background

The Florida Department of Transportation (FDOT) was assigned with all responsibilities of the National Environmental Policy Act (NEPA) in December 2016 by the Federal Highway Administration (FHWA). This required FDOT's environmental office to complete the NEPA process on all federal roadway projects in the state which includes deliberation of the projects' impacts on species. In the process, the National Marine Fisheries Services (NMFS) and the United States Fish and Wildlife Service (USFWS) presented concerns about potential effects marine pile driving might have on Florida's protected species. These concerns are expected to increase due to aging infrastructure and sea level rise.

1.3 Regulatory Criteria and Scientific Guidelines

The USFWS and NMFS reviewed the available scientific information and developed regulatory criteria for assessing the potential impacts of pile driving activities (FHWG, 2008) which were concluded in a meeting with key staff from the FHWA, NOAA, NMFS, USFWS, Departments of Transportation from California, Oregon and Washington and national experts on

sound propagation activities that affect fish and wildlife species of concern. These are guideline criteria also followed by FDOT. The criteria are summerized in Table 1-1 below.

Table 1-1. Interim Fisheries Current Noise Guidelines Criteria adapted from

Effect	**Metric**	**Fish Mass (g)**	**Threshold (dB relative to 1µPa)**
Onset of physical injury	Peak Pressure	N/A	206
	Accumulated SEL	>2g	187
		≤2g	183
Adverse behavior effects	RMS Pressure	N/A	150

The criteria proposed considered the fact that different fish species are affected differently and have different sensitivity to sound pressures for instance, fish with a reduced or no swim bladder generally are less sensitive to sound than those with a fully developed swim bladder. In this table, the peak SPL refers to the highest SPL recorded in a given interval of time. The sound-exposure level (SEL) and the root-mean-squared sound pressure (RMS) are defined as follows:

$$\mathrm{RMS} = \sqrt{\frac{1}{t_2 - t_1}\int_{t_1}^{t_2}\left(\frac{p}{p_0}\right)^2 dt} \tag{1-1}$$

$$\mathrm{SEL} = \int_{t_1}^{t_2}\left(\frac{p}{p_0}\right)^2 dt \tag{1-2}$$

where p is the SPL from a time series in Pa; p_0 is the reference SPL which was defined as 1 µPa; and t_1 and t_2 are start and stop times of a given time-series.

1.4 Transmission Loss Modelling

It is important to understand both if and over what distance from a pile the thresholds in Table 1-1 are exceeded. To understand the "where," one must understand how pile driving noise is attenuated as the sound waves propagate through the water. The concept of sound attenuation over some distance is known as transmission loss (TL). Many underwater sound propagation

models have been developed since the 1940s to estimate TL. These acoustic models are generally grouped based on their approaches as shown in Figure 1 below (Dawoud et al., 2016). The two major categories are numerical models and empirical models.

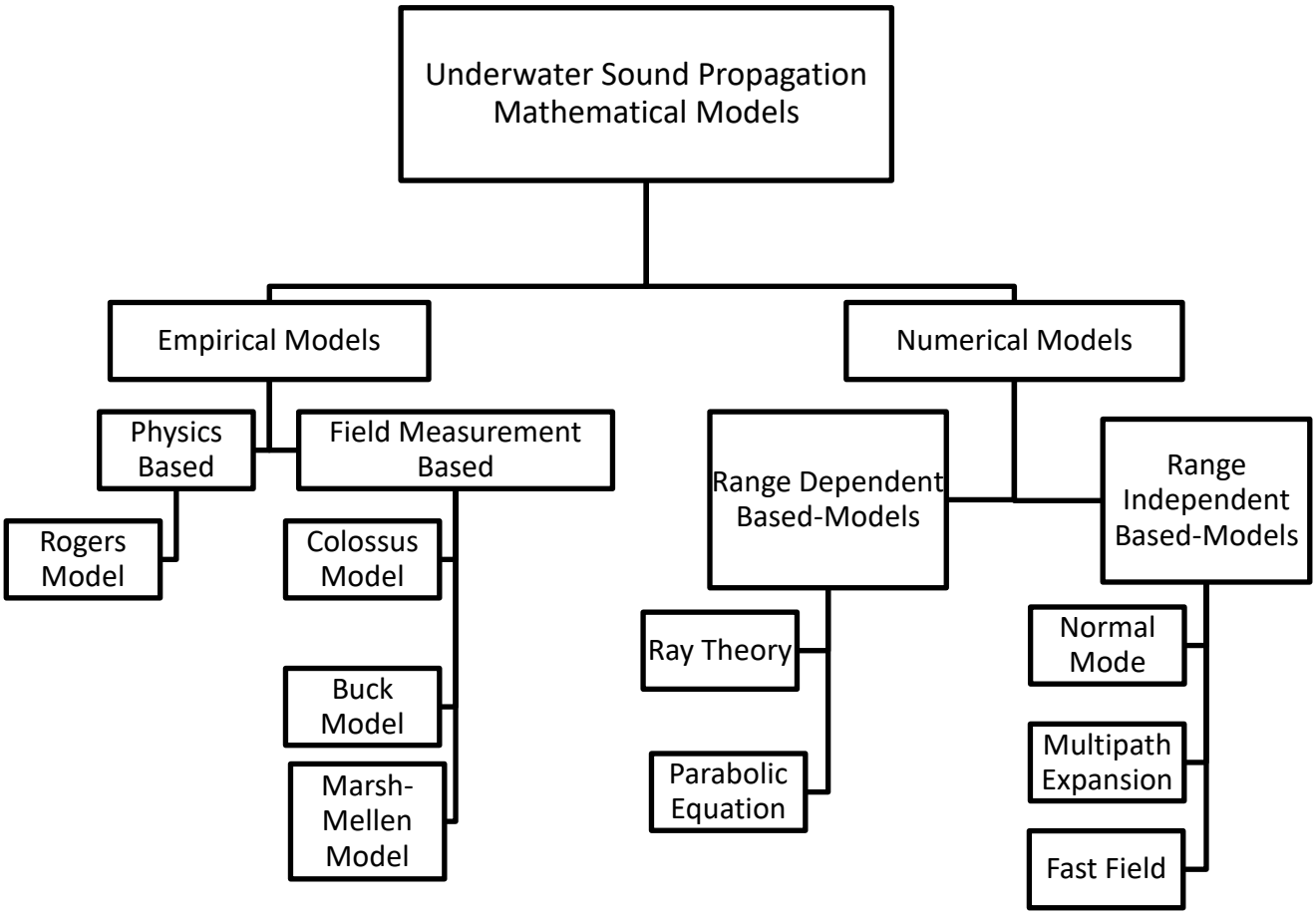

Figure 1-1. Underwater sound propagation mathematical models (adapted from Dawoud et al., 2016)

1.4.1 Numerical models

Numerical models attempt to solve the wave equation or Helmholtz equation, which governs of underwater sound propagation (Jensen et al., 2011) with associated boundary and radiation conditions. The main difference between different numerical models is their mathematical treatment of the wave equation before implementation of the solution. Solving the wave equation is usually done for a single frequency but sometimes a solution can be calculated

for each frequency or band of frequencies across a required range. The hydroacoustic numerical propagation models are usually classified based on their source frequency characteristics (either low or high frequency), the dependence of the propagation region on the local environment (either range dependent or range independent) and the water depth of the propagation domain (either deep or shallow water). Therefore, different models are suitable for application in some situations and limited or inapplicable in others. Based on the underlying method of solving the acoustic wave equation, the numerical propagation models are generally grouped into Ray Methods, Wavenumber Integration techniques, Normal Modes and Parabolic Equations.

These numerical models are however very sophisticated, not easy to implement, and some of their key assumptions are questionable for very shallow water that would be encountered during most pile driving sites in Florida. Furthermore, limited knowledge of subsurface conditions makes the application of these models for underwater pile noise modelling unreliable. Empirical models could therefore provide a better estimate of transmission losses than numerical models in pile noise modelling.

1.4.2 Empirical models

Empirical models are developed based upon field measurements or physics-based approaches coupled with field measurements or inferences from more sophisticated models. Many previous studies (Ainslie et al., 2014; Hastrup & Akal, 1980; Rogers, 1981; Marsh & Schulkin, 1962) indicate that an empirical shallow water TL model is generally given by:

$$TL = B + A \log_{10} R \tag{1-3}$$

where A and B depend on the propagation conditions and R is the range (i.e., distance) from the sound source (which, in this case is the pile drive). Ainslie et al. (2014) shows that A and B are not arbitrary values and are not independent of one another. The term $A \log_{10} R$ is associated with geometrical spreading loss and B is likely TL due to a combination of multiple variables including

depth, range, frequency and bottom geoacoustic properties. Rogers (1981) summarized this and explained that shallow water acoustics is plagued by an overabundance of input parameters. A fully comprehensive, accurate model would have to accommodate approximately 24 separate inputs, and most of these are difficult to measure using traditional geotechnical and hydrological testing. For multilayered bottoms, up to 35 similarly difficult to measure inputs would be required. Most models therefore just consider different subsets of the complete input field. This has led to the studies proposing different forms and values for A and B.

Ainslie et al. (2014) pointed out that pile driving is a special case of underwater sound propagation in the sense that unlike most shallow water propgation situations, pile driving cannot be thought of as point source. This was also shown by Reinhall and Dahl (2011) who proposed a complex-phased array of point sources of fixed strength and linearly varying depth dependent phases to model sound radiation as a function of range from the pile. This method produced and important range parameter R^* given by $R^* = \frac{H}{tan\theta}$ where H is the water depth and θ is the angle related to the ensuing mach wave due to the supersonic compressional wave travelling through the pile from impact pile driving. For ranges less than R^*, SPL are highly depth dependent but less so for ranges greater than R^*. Ultimately, Ainslie et al. (2014) proposed a model of the form $TL = 10\log_{10} R + \alpha R$ for pile driving TL where α is some attenuation coefficient based upon water and/or soil conditions.

The current design guidelines for underwater noise mitigation use a simple Practical Spreading Loss Model (NOAA, 2021; also known as the NMFS calculator) generally given by:

$$TL = F\log_{10} R \tag{1-4}$$

where R is the range and F is the TL coefficient. The NMFS calculator uses F = 15. Thus specifically, the PSLM currently used by the NMFS calculator is given by:

$$TL = 15 \log_{10} R \quad (1\text{-}5)$$

The TL coefficient value of 15 is the result of assuming that most TL is due to mode stripping. The advantage to Eq. 1-5 is that using it to predict TL is very easy to implement. But, its disadvantage is that data show that it often tends to underestimate TL (hence overestimate SPL) at respective ranges because it does not take into account many important variables such as bottom loss, water depth and the fact that different sound frequencies are attenuated differently. This tendency toward over-conservatism may lead to unnecessary increases in construction costs. But, as of yet, a similarly easy to use model is not yet available for use during construction.

1.5 Goals and Objectives

The goals of this study were to use computer modelling and sound data collected from various bridge construction sites in Florida to garner a better understanding of underwater TL during pile driving. Overall, the goal was to leverage this improved understanding of TL to develop a new empirical model for TL that was easy to use, that required no onsite calibration, and that would be at least as accurate or more accurate than Eq. 1-5.

1.6 Thesis Organization

This thesis is comprised of five chapters. Chapter 1 provides a brief introduction and background information on the problem. Chapter 2 is a description of the data collection methods and procedures used in the study. Chapter 3 is comprised of the analysis of marine pile driving noise using a computational fluid dynamics acoustic modelling package. Chapter 4 details the analysis of marine pile driving noise using empirical data fitting. Chapter 5 presents an overall summary, conclusions and recommendations.

CHAPTER 2
DATA COLLECTION METHODOLOGY

A significant amount of data has already been collected during underwater pile driving operations; Buehler et al. (2015) summarize these data well. However, most of these data came from California and Washington State and it was unclear how these data would translate to geotechnical or hydrological conditions typical in Florida. As such, data were collected at several sites around Florida and these data were used for analysis throughout this study.

2.1 Site Information

A total of 9 bridge construction sites around Florida were visited for data collection. Data from the first five sites were partially reported by Berube (2019) and Crowley et al. (2020) while data from the other four sites are new and presented for the first time in this study. Fig. 2-1 shows the approximate location of the sites in Florida.

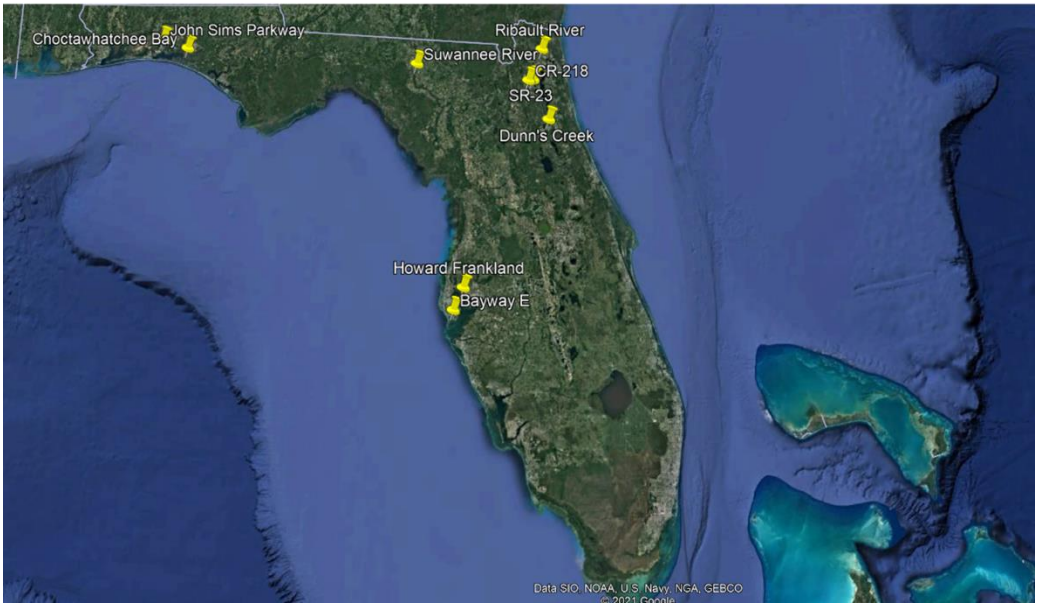

Figure 2-1. Sites Locations in Florida

Environmental conditions varied across the sites. Soil profiles for each site were obtained from contractor boring logs and were later used for geotechnical data analysis. Bathymetry data to

be used for computational fluid dynamics modelling for some of the sites was provided by FDOT and was supplemented by data from NOAA.

2.2 Data Collection System

Sound data was collected using a system of buoy-mounted hydrophones developed by Berubue (2019). The hydrophones were suspended from floating platform system that consisted of two small pontoons attached to aluminum frames. Each frame held a PelicanTM 1450 watertight box that housed the electronics of the system. Scanstrut cable clam/deck seals were used to pass a hydrophone cable and a thermocouple cable from the exterior into the box while a MENCOM MDE45-8FR-RJ45-BM waterproof Ethernet connection was used to route an Ethernet cable into the case. The electronics contained in the cases were Bruel and Kjaer 2250 handheld analyzers; Bruel and Kjaer 2647 charge converters; L-Com BT-CAT5-P1 power-over-Ethernet converters; 24-volt motorcycle batteries connected in series. Outside of the case was a Bruel and Kjaer 8103 hydrophone; a Ubiquiti Bullet M2 wireless access point; and an L-COM HG2409UP antenna. The batteries, power converter, Bullet, and antenna connect to the handheld analyzer via Ethernet cable and broadcast the measured sound data to a computer in real-time. In addition, Garmin GPSMAP global position system (GPS) units were added to each box to track the location of the buoys in the field. Hydrophone and thermocouple cables were attached to a fish weight to ensure they remain vertical in the water column and a wire strain relief system was attached to them to protect them from excessive tensioning.

In total, five of these floating data collection systems were built so that data from five ranges from the piles could be captured simultaneously. Photographs of these data collection platforms are shown below in Fig. 2-3 and Fig. 2-4. Prior to each buoy deployment, buoys hydrophones were calibrated using a Bruel and Kjaer 4229 calibrator.

Figure 2-2. Electronics inside data collection case

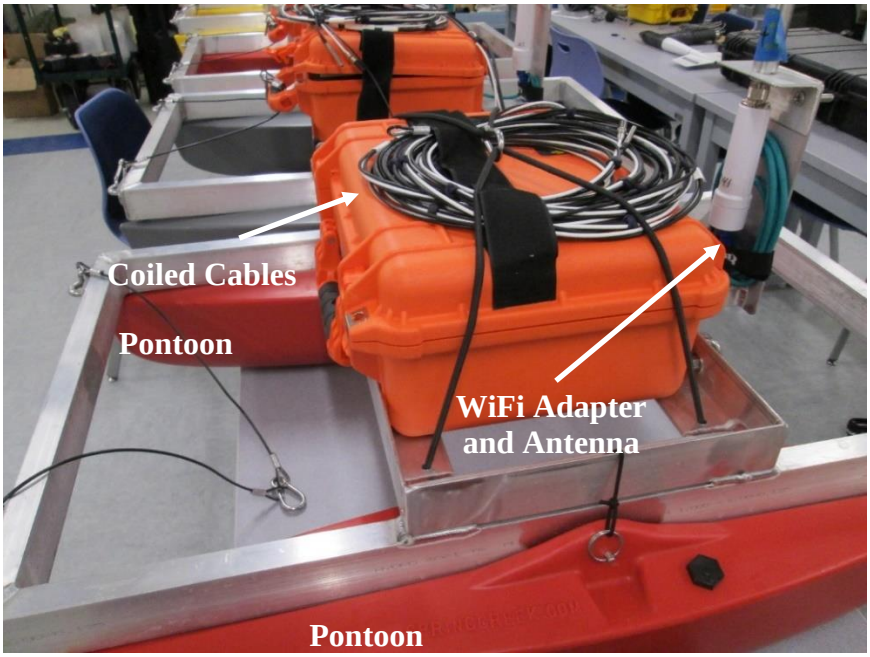

Figure 2-3. Data collection buoy ready to deploy

2.3 Data Collection Procedure

These buoys were deployed at varying distances from the piles being driven. Generally, the first buoy was deployed as close as possible to the pile or pile bent being driven without compromising safety. After deployment of the first buoy, each of the other buoys were deployed

at distances twice as far as the distance of the buoy preceding it. For instance, if the first buoy was deployed at 25 m from the piles, the second would be deployed at 50 m, the third at 100 m, the fourth at 200 m and the fifth at 400 m. Approximate deployment distances were achieved using a LaserWorks Long Distance 1,200-Yard Hunting Range finder and were later verified using GPS data collected by the on-board Garmin GPS units. Once the buoys were positioned, the hydrophones were hung from the buoys to approximately half the water column depth. Verticality of the hydrophones in the water column was ensured by the 240 g (12 oz) fish weight attached at the end of the cable. Depth data was obtained by a depth meter attached to the vessel. Sound data were collected in two forms. First, a signal recording was sampled at 48 kHz. Secondly a maximum Z-weighted (no frequency weighting) value was captured every second and was recorded in a separate file (LZ_{peak} in Bruel and Kjaer software). In all, sound data was collected from 64 separate drive events. These collected data are summarized in the Table 2-1 below and were used throughout this thesis during both computational and empirical analyses.

Table 2-1. Site Data Summary

Site Name	Northing	Easting	Pile Type	Hammer Type	Number of Drives
Bayway E Bridge	30°04'19"	81°49'08"	36-inch open-ended steel	200T vibratory hammer	1
Bayway E Bridge	30°04'19"	81°49'08"	30-inch by 30-inch by 123-ft long square PCP	APE Model D80-52	2
Dunn's Creek Bridge	29°34'38"	81°37'35"	PZ-27 sheet pile	200T vibratory hammer	2
Ribault River Bridge	30°23'37.38"	81°42'48.17"	24-inch by 24-inch by 110-ft long square PCP	APE Model D36-42	4
County Road (CR) 218 Bridge	30°03'37.96"	81°52'17.42"	24-inch by 24-inch by 110-ft long square PCP	APE Model D62-22	5
Suwannee River Bridge	30°14'48.86"	83°15'0.34"	24-inch diameter open-ended steel	Del-Mag D-46	3
John Sims Parkway Bridge	30°30'10.43"	86°29'38.66"	18-inch by 18-inch by 81-ft square PCP	BSP C585-u	1
State Road (SR) 23 Bridge	30°04'19"	81°49'08"	24-inch by 24-inch by 110-ft long square PCP	APE D62-70	13
Choctawatchee Bay Bridge Fenders	30°24'16.26"	86°10'0.03"	PZ-27 sheet pile	200T vibratory hammer	2
Howard Frankland Bridge	27°55'17.49"	82°36'25.50"	30-inch by 30-inch by 73-ft long square PCP	APE D80-44	18
Howard Frankland	27°55'17.49"	82°36'25.50"	Steel King piles	APE D80-44	13

CHAPTER 3
ANALYSIS USING COMPUTATIONAL FLUID DYNAMICS

3.1 Introduction

As discussed in Ville et al. (2017), computational fluid dynamics (CFD) can be used to model underwater sound propagation. The advantage to using CFD to analyze underwater noise due to pile driving is that CFD allows one to isolate TL variables from one another so that they may be analyzed independently. In the context of underwater pile driving noise, TL should be mostly governed by six major factors: localized site geometry, bed (i.e., geotechnical) reflectivity, water surface reflectivity (likely a function of free-surface wave action), localized currents, water temperature, and water salinity. A CFD package allows one to calibrate bed and water surface reflectivity to match data while isolating/controlling the other variables. If the effect of bed reflectivity is well-understood, it should be possible to correlate it to geotechnical properties and thus establish their contribution to overall TL.

3.2 Objective

As noted in Chapter 1, field measurements often imply that *F*-values in Eq. 1-4 are much greater that $F = 15$. The goal of the work presented in this chapter was to use a CFD package to determine if the discrepancies between observed *F*-values and $F = 15$ could be partially explained by variability of geotechnical conditions, particularly geotechnical absorption, at various sites.

3.3 Methodology

To accomplish this goal, several models were prepared using Siemens' Star-CCM+ (Siemens 2021) commercially available computational fluid dynamics (CFD) model.

3.3.1 Acoustic Wave Model Formulation

The complete set of acoustic perturbation equations used by Star-CCM+ are as follows:

$$\frac{\partial p'}{\partial t} + c^2 \nabla \cdot \left(\overline{\rho} u^a + \overline{v} \frac{p'}{c^2} \right) \approx 0 \tag{3-1}$$

$$\frac{\partial u^a}{\partial t} + \nabla(\overline{v} \cdot u^a) + \nabla\left(\frac{p'}{\overline{\rho}}\right) \approx \nabla\Phi_p \tag{3-2}$$

Where:

- p' = perturbation pressure;
- u^a = irrotational perturbation velocity;
- $\overline{\rho}$ = time-averaged density;
- $\overline{v}$ = time-averaged (i.e., mean) velocity;
- c = speed of sound;
- Φ_p = the noise source function.

Ewert and Schroder developed a relationship between perturbation pressure, the noise source function, and the acoustic pressure, p^a:

$$p' = \overline{\rho}\Phi_p + p^a \tag{3-3}$$

Eqn. 3-3 is applied to Eqn. 3-1 by taking the substantial derivative, i.e.:

$$\frac{\partial}{\partial t} + \overline{v} \cdot \nabla \tag{3-4}$$

Likewise, Eqn. 3-3 is applied to Eqn. 3-2 using the divergence. This leads to two equations where of p^a and u^a are dependent variables. Then, assuming incompressible flow (i.e., $\nabla \cdot \overline{v} = 0$) and combining these equations, a single equation is obtained that describes acoustic pressure and noise sources in an incompressible flow domain:

$$\frac{1}{c^2}\frac{\partial^2 p^a}{\partial t^2} + \frac{2\overline{v}}{c^2} \cdot \frac{\nabla \partial p^a}{\partial t} + \frac{\overline{v}\cdot\nabla}{c^2}(\nabla \cdot \overline{v} p^a) - \nabla^2 p^a = -\left[\frac{\overline{\rho}}{c^2}\frac{\partial^2 \Phi_p}{\partial t^2} + \frac{2\overline{v}\cdot\nabla}{c^2}\overline{\rho}\frac{\partial \Phi_p}{\partial t} + \frac{\overline{v}\cdot\nabla}{c^2}\left(\nabla \cdot \overline{v}\Phi_p\right)\right] \tag{3-5}$$

Then, due to the incompressible flow condition:

$$\overline{\rho}\frac{\partial \Phi_p}{\partial t} \approx \frac{\partial P'}{\partial t} \tag{3-6}$$

And:

$$\nabla\Phi_p \approx \frac{1}{\overline{\rho}}\nabla P' \tag{3-7}$$

In addition, a physical damping mechanism is added to Eq. 3-6, which is necessary to eliminate false waves that originate due to mesh-coarsening. From this, the final wave equation is:

$$\frac{1}{c^2}\frac{\partial^2 p^a}{\partial t^2}+\frac{2\overline{v}}{c^2}\cdot\frac{\nabla\partial p^a}{\partial t}+\frac{\overline{v}\cdot\nabla}{c^2}(\nabla\cdot\overline{v}p^a)-\nabla^2\left(p^a+\tau\frac{\partial p^a}{\partial t}\right)=-\left[\frac{1}{c^2}\frac{\partial^2\Phi_p}{\partial t^2}+\frac{2\overline{v}\cdot\nabla}{c^2}\frac{\partial P'}{\partial t}+\frac{\overline{v}\cdot\nabla}{c^2}(\nabla\cdot\overline{v}P')\right] \quad (3\text{-}8)$$

where τ is the physical damping term defined as:

$$\tau=\chi\frac{\Delta t}{\pi\lambda} \quad (3\text{-}9)$$

in which:

- χ = the damping coefficient (0 for no damping; 1 for maximum damping);
- Δt = the time-step;
- $\lambda=c\frac{\Delta t}{\Delta x}$; i.e., the local Courant Number (i.e., the Courant-Friedrichs-Lewy or CFL condition).

3.3.2 Energy Conservation

For this preliminary set of computational runs, investigators utilized the simplest set of built-in models in Star-CCM+. Specifically, the acoustic wave model was coupled with an inviscid flow model where conservative of energy was enforced via the built-in segregated fluid enthalpy equation:

$$\frac{\partial(\rho E)}{\partial t}+\nabla\cdot(\rho E v)=f_b\cdot v+\nabla\cdot(v\cdot\sigma)-\nabla\cdot q+S_E \quad (3\text{-}10)$$

where:

- E = total energy per unit mass;
- q = heat flux;
- S_E = energy source per unit volume;
- f_b = the resultant of the buoyant forces such as gravity, centrifugal force, etc. per unit volume acting on the continuum;
- ρ = the density of the fluid medium;

σ, the stress tensor, is computed as the sum of normal stresses, $-pI$ and viscous (i.e., shear) stresses, T:

$$\sigma=-pI+T \quad (3\text{-}11)$$

3.3.3 Model Phases

In its truest sense, the Star-CCM+ acoustic wave model is simply a repurposing of its aeroacoustics model in the sense that the equations above are applied to water instead of air. Star-CCM+'s built-in International Association for the Properties of Water and Steam, Industrial Formulation, 1997 (IAPWS-IF97) model was used throughout all models' flow domains. As such, water was assumed to be incompressible with a molecular weight of 39 $lb/kmol$ (18 $kg/kmol$). The speed of sound was assumed to be 3,243 mph (1,450 m/s).

3.3.4 Boundary Conditions

All model boundaries were assumed to be "walls" since models were run under stagnant flow conditions because observed currents were generally very small when compared to the speed of sound. The acoustic wave equations above are valid both within the flow domain and at reflective or partially absorbing boundaries. Sometimes, it is necessary to focus a CFD model on an area of interest by "cutting" computational mesh where a wall would not physically exist in nature. Under these conditions, it is necessary to specify a non-reflective boundary condition that allows acoustic waves to leave the computational domain without any spurious reflections. By applying the $\nabla \cdot$ operator to Eqn. 3-1, one can show that:

$$\nabla \cdot u^a = -\frac{1}{\overline{\rho} c^2}\left(\frac{\partial p^a}{\partial t} + \overline{v} \cdot p^a\right) \tag{3-12}$$

Also, acoustic pressure must be related to the normal component of acoustic velocity:

$$p^a = \overline{\rho} c u^a \cdot n \tag{3-13}$$

where *n* is a normal unit vector. Taking the derivative of Eqn. 3-10 and applying Eqn. 3-11 leads to:

$$\nabla p^a \cdot s = -\frac{(1-\overline{v}\cdot n/c)}{\left(1-|\overline{v}^2|/c^2\right)c}\left(\frac{\partial p^a}{\partial t}\right)|s| \tag{3-14}$$

in which *s* is the face normal area vector and |s| is its magnitude.

3.3.5 Field Data

The above models were applied at three bridge sites where underwater noise data had been collected. These sites were the Bayway E, Ribault River, and John Sims Parkways locations from Table 2-1. Note that in Table 2-1, Bayway E is listed twice because two pile drive types were observed at this site. The analysis presented here only examined the first set of drives where the vibratory hammer was used.

Sound data were analyzed to compute F-values associated with Equation 1-4 by fitting a best-fit regression line to the data of the form $y = F \log_{10} R + G$ to the data. It was assumed then that G corresponded to the sound directly at the pile while y corresponded to the sound-level at R. As will be discussed in Chapter 4, this assumption may not be entirely accurate, but for the purposes of the discussion in this chapter, this distinction is mostly irrelevant.

3.3.6 Local Bathymetry Data

With assistance from FDOT, local bathymetry data were collected for the three site locations. While these data were useful, generally, available bathymetry data from these sites were only in the direct vicinity of the bridges, and usually parallel with the bridges (see Fig. 3-1 for an example). In the context of determining sound propagation downstream and perpendicular from the bridges, these data were insufficient. As such, these data were supplemented with data from the NOAA. The NOAA data tended to be lower resolution than data provided from FDOT in the sense that fewer soundings were available per unit area. In the context of channels, where bridges are located, this meant assuming trapezoidal bathymetries beyond the extents of NOAA's soundings.

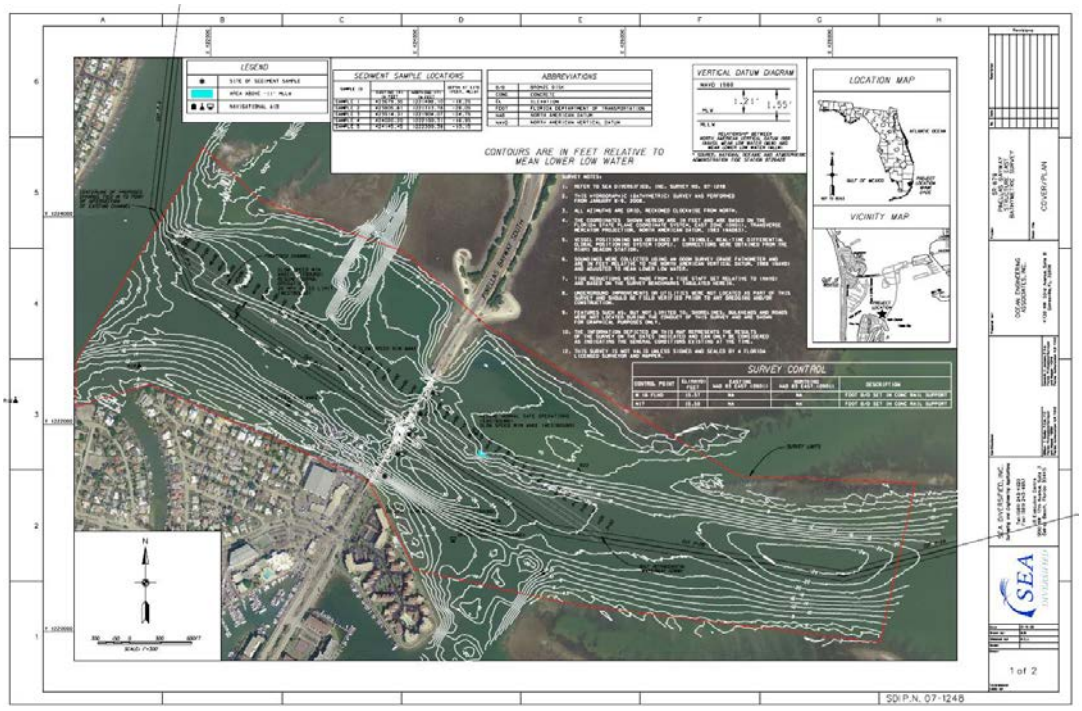

Figure 3-1. Example of available local bathymetry data from FDOT from the Bayway E location

The combined FDOT/NOAA data were used to draw geometrical meshes that captured local bathymetry. Water surfaces were assumed to be flat while upstream/downstream mesh extents were assumed to be vertical planes. Field buoys were geolocated on these meshes so they could be later used as comparison points for downstream noise data. This means that comparison points in the model corresponded to locations where buoys were located in the field. In addition, a pile extrusion was “cut” though each mesh. An example of a geometrical mesh is presented in Fig. 3-2:

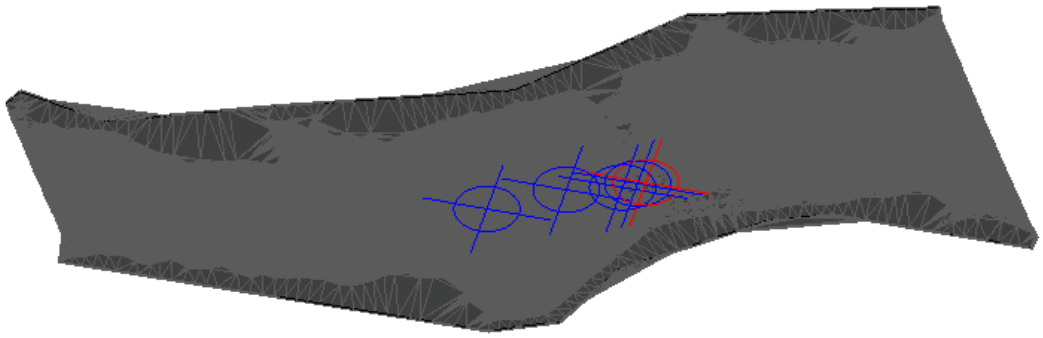

Figure 3-2. Example of geometrical mesh from the Bayway E location showing the buoy locations (in blue crosshairs); and the pile location (in red crosshairs)

3.3.7 Meshing

Once the geometrical model had been developed for each location, it was imported in Star-CCM+. Where necessary, the meshes were trimmed to focus on the bridge/buoy locations and narrow the computational channels. This ensured that the resultant mesh would contain a reasonable number of cells relative to available computational resources. Once computational geometry had been finalized, the built-in Star-CCM+ surface wrapper was used to ensure that the meshes were water-tight. Then, each geometry surface was remeshed using Star-CCM+'s surface mesher (Fig. 3-3). The remeshed surfaces were used to create volume meshes using Star-CCM+'s built-in polyhedral meshing scheme (Fig. 3-4).

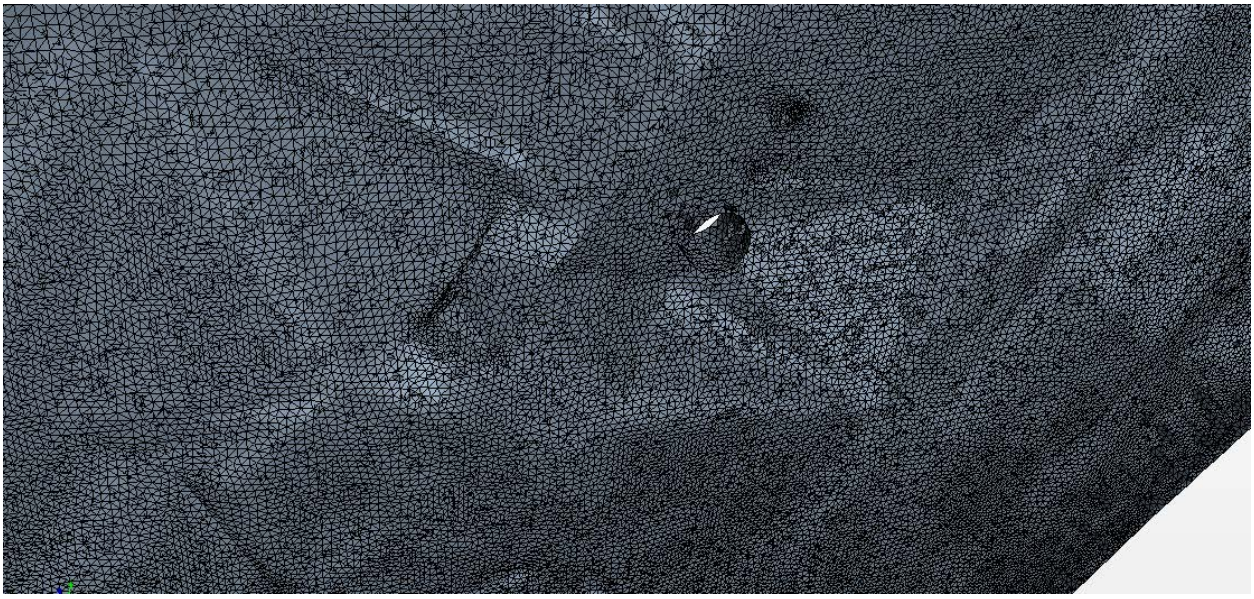

Figure 3-3. Example of remeshed surface showing the Bayway E location; mesh shown from the bottom-up so bathymetry can be visualized

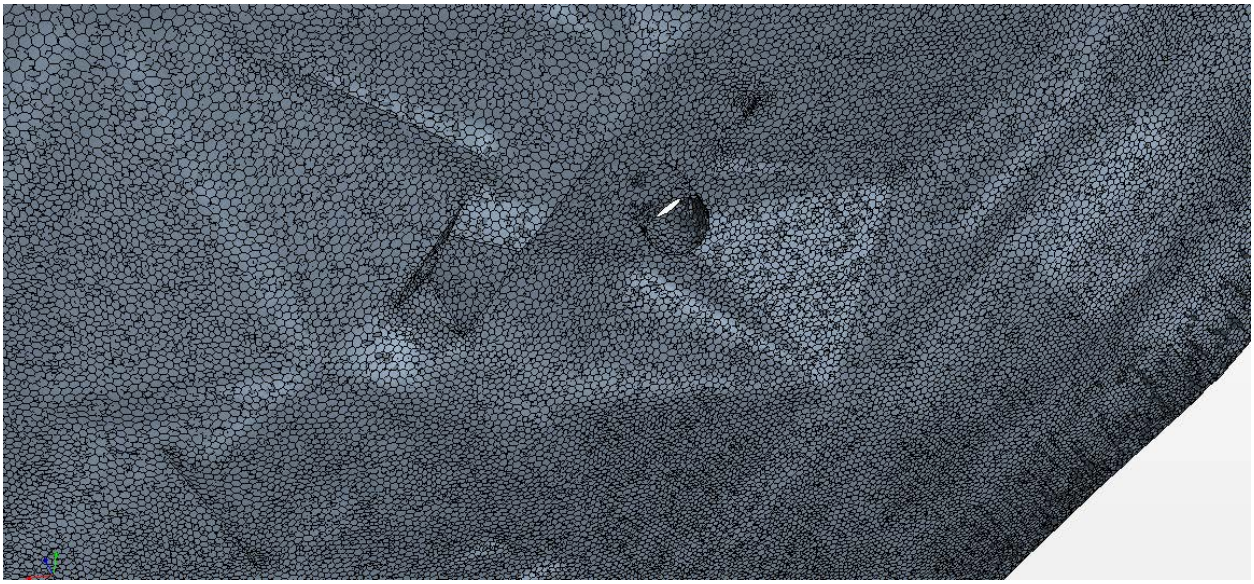

Figure 3-4. Example of polyhedral mesh showing the Bayway E location; as in Fig. 3-3, mesh shown from bottom-up to visualize bathymetry

Mesh resolutions were chosen so that even with trimmed geometries, there were less than 10 million cells per model. In addition, for shallower sites such as the Ribault River, resolutions needed to be sufficiently small to capture localized bathymetry data. For context, the Ribault River's maximum water depth was only approximately 3.78 m. With such a shallow depth, a resolution of 1 m would not capture shallower portions of the river correctly. Table 3-2 provides a

summary of cell resolution and cell number. After the meshes had been generated, the locations where data were collected were geolocated using Star-CCM+'s derived part tool. Each data collection point was assumed to be a point at the mid depth.

Table 3-2. Mesh Resolutions

Site	Baseline Resolution (m)	Number of Cells
Bayway E Bridge	0.75	1,735,324
Ribault River Bridge	0.30	2,462,211
John Sims Parkway	0.50	6,677,729

3.3.8 Imposing a Pile Drive Function

Initial conditions of each model were such where it was assumed that no flow was present in each computational domain. At the pile, a pile drive function was assumed based upon collected field data. Each pile drive hammer strike resembled a sinusoidal exponential decay function as shown below in Fig. 3-5:

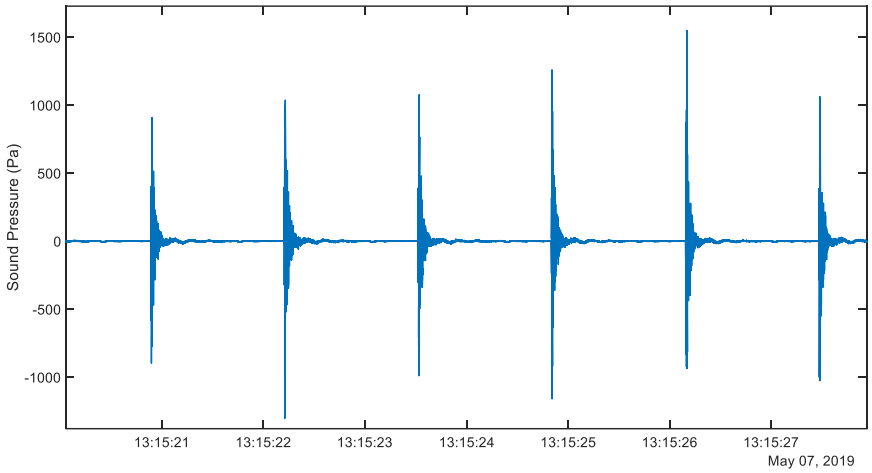

Figure 3-5. Pile drive hammer strike sound data from Ribault River

Fig. 3-5 shows maximum sound amplitudes between 1,000 Pa and 1,500 Pa, which corresponds to to between 180 and 185 dB relative to 1 μPa. It is important to note that these sound-levels are from collected data – in the case of Fig. 3-5, the buoy closest to the pile. Extrapolating these sound levels back to the sound source using a logarithmic TL curve, one finds that source pressure was

on the order of 250 dB relative to 1 μPa, which corresponds to pressure levels of 3×10^6 Pa. In addition, Fig. 3-5 shows that sound oscillated with a very high frequency and that sound associated with each hammer strike appears to dampen in approximately half a second. Using this information, a pile drive source term, *S*, was inferred for each pile of the form:

$$S = 3 \times 10^6 \, e^{-10t} \cos(100t) \tag{3-15}$$

This source term was applied to each simulation's extruded pile at $t = 0$. The models then tracked the subsequent SPL as it traversed through each flow domain.

3.3.9 Imposing Boundary Absorption

Each model was run with a series of absorption coefficients at both the water surface and along each bed. Acoustic absorption was applied at each appropriate wall by marking the walls as partially absorbent and specifying the percentage of sound pressure absorbed. Then, several water surface/bed coefficients were used. Bottom absorption coefficients, α_b, were varied in 20% increments from 0% to 100% (i.e., α_b was equal to 0, 0.2, 0.4, 0.6, 0.8, 1.0). Water surface coefficients, α_s, focused more on the low-end of the spectrum; tested α_s values were 0, 0.02, 0.04, 0.06, 0.08, 0.10, 0.15, 0.20, 0.40, 0.60 because Asgedom et al. (2017) indicated that relatively quiescent water surfaces similar to those in this study sites are almost perfect reflectors tending to only absorb/transmit a maximum of 10% of low frequency incoming sound waves.

Taken together, this represented 60 surface/bottom coefficient combinations. Each of these were tested at the Bayway E and Ribault River locations. At that point, it became relatively obvious that bottom absorption played a significant role in determining TL. As such, only 35 combinations were tested at the John Sims Parkway location.

3.3.10 Solving Each Model

Each model was solved using Star-CCM+'s built-in implicit unsteady flow solver with a first-order implicit time step of 0.005 seconds. At each time step, 5 iterations were used; these showed good convergence when examining each model's residuals.

3.3.11 Mesh Resolution and Time Step Sensitivity

Because Star-CCM+ is a finite volume model, results from any simulation using it are mesh dependent. In other words, given a certain mesh, the simulation may run and produce data. If a different mesh is used, the model will also run and produce different data. The difference between the first model and the second model is due to computational errors associated with discretization. A "perfect" simulation is one where the discretized steps in space (i.e., x, y, and z) and time (t) approach zero. Or, put another way, the "perfect" simulation is one with infinite cells. But, of course, due to computational constraints, this is impossible. Therefore, the goal of most CFD studies like this is to produce data that is within 5% of the "perfect" solution.

While it is impossible to compute the "perfect" solution, it is possible to infer what this solution should be by using a Richardson extrapolation. A Richardson extrapolation is a common methodology in CFD whereby a certain geometry is run using three or more meshes (or time steps), and all other model input are held constant. Then, some value of interest from each simulation is examined from each computational run. The value of interest is plotted as a function of resolution, and a best-fit regression line is fit to the data. The line's intercept is the "correct" answer. Generally, if production runs are within 5% of the Richardson extrapolated value, simulations are usually deemed to be converged and close enough relative to reality. This sort of study was conducted using a subset of the models at each location by coarsening the meshes and timesteps several times.

3.3.12 Data Analysis

Each absorption coefficient combination's modeled TL coefficient was estimated by fitting best-fit regression curves of the same form that were used to field data to the modeled data (i.e., curves of the form $y = F \log_{10} R + G$) at each modeled buoy location. Thus, F from the data fit corresponded to modeled TL. These modeled *TL* coefficients were contoured as functions of both α_s and α_b. During the mesh and timestep sensitivity studies, the "value of interest" was F-value deviation from these parametric data-fits using a subset of the modeled data.

3.4 Results

3.4.1 Sample Simulation Results

Sample plots of sound-pressure level from the simulations and associated sound decay curves from the model runs are presented below while additional plots are presented in Appendix A and Appendix B:

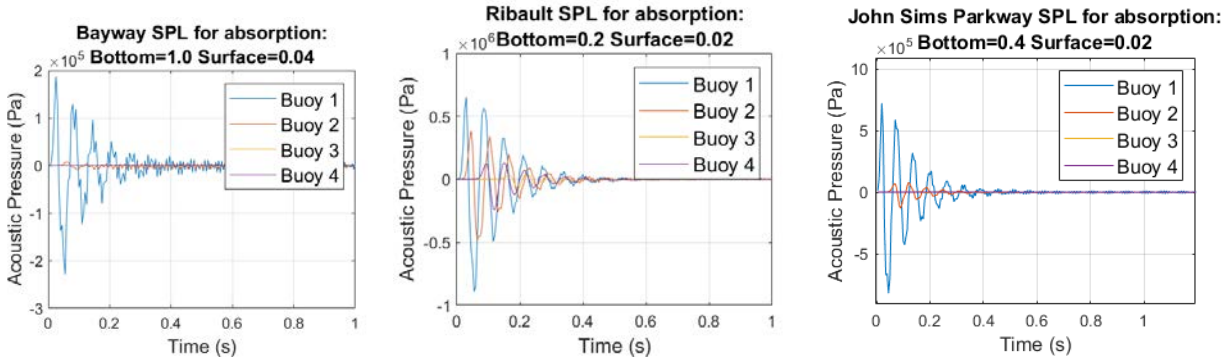

Figure 3-6. Sample results of sound-level at each buoy as a function of time showing 1.0 Bottom-0.04 Surface Absorption at Bayway E (left); 0.2 Bottom-0.02 Surface Absorption at the Ribault River (middle); and 0.4 Bottom-0.02 Surface Absorption at the John Sims Parkway (right)

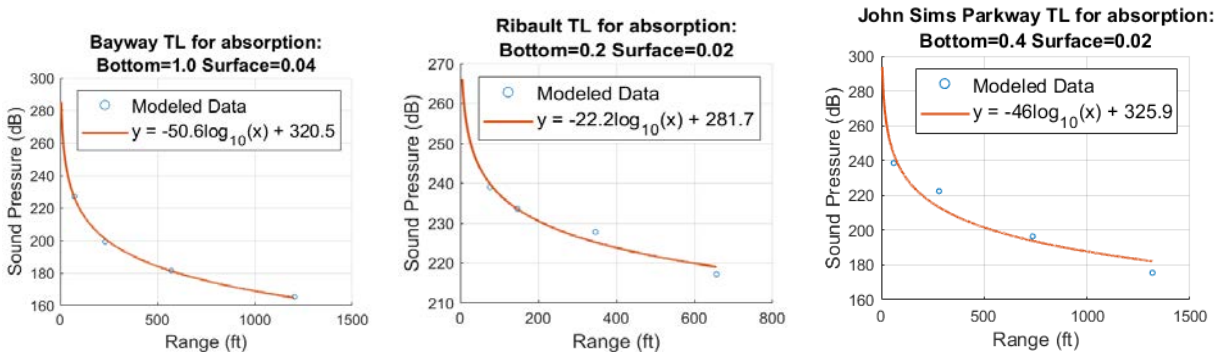

Figure 3-7. Sample TL curve results from 1.0 Bottom-0.04 Surface Absorption at Bayway E (left); 0.2 Bottom-0.02 Surface Absorption at the Ribault River (middle); and 0.4 Bottom-0.02 Surface Absorption at the John Sims Parkway (right)

3.4.2 Mesh Sensitivity Study Results

The results from the mesh sensitivity study for all three sites are as shown below in Fig. 3-8.

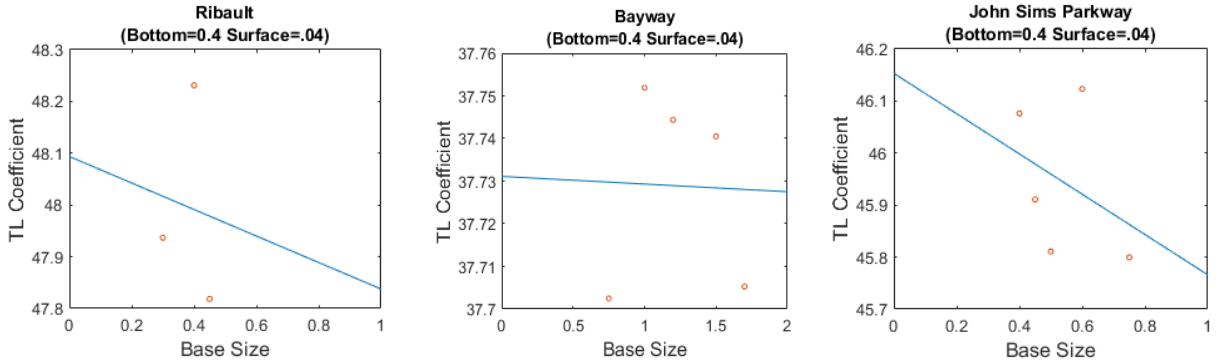

Figure 3-8. TL coefficient versus Mesh Resolution for Bayway E (left); Ribault River (middle); and John Sims Parkway (right)

For all three sites the results generally indicated computaitonal convergence.

3.4.3 Contour Plots

Results from the TL contours as functions of α_b and α_s are presented below in Fig. 3-9 thorugh Fig. 3-11:

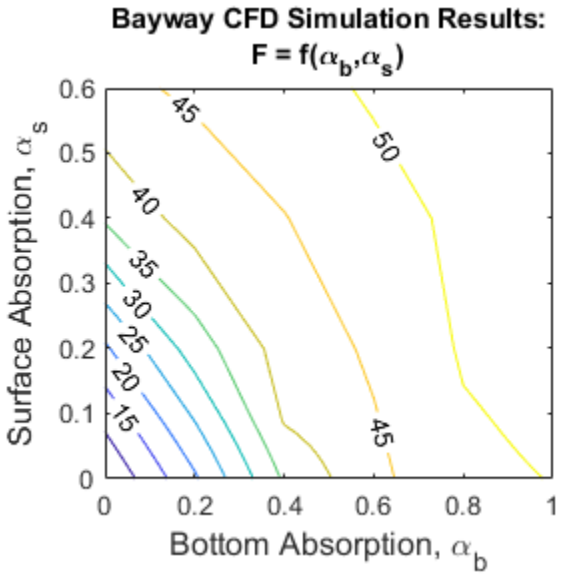

Figure 3-9. Bayway simulation results showing TL coefficient as a function of bottom and surface absorption

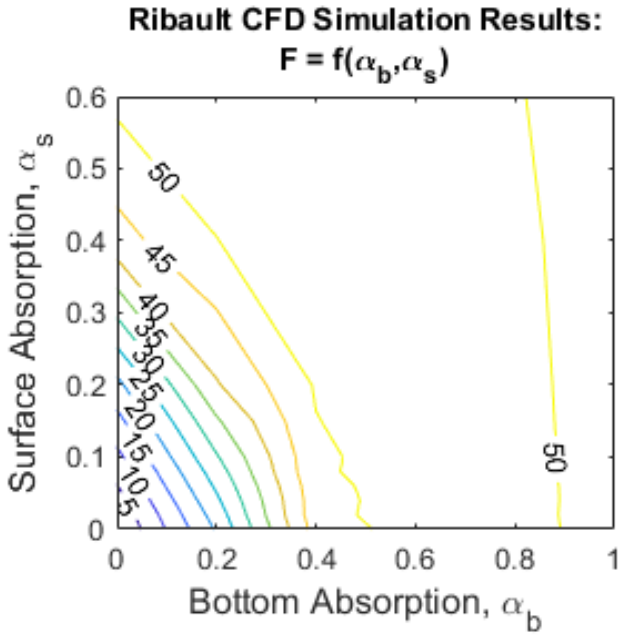

Figure 3-10. Ribault simulation results showing TL coefficient as a function of bottom and surface absorption

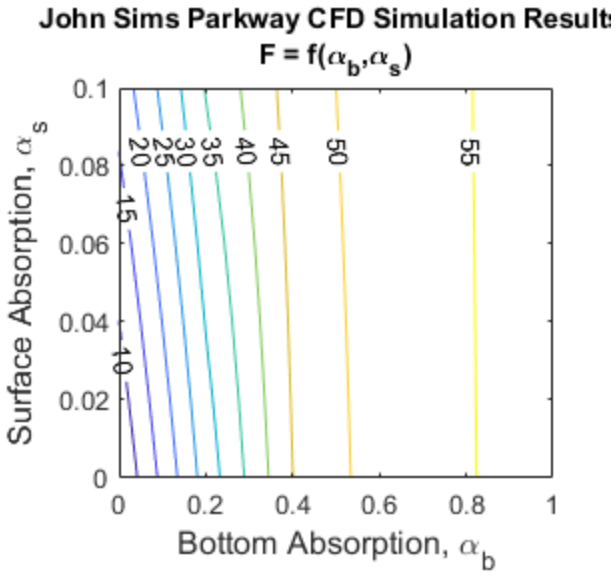

Figure 3-11. John Sims Parkway simulation results showing TL coefficient as a function of bottom and surface absorption

3.5 Discussion

3.5.1 Bottom Absorption Effects on TL Coefficient

Field measurement data from Bayway E site gave a mean TL coefficient of 18. This corresponds to α_b values between 0 and 0.18; and α_s values between 0 and 0.35. If one assumes that the water surface absorbed/lost relatively little acoustic energy as indicated in the literature (i.e., less than 10%), one can use these data to reduce the bottom absorption range to 0.15 to 0.20. In other words, the simulation results indicate that about 17.5% of the acoustic energy was absorbed by the soil at the Bayway E location.

Field data from the Ribault River site gave a mean TL coefficient of 44. This corresponds to α_b values between 0 and 0.39; and α_s values between 0 and 0.45. Making the same assumption as above associated with water surface absorption, data imply that bottom absorption must have ranged from 0.35 to 0.40. Put another way, these preliminary results appear to indicate that 37.5% of the acoustic energy was absorbed by the soil at the Ribault River location. This 37.5% should not be confused with the TL coefficient. Rather, the ~37.5% bottom absorption coupled with

surface absorption of less than 10% superimposed onto the Ribault River location's local bathymetry yielded a TL coefficient of 44.

Field data from the John Sims Parkway site gave a mean TL coefficient of 25. This corresponds to α_b values between 0.09 and 0.18; and α_s values between 0 and 0.1. Again, if water surface absorption is assumed to be small, then these data imply that the bottom absorption coefficient ranged to 0.09 to 0.18. Overall, the likely bottom absorption ranges for each site are tabulated below in Table 3-1:

Table 3-2. Likely Bottom Absorption Ranges

Site Name	Likely Bottom Absorption Range
Bayway E	0.15-0.20
Ribault River	0.35-0.40
John Sims Parkway	0.09-0.18

3.5.2 Geotechnical Analysis

Examination of the boring logs at each of these sites indicated that geotechnical conditions were significantly different at each location – see Fig. 3-12, below:

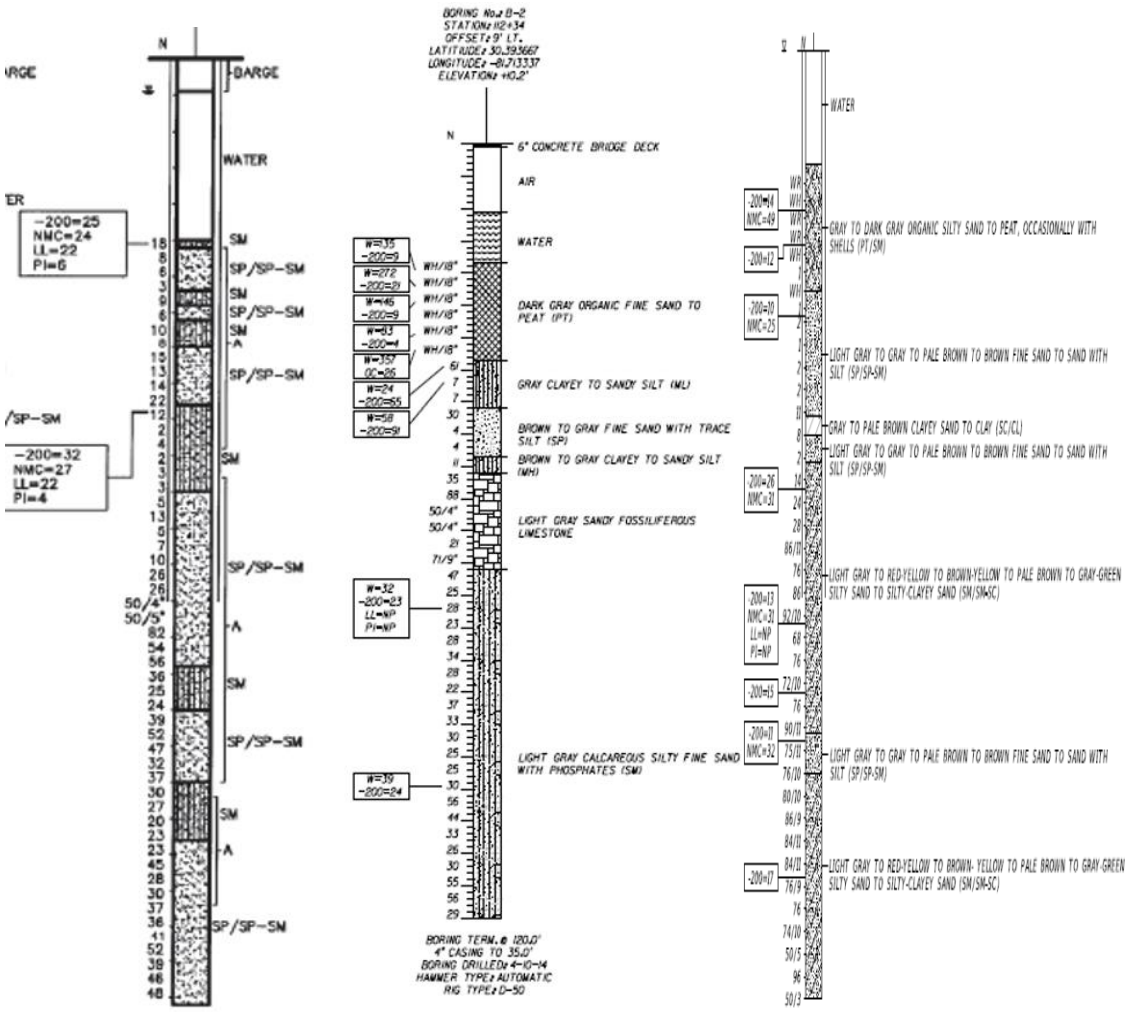

Figure 3-12. Boring log data from Bayway E Bridge (left); Ribault River (middle); and John Sims Parkway (right)

As shown, at the Bayway E site, the surface sediment was classified as SM. Below that, alternating layers of SM and SP/SP-SM were encountered. At the Ribault River site, PT was encountered along the surface of the riverbed. Below that, layers of ML, SP, MH fossilized limestone layer, and a deep SM layer were observed. On the other hand, John Sim's Parkway the top sediment was classified as PT/SM followed by layers of SP/SP-SM, SC/CL, SM/SM-SC, SP/SP-SM and a layer of silty sand to silty clayey sand (SM/SM-SC). Total boring depth was approximately 40 m for the Bayway E river, 35 m for the Ribault River and 32 m for John Sim's Parkway site. Overall, results would appear to indicate that geotechnical conditions may have been

partially responsible for different sound absorption values. And, more generally, the peat and more cohesive sediments at the Ribault River site attenuated more sound that the relatively coarse material at the John Sims Parkway site and the Bayway E Bridge.

3.6 Summary and Conculsions

To summarize, several simulations of hammer blows on piles were performed using varying bottom and surface absorption criteria at three sites in Florida – the Bayway E bridge, the Ribault River bridge and John Sim's Parkway bridge. Table 3-3 summarizes the results.

Results showed that to reproduce observed TL coefficients from field data, different bottom absorption values were required at each site. The geotechnical data at each location from contractor boring logs showed that geotechnical conditions were significantly different at each site. For instance, at the Bayway E site, surface sediments were relatively coarse, while at the Ribault River site, surface sediments were finer and organic materials were encountered. Preliminarily then, one can conclude that based upon these data, the finer and organic sediments attenuated sound more efficiently than the coarser sediments. Or, more generally, one may conclude that it may be possible to correlate geotechnical sound absorption with traditional geotechnical properties like grain size, density, compressive strength, etc. Further analysis showed that physically, a TL coefficient of 15 may sometimes be an oversimplification of field conditions and a more sophisticated sound attenuation model that takes geotechnical conditions into account may more accurately predict TL during pile driving.

CHAPTER 4
ANALYSIS USING EMPIRICAL DATA FITTING

4.1 Introduction and Background Information

Determining underwater TL during pile driving using empirical methods has remained a challenge due to a number of factors discussed in-depth by Ainslie *et al.* (2014). In particular, the current understanding of most TL through fluid media involves point or dipole sound sources. A pile drive is neither because the pile spans the entire water column. In addition, current TL models usually assume a uniform medium, but in the case of the pile drive, this is not true either because sound propagates through the air, water, and soil.

Some have attempted to take these variable sound media conditions into account using more sophisticated empirical or semi-empirical models for sound propagation in shallow water. A good example is the semi-empirical model by Rogers (1981) which was derived from physics-based considerations of energy conservation, ray refraction, surface reflection, bottom reflection, the mode stripping process, geometric spreading and mainstream attenuation. Rogers (1981) points out that for a simple propagation case with a homogeneous fluid bottom, a smooth surface and bottom and a constant sound speed gradient (typical of most pile driving cases observed in Florida), a simple algebraic model may be just as accurate as a more sophisticated numerical model. Rogers (1981) proposed the following model to characterize TL:

$$TL = 15logR + AR + B + CR^2 \tag{4-1}$$

where A, B and C are empirical coefficients and C is usually very small.

More specifically, for cases where sound speed decreases as one moves deeper into the water column (i.e., negative sound speed gradient) with constant sound speed in the water column (isospeed case), Rogers proposed the following expression for TL:

$$TL = 15\log_{10} R + 5\log_{10}(H\beta) + \frac{\beta R\theta_L^2}{4H} - 7.18 + \alpha_W R \quad (4\text{-}2)$$

where:

- R = range (m)
- H = water depth (m)
- B = bottom loss (dB rad^{-1})
- θ_L = limiting angle(rad)
- α_w = absorption coefficient of sea water

The limiting angle (θ_L) is the larger of the maximum grazing angle for a skip distance (θg) and the effective plane-wave angle corresponding to the lowest propagating mode (θc) as follows:

$$\theta_g = \sqrt{\frac{2Hg}{c_w}}\,(\text{rad}) \quad (4\text{-}3)$$

$$\theta_c = \frac{c_w}{2fH}\,(\text{rad}) \quad (4\text{-}4)$$

where g is the magnitude of the negative sound-speed gradient (s^{-1}), and f is the frequency (Hz) and c_w is the maximum sound speed (ms^{-1}). The bottom loss β can be approximated for small values of the limiting angle by:

$$\beta \approx \frac{0.477M_0N_0K_s}{[1-N_0^2]^{\frac{3}{2}}}\ (\text{dBrad}^{-1}) \quad (4\text{-}5)$$

where;

1.

- $N_0 = c_w/c_s$
- $M_0 = \rho_s/\rho_w$
- ρ_w = density of sea water
- ρ_s = sediment density
- Ks = sediment attenuation coefficient (dB m^{-1} kHz^{-1})

The parameter α_w is mainstream frequency-driven wave attenuation and is given by:

$$\alpha_w = 0.001936\left[\frac{0.1f^2}{1+f^2} + \frac{40f^2}{4100+f^2}\right] \quad (4\text{-}6)$$

The Rogers (1981) model was developed primarily for use in shallow water environments by taking into account several bottom sediment properties and a given frequency of propagation. Dawoud et.al (2016) managed to use the model to estimate the

impact of offshore pile driving noise on the Red Sea marine mammals. They used the model to estimate TL and SEL by taking into account seabed bathymetry and sound speed as influenced by temperature and salinity. However, note that impleneting the Rogers (1981) model is difficult because inputs like sound speed through soil and sediment attenuation coefficients are required as inputs. These variables may be difficult to measure and could vary considerably even within a given jobsite.

Weston (1971), Ainslie (2010), and Ainslie *et al.* (2014), pointed out that Eq. 1-5 is derived from the exact solution for cylindrical spreading for a point source far from a boundary at frequencies above the cutoff frequency. The exact solution to this situation is:

$$\mathrm{TL} = 15\log_{10}\left(\frac{r}{r_0}\right) + 5\log_{10}\left(\frac{\eta H}{\pi r_0}\right)^{\frac{1}{2}} \tag{4-7}$$

Ainslie *et al.* (2014) point out that the practical spreading loss model Eq. 1-5 is simply a special case of Eq. 4-7 where A is assumed to equal zero which implies that $\eta H = \pi r_0$. More generally then, the full equation for underwater TL is:

$$\mathrm{TL} = A\log_{10}\left(\frac{r}{r_0}\right) + B \tag{4-8}$$

And, in the case of Eq. 4-7, $B = 5\log_{10}\left(\frac{\eta H}{\pi r_0}\right)^{\frac{1}{2}}$ while $A = 15$.

Ainslie *et al.* (2014) go on to provide several other examples where A and B from Eq. 4-8 are computed for situations other than point sources far from boundaries above the cutoff frequency including transient and dipole sources. In each solution, some value of A from Eq. 4-8 is derived along with a term or terms that comprise B. These solutions imply that A and B must be co-dependent and interrelated. More recently, Lippert *et al.* (2018) provided an analytical solution of the form of Eq. 4-8 that accounted for the line-source associated with a pile drive:

$$\mathrm{TL} = 10\log_{10}\left(\frac{r}{r_0}\right) + \alpha(r - r_0) \tag{4-9}$$

where α is a decay factor given by:

$$\alpha = 10\log_{10}\frac{R^2}{2H\cot\phi + \Delta l} \tag{4-10}$$

In Eq. 4-10, R is a power reflection coefficient defined by the squared magnitude of the reflection factor between water and soil; ϕ is the angle from which sound leaves the pile derived from the ratio between sound speed through the pile and sound speed in water – see Reinhall and Dahl (2011b) for details; Δl is the horizontal beam shift described in detail by Weston (1994); and H is the water depth. Martin and Barclay (2019) pointed out that Eq. 4-9 may be further generalized:

$$L_r = C - A\log_{10}\left(\frac{r}{r_0}\right) + B(r - r_0) \tag{4-11}$$

In Eq. 4-11, L_s has been replaced by a constant, C, that is not necessarily a source term, but rather, according to Martin and Barclay (2019) depends on project-specific conditions such as strike energy (SE), the coupling of hammer energy into the pile, and the damping of pile vibrations by the sediment. See Lippert *et al.* (2016) and MacGillivray (2013) for additional details. The B-term in Eq. 4-11 is due to multiple reflections between the seabed and surface while the A-term is due to bottom composition, the water-column sound speed profile, surface roughness, and seabed roughness. Martin and Barclay (2019) go on to present their own model that is a function of SE; pile penetration, PP; and the angle between the pile and the receiver, θ:

$$TL = A\mathrm{SE} + B\mathrm{PP} + Cr + D\cos\theta + E(r, \cos\theta) - 10\log_{10} r + \alpha r \tag{4-12}$$

In Eq. 4-12, α was found to be frequency dependent similar to Rogers' (1981) α value.

The Martin and Barclay (2019) and Lippert *et al.* (2018) studies both represent breakthrough leaps in terms of overall understanding of the anthropogenic sound

transmission due to pile driving issue. However, while Lippert *et al.* (2018) provide a physically-based approach for determining underwater TL, the authors reported that field testing with their model (i.e., Eq. 4-9 and Eq. 4-10) showed that errors may be as high as 33%. To improve upon this, presumably, one could utilize Eq. 4-11, but this would require calibration of Eq. 4-11's *A, B,* and *C* coefficients. The Martin and Barclay (2019) model (i.e., Eq. 4-12) and even the general shallow water model by Rogers (1981) (Eq. 4-1) have a similar issue in the sense that they requires calibration of Eq. 4-12's *A, B*, *C*, *D*, and *E* coefficients or Eq. 4-1's *A,B* and *C* coefficients. Martin and Barclay (2019) recommend logarithmically spacing at least four recorders during pile driving operations to perform this calibration.

4.2 Goals and Objectives

The goal of the work presented herein was to simplify the approaches presented by Martin and Barclay (2019) and Lippert *et al.* (2018) and develop a simple, easy to implement model for predicting underwater TL that requires no calibration. In particular, this study sought to leverage the interdependency between *A* and *B* from Eq. 4-8 that was discussed in-depth by Ainslie *et al.* (2014). The current standard for estimating TL during pile driving (i.e., Eq. 1-5) presumes that sound-level is known at one location during pile driving. Thus, a similar approach was taken throughout this study in the sense that it was assumed that like NOAA (2021), SPL was known at one location during pile driving operations. Two techniques were used throughout this study – first, Rogers' (1981) model was calibrated using the field data collected during this study. Secondly, a new model that takes advantage of the interplay associated with the various TL terms was developed.

4.3 Methodology

4.3.1 Rogers (1981) Model Calibration

A 10th order z-weighted digital filter with 1 octave bandwidths was used to group the sound signal into frequency bands from 1 Hz to the Nyquist frequency associated with a 48 kHz sampling rate (i.e., 24 kHz) as per ANSI S1.11 (Acoustical Society of America, 2009) using the built-in 'octavefilterbank' tool in MATLAB. This resulted in 15 octave bands where sound was grouped. Next, TL was computed at various ranges during each drive event by subtracting sound-level data collected at one distance from each pile from sound-level data collected at another distance from each pile. Then, a cut off frequency was calculated for each site. The cutoff frequency assumes that no propagation modes can exist in the water column below the cutoff frequency (Jensen et al., 2011) and is given by:

$$f_c = \frac{\pi - \frac{\rho_S}{\rho_W}}{2\pi \sin\left(\cos^{-1}\left(\frac{c_W}{c_S}\right)\right) \times \frac{c_W}{H}} \tag{4-13}$$

Geotechnical data were used to compute the appropriate Rogers (1981) model coefficients while octave bin centerpoints were used to compute the Rogers frequency-dependent sound decay. The result was a direct application of the Rogers (1981) model equations. These data for predicted TL were compared to measured field data.

Results (please see below) showed that the Rogers model reproduced field rather poorly. In an attempt to salvage the Rogers model, an error term was defined as the difference between the Rogers model predicted TL and the measured TL. This term was added to the Rogers model to yield a new formulation for TL:

$$TL = 15\log_{10} R + 5\log_{10}(H\beta) + \frac{\beta R \theta_L^2}{4H} + \alpha R + 7.18 + E \tag{4-14}$$

in which:

$$E = TL_{Field} - TL_{Rogers} \tag{4-15}$$

Then, a multi-dimensional curve fitting tool (Cepowski 2017), was used to fit E as a function of other variables associated with the pile drives – specifically, f, R, β, and H. These results produced a model that was used to back-calculate TL and compare to measured TL to assess performance of the new calibration term.

4.3.2 Development of a New Empirical Model for TL

A new empirical model for computing underwater TL during pile driving was also developed during this study. This new model took advantage of the interplay between A and B in Eq. 4-8 that was pointed out by Ainslie (2014). Starting with Eq. 4-8 in terms of the sound-level at the pile (L_s) and sound-level at some range, r (L_r):

$$TL = L_s - L_r = A \log_{10}\left(\frac{r}{r_0}\right) + B \tag{4-16}$$

This equation was rearranged:

$$L_r = (L_s - B) - A\log_{10}\left(\frac{r}{r_0}\right) \tag{4-16}$$

For each drive event, if curves of the form:

$$y = a \log_{10} x + b \tag{4-17}$$

are fit to sound-level data as a function of range, then a must correspond to $-A$ while b must correspond to $(L_s - B)$. But, as discussed above, a and b must be co-dependent which means that A and $(L_s - B)$ must also be co-dependent. As such, a correlation could be developed between A and $(L_s - B)$ using linear regression. This was conducted for each a and b combination associated with SEL, RMS, and Peak data during each drive event.

4.4 Results

4.4.1 Rogers Model Calibration Results

This section shows the results obtained from calibration of Roger's model by data fitting. Fig. 4-1 shows the results of curve fitting of E from Eq. 4-14 as a function of frequency, bottom loss, water depth and range using a multidimensional curve-fitting tool.

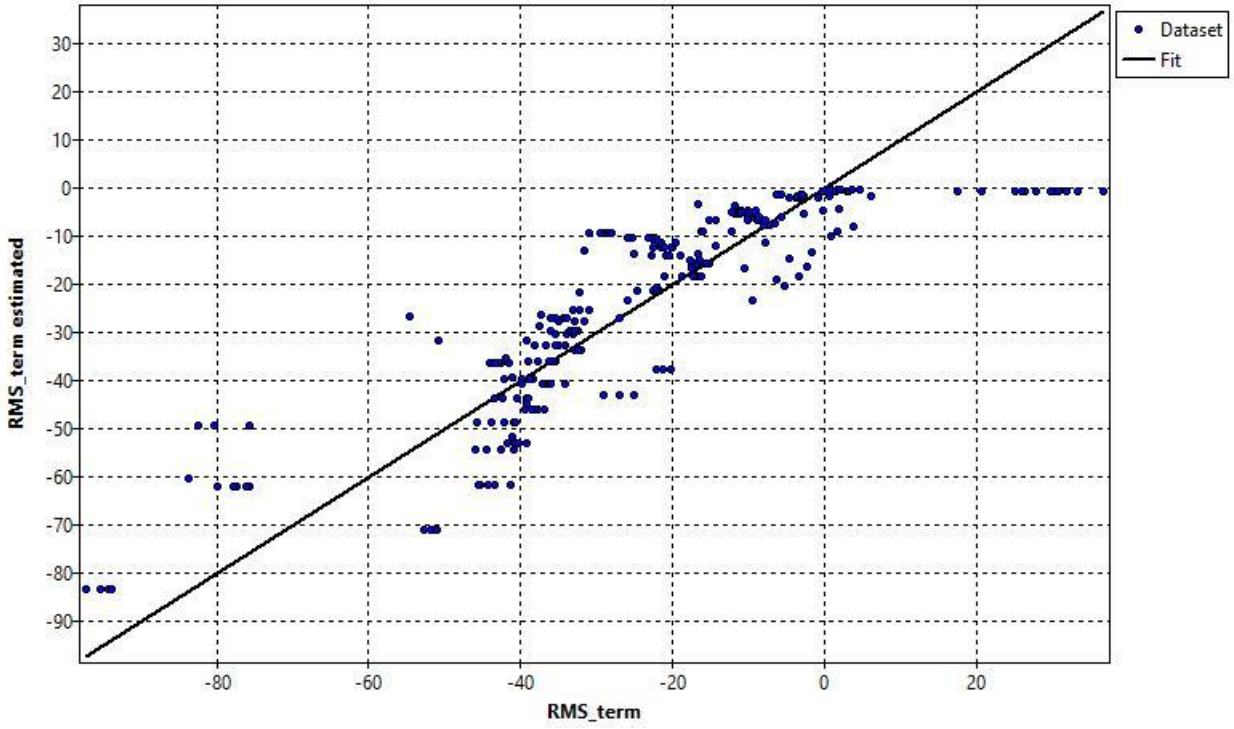

Figure 4-1. Multidimensional curve fit between E and f, R, β, and H

The estimated function for E is given by:

$$E = a_1 (\log_{10} f)^{0.37} R^{0.15} \beta^{-0.9} H^{0.55} + a_2 (\log_{10} f)^{\frac{1}{19}} R^{0.99} \beta^{\frac{1}{17}} \quad (4\text{-}18)$$

where $a_1 = 6.66$ and $a_2 = -0.0096$. Adding this term to Rogers model predictions produced the calibrated model's results. The following figures illustrate how the PSLM, Uncalibrated Rogers Model and the Calibrated Rogers model perform in predicting TL:

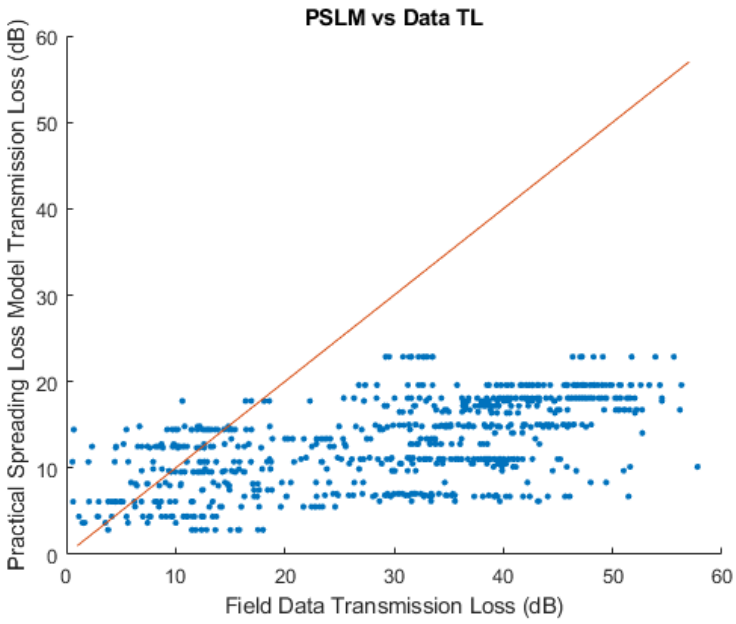

Figure 4-2. Results of TL from applying the PSLM (Eq. 1-5) to data directly vs measured TL

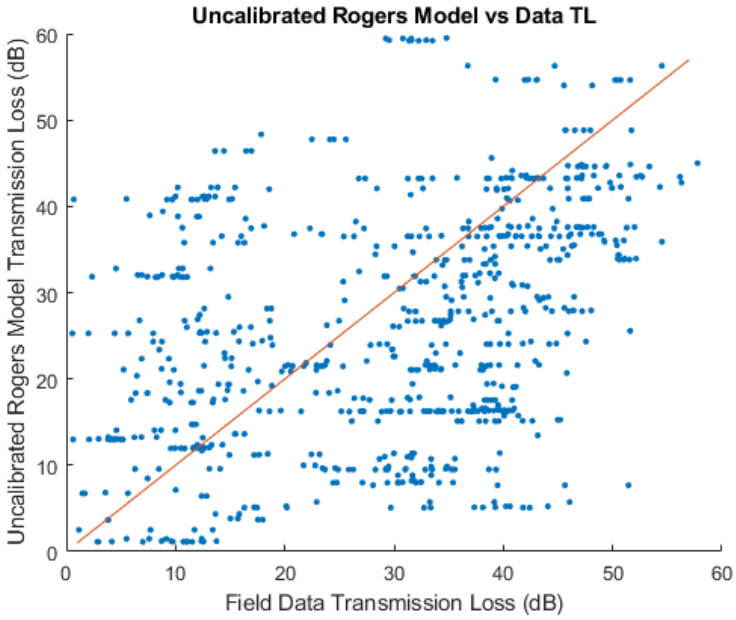

Figure 4-3. Results of TL from applying the Rogers model (Eq. 4-2) to data directly vs field TL

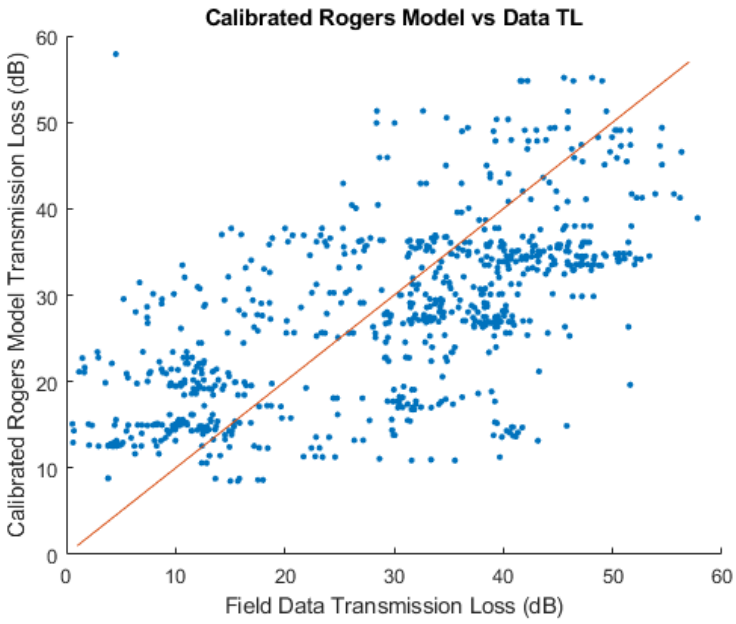

Figure 4-4. Results of TL from applying the Calibrated Rogers model (Eq. 4-14) with the additional term (Eq. 4-18) to data directly vs field TL

4.4.2 New Model Results

Logarithmic decay curves from field data for RMS, SEL and Peak sound-level for each drive event are shown below from Fig. 4-5 to Fig. 4-10. In each of these curves, circles are used to denote the result of each statistical compuatiaon (i.e., RMS, SEL, or Peak) at each buoy location while the logarithmic decay curves represent best-fit curves discussed in Eq. 4-17. Fig. 4-11 shows the apparent dependency between $(L_s - B)$ and A discussed above.

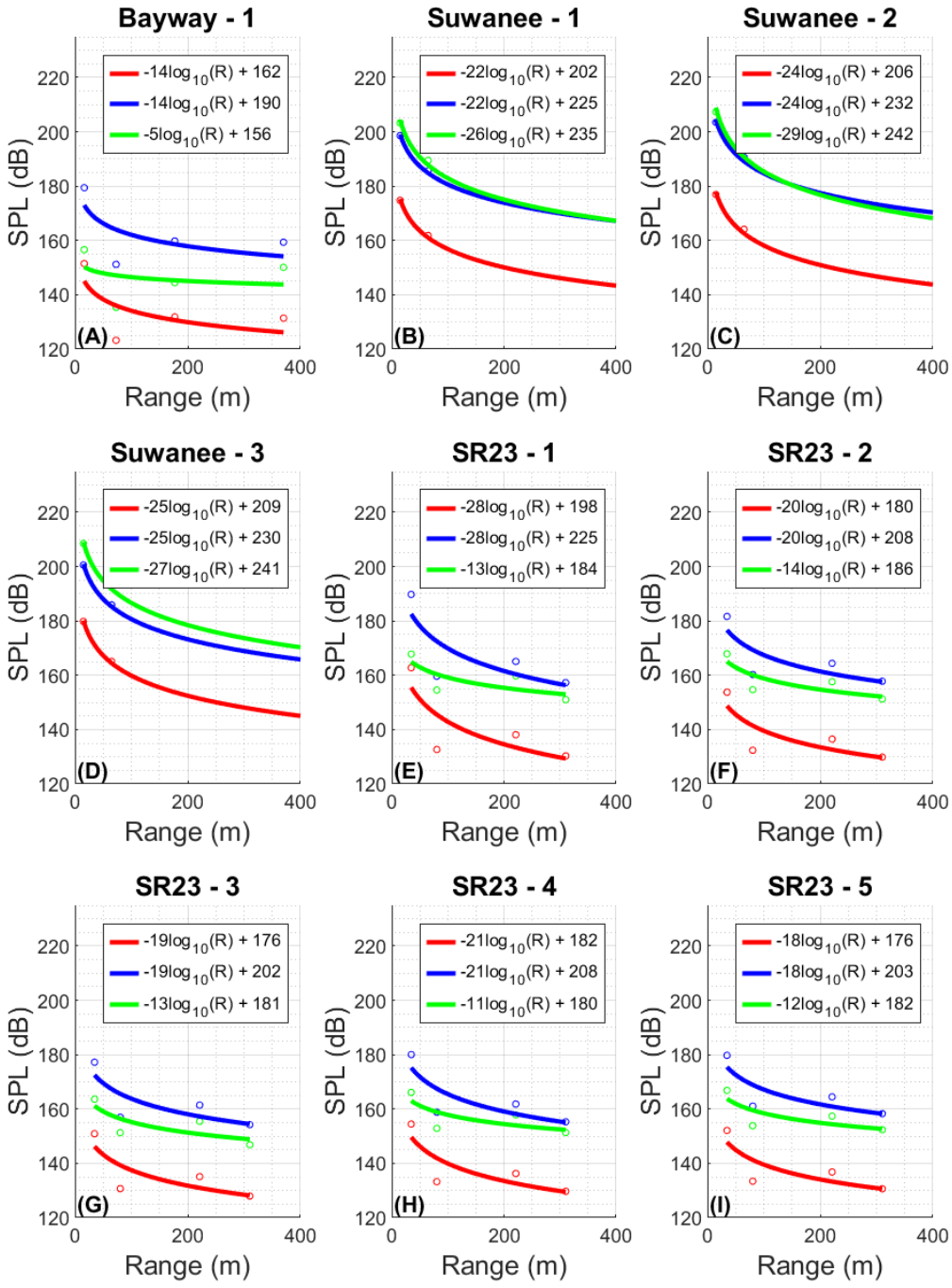

Figure 4-5. RMS(Red), SEL(Blue) and Peak (Green) decay curves for Bayway, Suwanee and SR23 drives

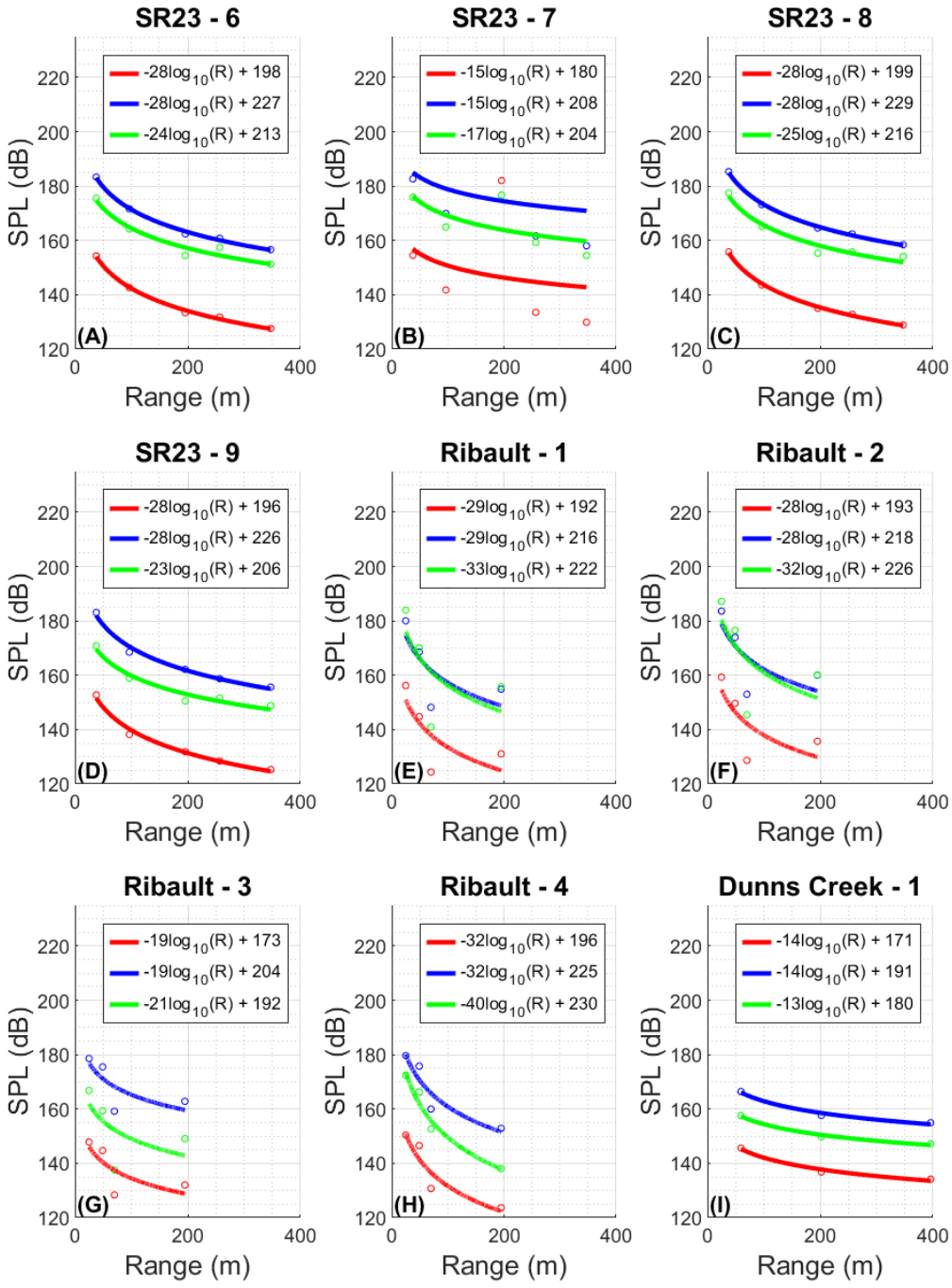

Figure 4-6. RMS(Red), SEL(Blue) and Peak (Green) decay curves for SR23, Ribault and Dunns Creek drives

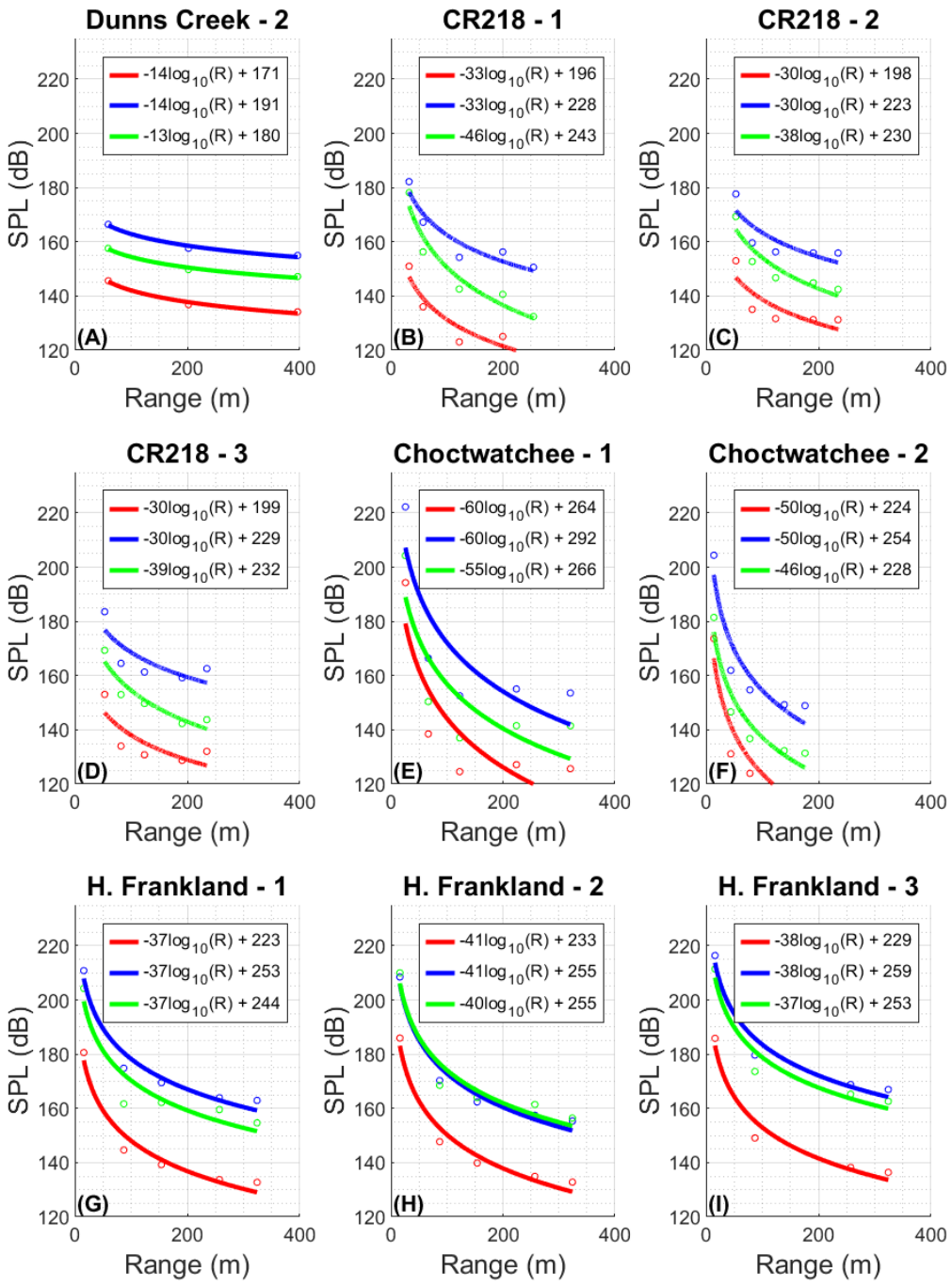

Figure 4-7. RMS(Red), SEL(Blue) and Peak (Green) decay curves for Dunns Creek, CR218, Cochtwatchee and Howard Frankland bridge drives

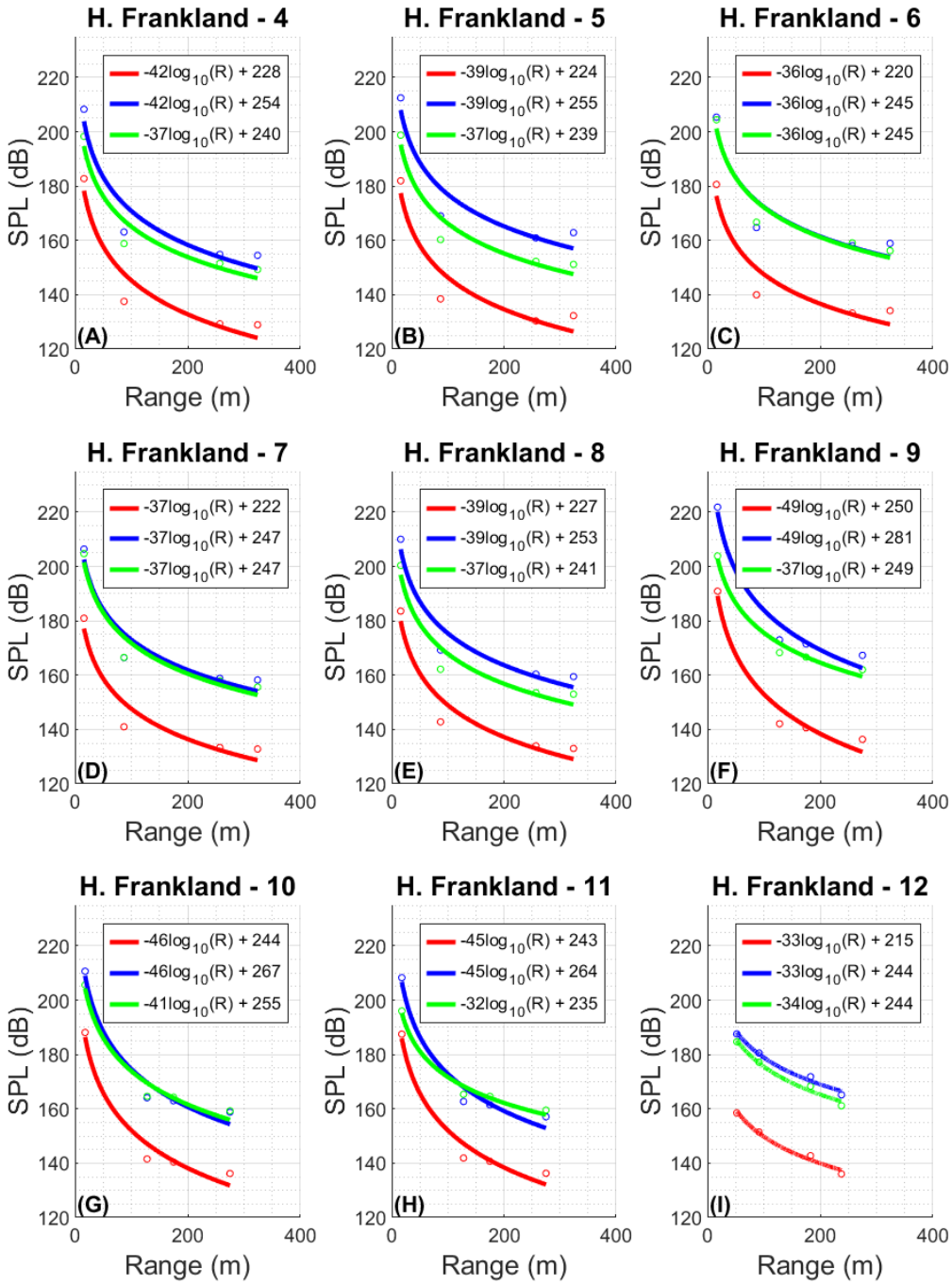

Figure 4-8. RMS(Red), SEL(Blue) and Peak (Green) decay curves for Howard Frankland bridge drives

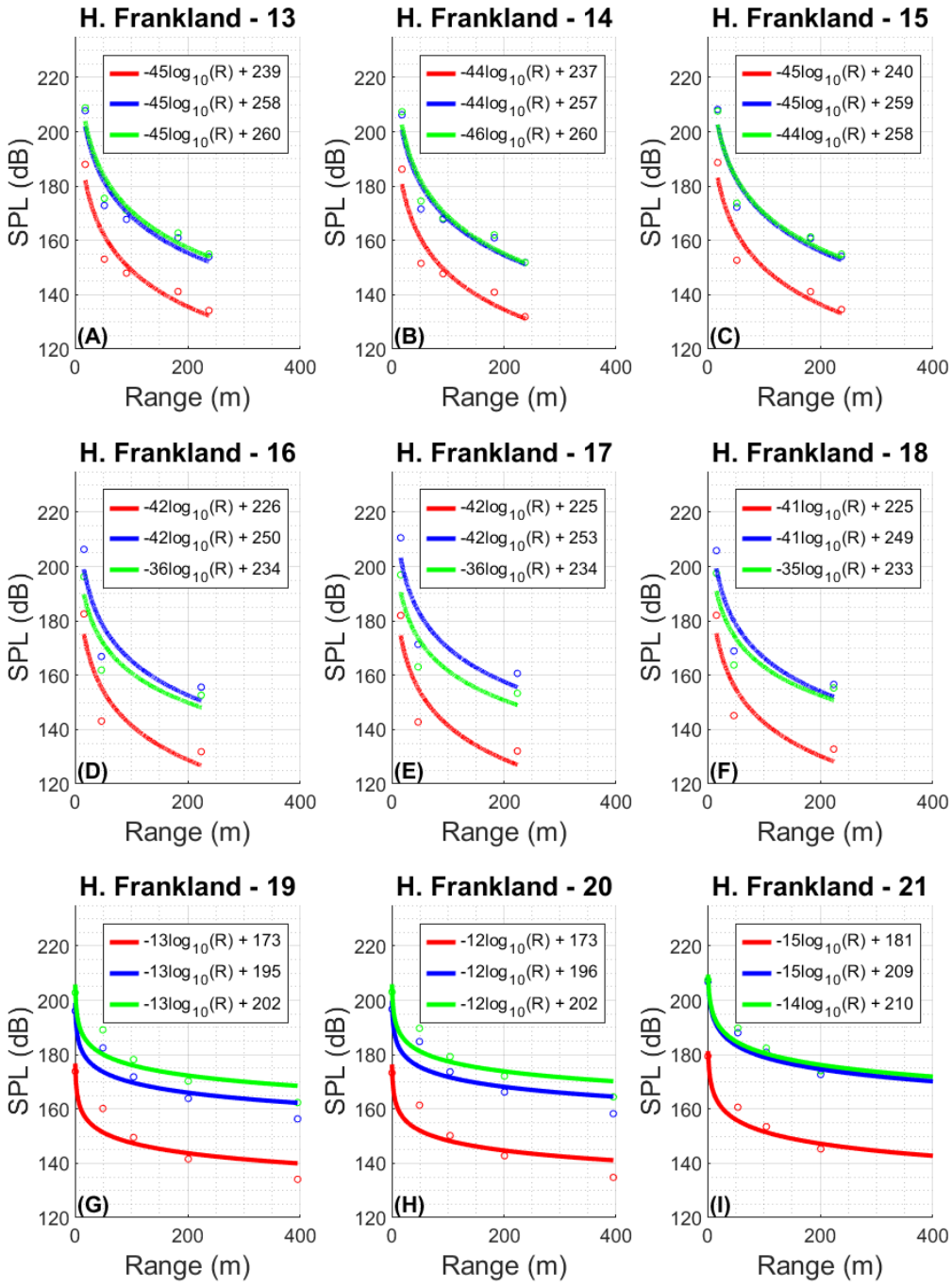

Figure 4-9. RMS(Red), SEL(Blue) and Peak (Green) decay curves for Howard Frankland bridge drives

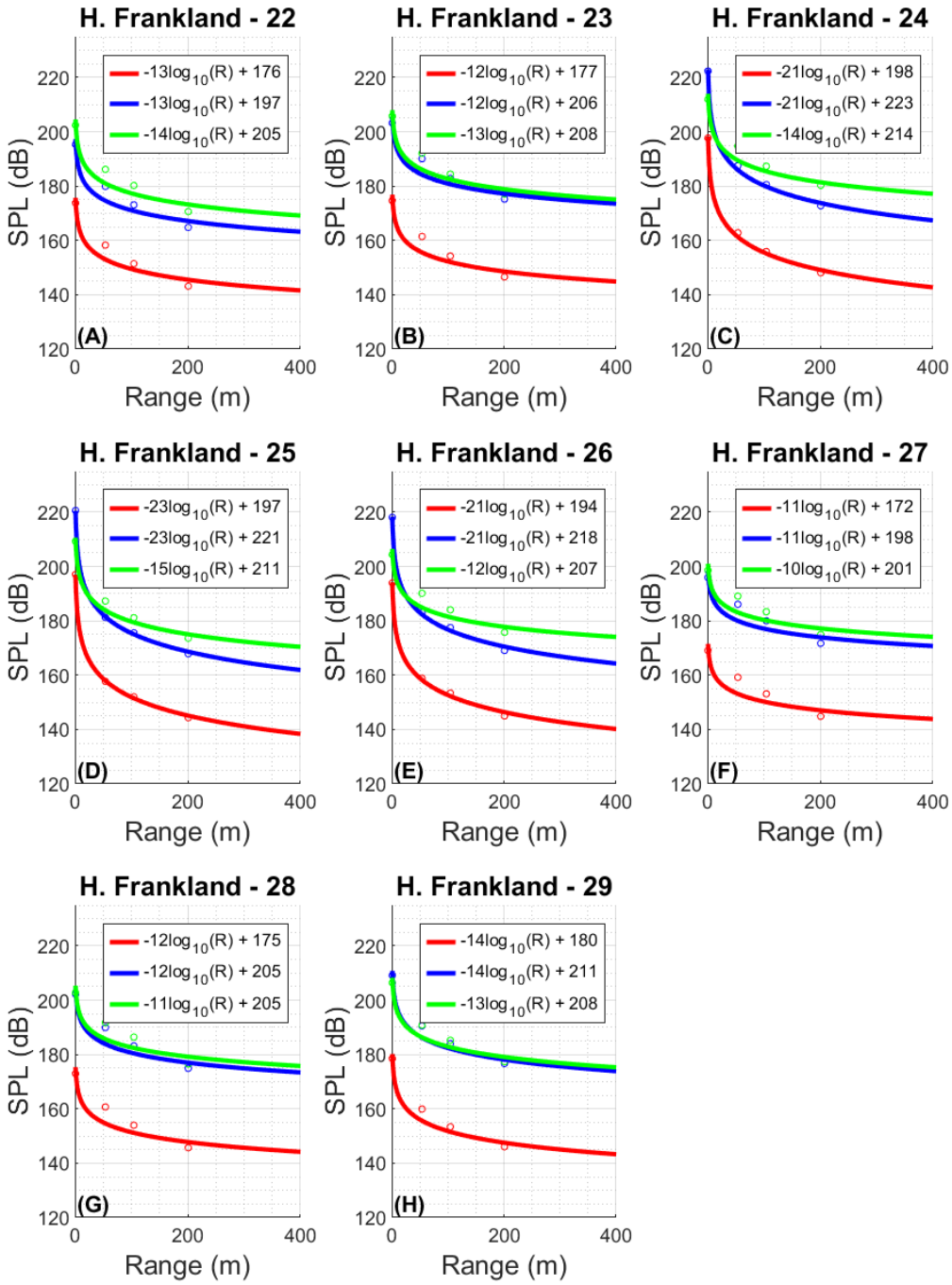

Figure 4-10. RMS(Red), SEL(Blue) and Peak (Green) decay curves for Howard Frankland bridge drives

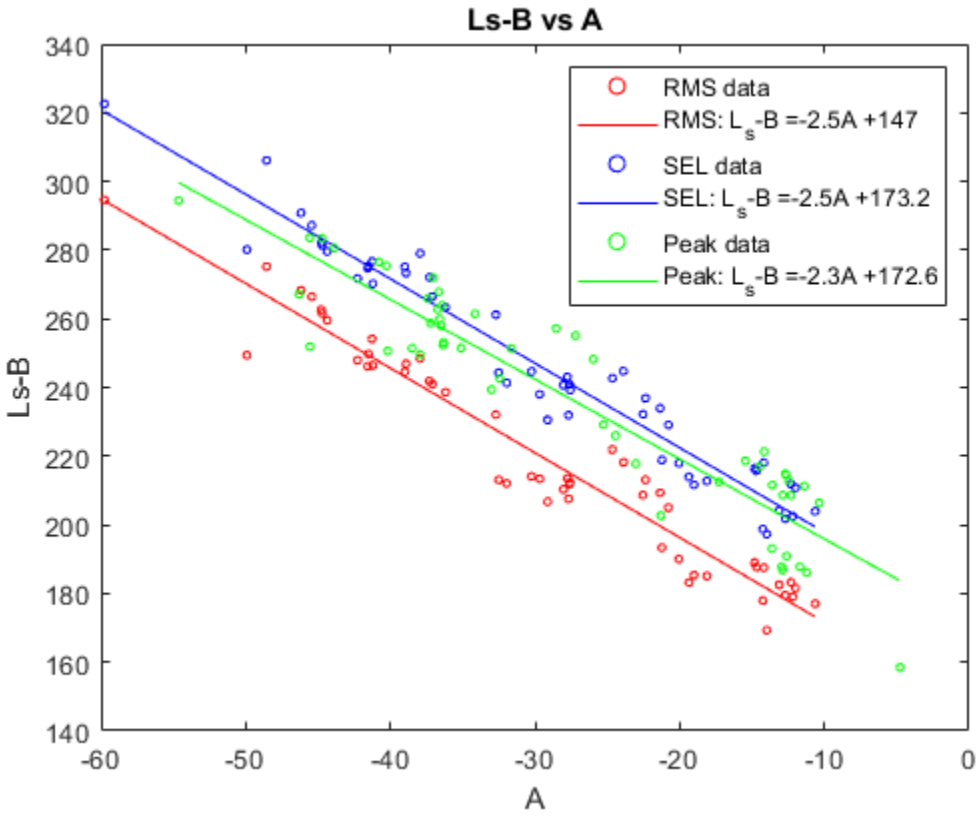

Figure 4-11. Regression lines for Ls-B vs A for RMS, SEL and Peak data

4.5 Discussion

4.5.1 Rogers Model Calibration

As shown in Fig. 4-2, the PSLM usually performs very poorly and consistently underestimates TL. The Rogers model performs more unpredictably in the sense that it may overpredict or underpredict TL as shown in Fig. 4-3. In addition, no strong correlation between modeled results and the data was observed. The addition of the term E from Eq. 4-18 resulted in a slightly improved model as shown in Fig. 4-4.

Overall, the results from these calibration attempts were very crude. However, enveloping the model may be an improvement over when compared to the PSLM, since, as shown in Fig. 4-2, the PSLM also performs very poorly when compared to field data. Improving results beyond this using the Rogers formulation may be impossible because of the overabundance of parameters associated with the model.

4.5.2 The New Empirical Model

As shown in Fig. 4-5 through Fig. 4-10, equations of the form of Eq. 4-19 appeared to fit SPL data well with average R^2 values of 0.8519 for RMS, 0.8519 for SEL and 0.8418 for Peak data. In addition, analysis of Fig. 4-11 appears to show strong correlation between a and b with R^2 values of 0.9438 for RMS, 0.9479 for SEL and 0.8710 for Peak. Thus, by extension, a strong correlation appears to be observed between A and $(L_s - B)$.

The relationships in Fig. 4-11 may be usable as a practical, empirical model to predict SPL decay as a function of distance. Similar to guidelines present by NOAA (2021), if one knows the sound-level at one location during pile driving, then Fig. 4-11 may be used to estimate A based upon this reading. Then, by extension, Fig. 4-11 may be reused to solve for the sound-level at some distance. Or, conversely, the distance required to meet some design threshold may be easily computed.

For example, suppose that during pile driving, one measured a Peak SPL of 220 dB at 20 m from the pile and was interested in determining the distance required to get below the peak threshold for fish injury, which according to NOAA (2021) is 206 dB. Using the NOAA method, one would simply rearrange the PSLM to: $r = 10^{\left[\frac{Ls-Lr}{15}\right]} r_0$. Then, the range required to get below peak is then $r = 10^{\left[\frac{220dB-206dB}{15}\right]} 20m = 176\ m$.

Using the same information, with the new method, Eq. 4-8 may be rearranged using the regression information from Fig. 4-11:

$$L_m = a_1 A + a_2 - A \log_{10}\left(\frac{r}{r_0}\right) \tag{4-19}$$

where L_m is the measured SPL and a_1 and a_2 are the regression line coefficients from Fig. 4-11 for the statistic of interest (i.e., Peak, SEL, or RMS). Rearranging this gives,

$$A = \frac{L_m - a_2}{a_1 - \log_{10}\left(\frac{r}{r_0}\right)} \tag{4-20}$$

Once A is obtained, Eq. 4-21 may be reused to solve for *r*:

$$r = \left[10^{\frac{a_1 A + a_2 - L_t}{A}}\right] r_0 \tag{4-21}$$

Substituting:

$$A = \frac{220dB - 172.6dB}{2.3 - \log_{10}\left(\frac{20m}{1m}\right)} = 47.45$$

$$r = \left[10^{\frac{2.3(47.45) + 172.6dB - 206dB}{47.45}}\right] 1m = 39.45\ m$$

Similarly, one could use the new model to compute a sound statistic of interest for at all the ranges from a pile drive as shown below in Fig. 4-12 for the same example inputs used in the problem above. The new model shows the SPL at the pile may be higher than predicted by the PSLM. But, the new model also implies that sound attenuates much more

quickly than predicted by the PSLM. This faster attenutaiton is attributed to the model's *B*-value, and, as shown in Fig. 4-12, this difference in attenuation between the PSLM and the new model is, at least somewhat, range-depdendent.

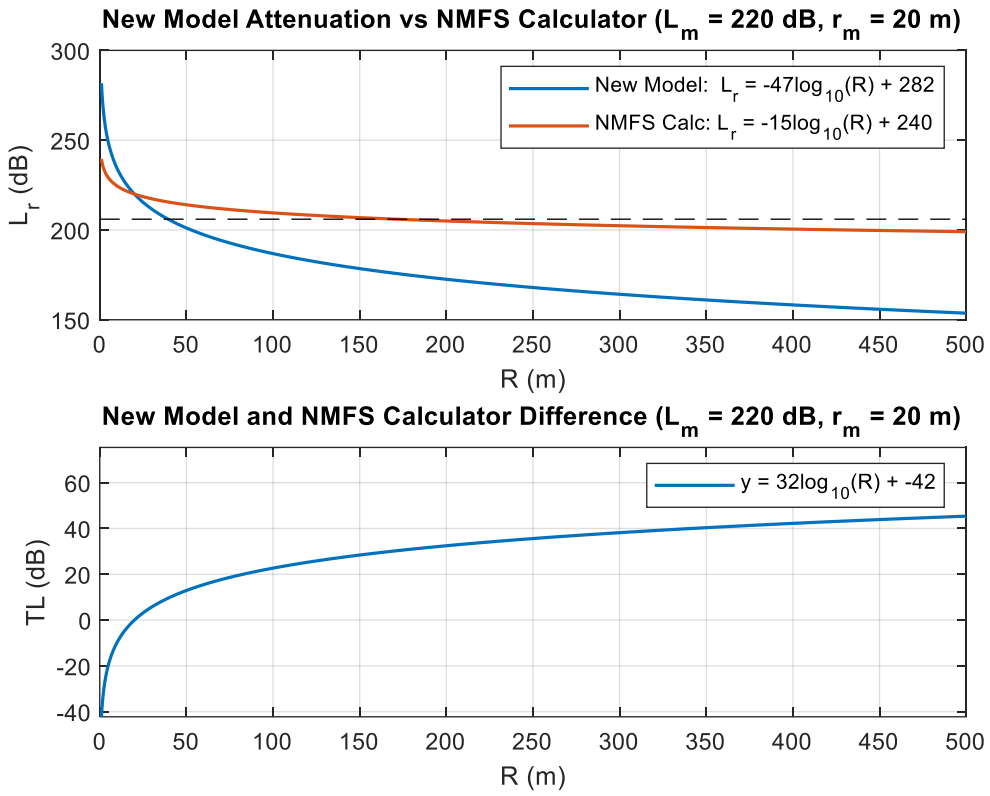

Figure 4-12. Comparison of predictions of the new model with the NMFS Calculator based on the PSLM for a SPL 220 dB measured at 20m from the pile source

The new model was further examined in the context of its calibration data. Fig. 4-13, below shows average peak decay curves from each of the data collection sites, and these curves are color-coded based upon pile type. Generally, impact driving concrete piles resulted in higher sound-levels near the pile but also exhibited very fast attenuation. Conversely, impact driven steel piles displayed relatively average sound-levels near the pile, but the attenuation associated with impact driving steel piles was consistently slower than it was for concrete piles. Vibrational driving produced the least noise. Attenuation associated with vibrational driving was faster than it was during steel impact driving but

was not as extreme as driven concrete attenuation. Overall, these data suggest that the pile type (or possibly the hammer energy) influences attenuation.

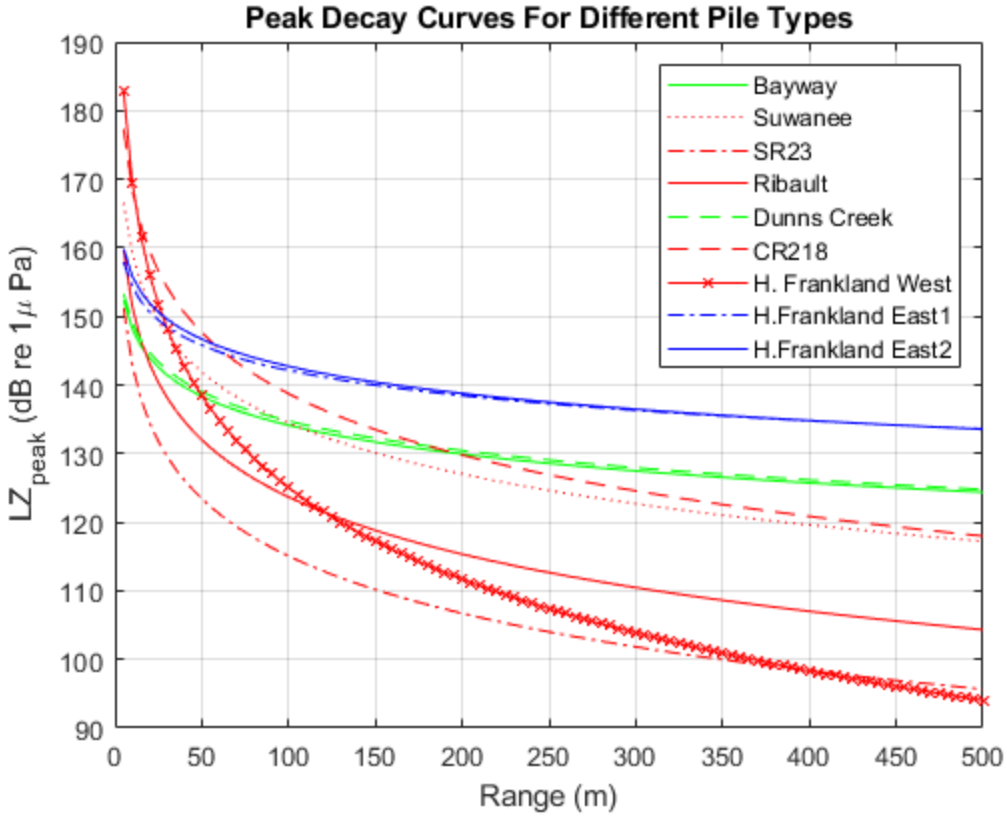

Figure 4-13. Decay curves for sites with different pile types; Red – Concrete Piles Impact Driving; Blue – Steel Piles Impact Driving; Green – Vibration Driving

This concept was further illustrated by replotting Fig. 4-11 as a function of pile-type as shown below in Fig. 4-14 thorugh Fig. 4-16:

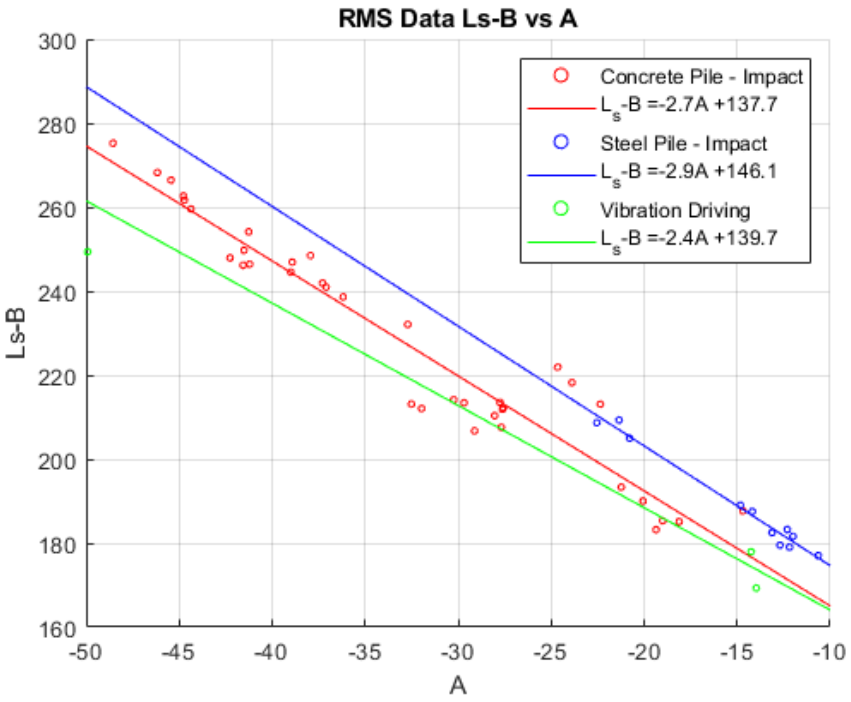

Figure 4-14. RMS Regression lines for Ls-B vs A for different pile types

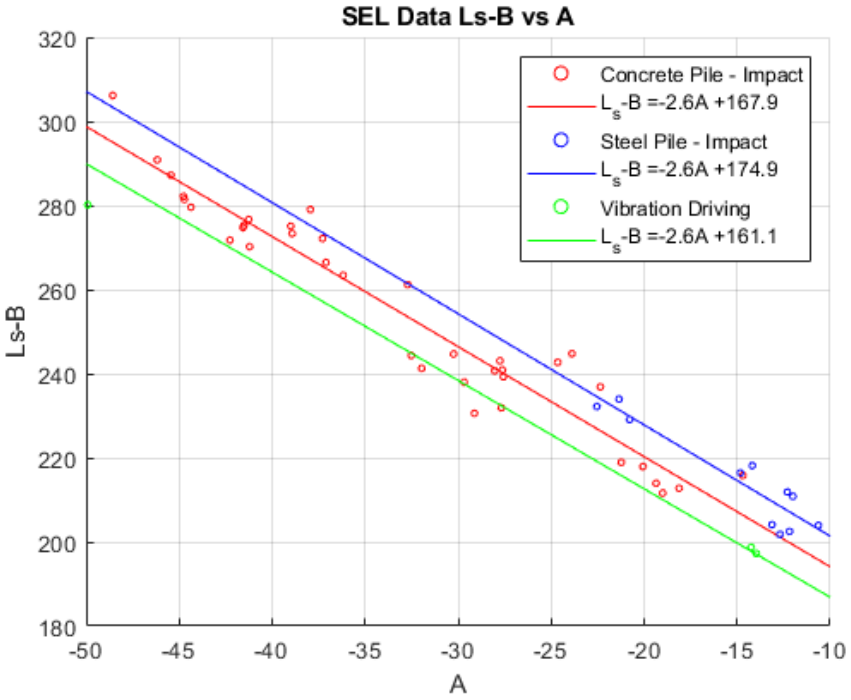

Figure 4-15. SEL Regression lines for Ls-B vs A for different pile types

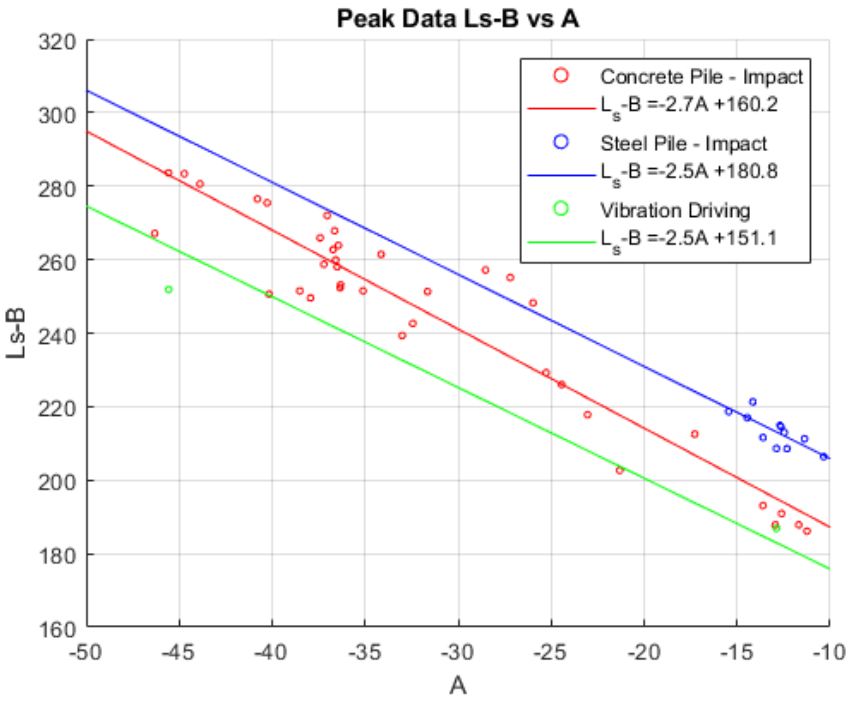

Figure 4-16. Peak Regression lines for Ls-B vs A for different pile types

As shown, there appears to be some relationship between pile-type (or again, possibly hammer energy) and the interplay between A and $(L_s - B)$. Generally, for a given value of $(L_s - B)$, vibratory driving has the highest A-value; impact driving steel piles has the lowest A-value; and impact driving concrete piles falls somewhere in between these two extremes. Despite this, in all cases, the relationship between attenuation variables is similar in the sense that an inverse relationship between $(L_s - B)$ and A was observed.

Finally, it is interesting to note that the new model implies that attenuation is somehow amplitude dependent as shown below in Fig. 4-17.

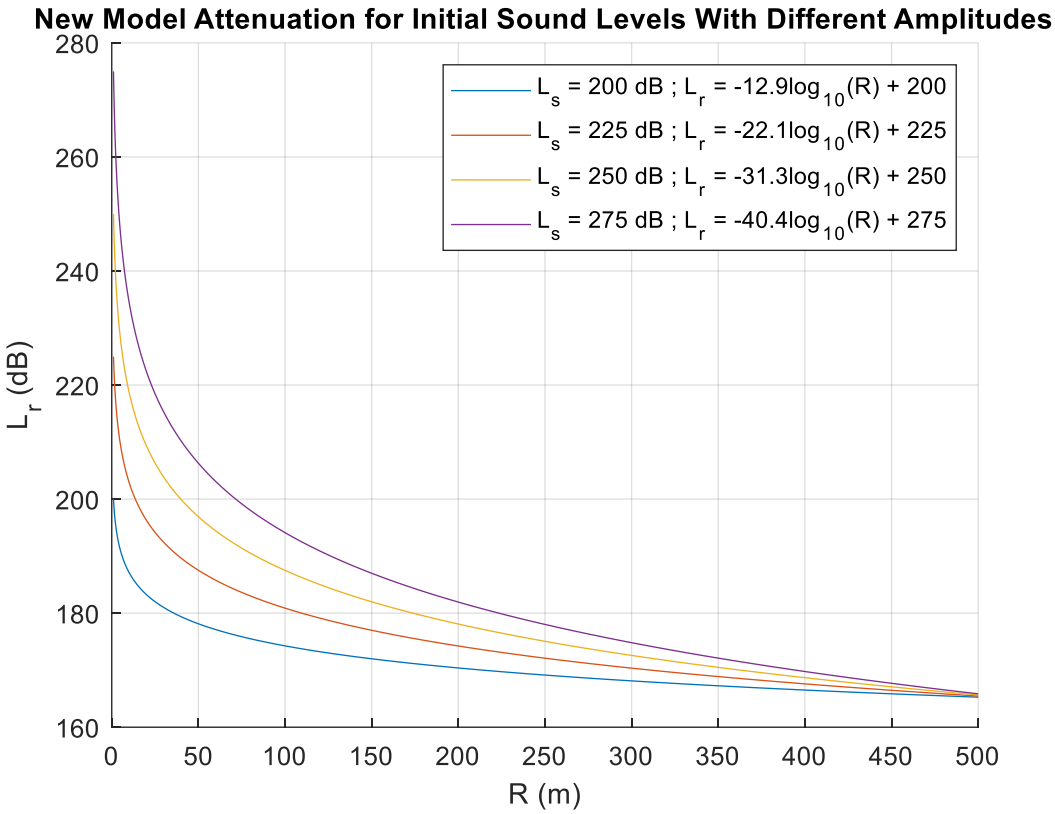

Figure 4-17. Sound TL with range for sources with different amplitudes at a given location

As shown in this figure, at a given range, the new model implies that higher amplitude initial sound-levels will attenuation more quickly than lower amplitude initial sound-levels. This is somewhat counterintuitive and is currently under further investigation because there is no known physical reason for this. There is a very well-known dependency between attenuation and sound freqeucny, so it is possible that this apparent amplitude dependency is really just a frequency dependency that is manifesting somehow as a function of amplitude.

4.6 Summary and Conclusions

The proposed new method indicates that sound attenuates more quickly than suggested by the PSLM. Thus, design thresholds may be exceeded over shorter distances from a given pile drive. The proposed new method has an advantage of being derived from

an empirical data fitting of a large set of data collected in Florida waters, and thus, may be more suitable for use under Florida geotechnical conditions than the PSLM.

Of course, the method presented here is not without its shortcomings. Most troubling, while data suggest that this method is useful from a practical perspective, the method presented is almost completely empirical. As such, while the concept of physical concept of geometrical spreading is somewhat manifested in the base-10 logarithmic decay associated with *A*, this manifestation is only ancillary. Ainslie et al. (2014) pointed out that it is very likely that the *B*-term used throughout this model is also some other range-dependent variable, and indeed, analysis of this model shows this range-dependcy. Mathematically:

$$TL = C\log_{10}\left(\frac{r}{r_0}\right)^{k_1} + D\log_{10}\left(f(?)\left[\frac{r}{r_0}\right]^{k_2}\right) \qquad (3\text{-}18)$$

Thus, the k_1 and k_2 exponents may be redistributed to C and D, or, mathematically, they may "hide" in the A-value. In the expression above, $f(?)$ represents "other" attenuation that must be responsible for the attenuation observed in B but whose physics remains unclear.

As discussed in Chapter 1, Rogers (1981) pointed out that attenuation may be due to 24 variables that include water depth, sound speed profile which is influenced by temperature and salinity, acoustic attenuation in water, for each sediment layer present; density of sediment, sound speed in sediment, shear speed in sediment, acoustic attenuation in sediment, shear attenuation in sediment, sound speed gradient in sediment layers, shear speed gradient in sediment, attenuation gradient in sediment, density gradient in sediment, thickness of sediment layer, sound speed in basement, shear speed in basement, density of basement, acoustic attenuation in basement, shear attenuation in basement, surface

roughness, bottom roughness, sub bottom roughness, entrained gas bubbles, fish and other biological scatterers and lastly wind vector. The *B*-values associated with the new proposed model may be any combination of these 24 variables. Thus, the *D*-term in Eq. 3-18 may be a combination of several terms, each of which may have some range-dependency. In future work, one could likely improve the model presented here by better parameterizing the "other" attenuation into some physically meaningful term or terms and this would likely improve results to some extent.

It is also troubling that, with the current incarnation of this model, it is impossible to say exactly why A and $(L_s - B)$ appear to be correlated in the sense that L_s was not measured during any drive. i.e.., investigators did not place a hydrophone on or very close (within 1 meter) of the pile. As such, it is impossible from these data to determine the "source term" associated with the pile drive. Thus, one cannot determine if A and B are directly correlated (although Ainslie et al. 2014 indicate that they should be) or if the correlation observed here is also a function of the initial noise-level associated with the pile drive. In other words, does a louder drive inherently imply more attenuation. Future work could also be aimed at answering this lingering issue.

CHAPTER 5
OVERALL SUMMARY, CONCLUSIONS AND RECOMMENDATIONS

The overall findings of this study provide valuable insights to the understanding and the prediction of underwater noise from pile driving.

The CFD analysis results, when taken holistically are exciting because they suggest that geotechnical conditions affect underwater sound attenuation. However, these simulations did not take into account varying currents, viscosity, and turbulence. Future work could focus on refinement of these models to study how these nonlinear processes affect underwater sound TL. In addition, investigations for more sites in Florida could also be conducted in a similar manner to better understand how sound absorption from the bottom and surface influence TL. With several more analyses/runs like this, development of a correlation between geotechnical conditions and underwater TL coefficient may be attainable.

The calibration of Roger's model produced a slightly improved model for predicting TL which accommodates frequency variation and some geotechnical parameters. However, practical application of the calibrated model could be tricky since it sometimes overestimates TL and the geotechnical charts it is based upon are not entirely reliable. The limited accuracy can be attributed to the empirical nature of the calibration and the overabundance of parameters needed as inputs. Future work could attempt to remedy this by attempting a more robust empirical approach supported by strong theoretical derivations accounting for even more pertinent environment variables. This could lead to a model with improved accuracy that encompasses a larger subset of the required input field.

From a practical perspective therefore, the proposed new method from empirical data fitting results appears to be the go-to model for prediction of underwater noise TL from pile driving in Florida. The method is fairly simple to use and follows a structure similar to what is currently used. This method was produced by leveraging a large dataset from pile drives in Florida, and it is therefore is likely to be more accurate than the current guidelines because it is based upon calibration using local geotechnical conditions. However, like the current guidelines, implementation of the new method requires one to know sound-level at one location during pile driving. Future work can be targeted at eliminating this shortcoming, ideally by characterizing the SPL at the source as a function of already measured geotechnical information such as pile type, hammer type, hammer blow frequency, or data from pile driving analyzers. Further attention could also be placed at establishing exactly why A and $(L_s - B)$ appear to be correlated. The approach used to develop the proposed method could also be extended and applied to predicting the attenuation of different frequency bands by using each band's respective decay curve for each pile drive. This could be used in estimating the sound levels of different frequency components of the sound signals which are more impactful to marine life.

APPENDIX A
CFD PRESSURE CURVES

A.1 Bayway Site CFD Simulations SPL Curves

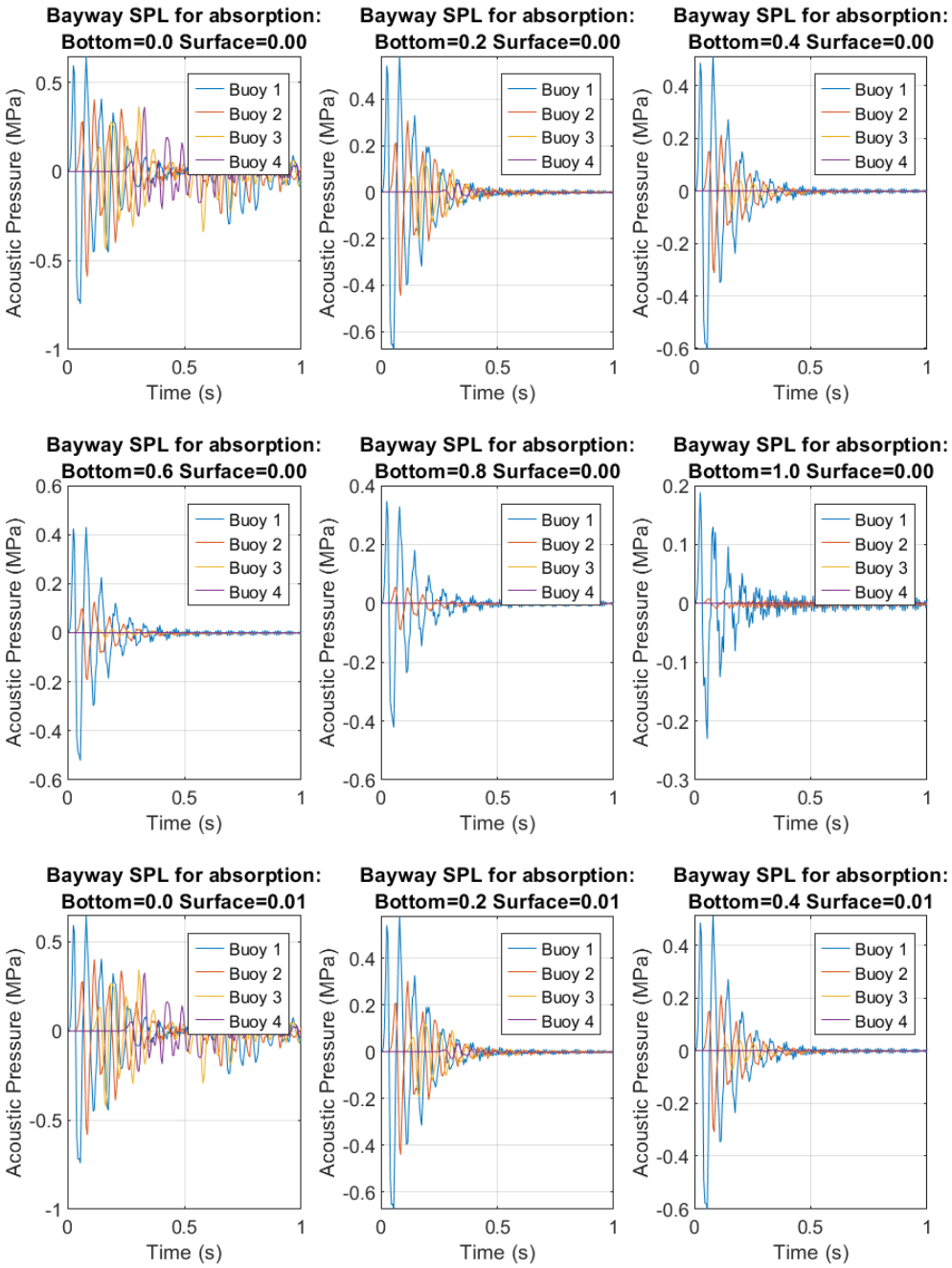

Figure A-1. Bayway SPL curves for bottom and surface combinations 1 - 9

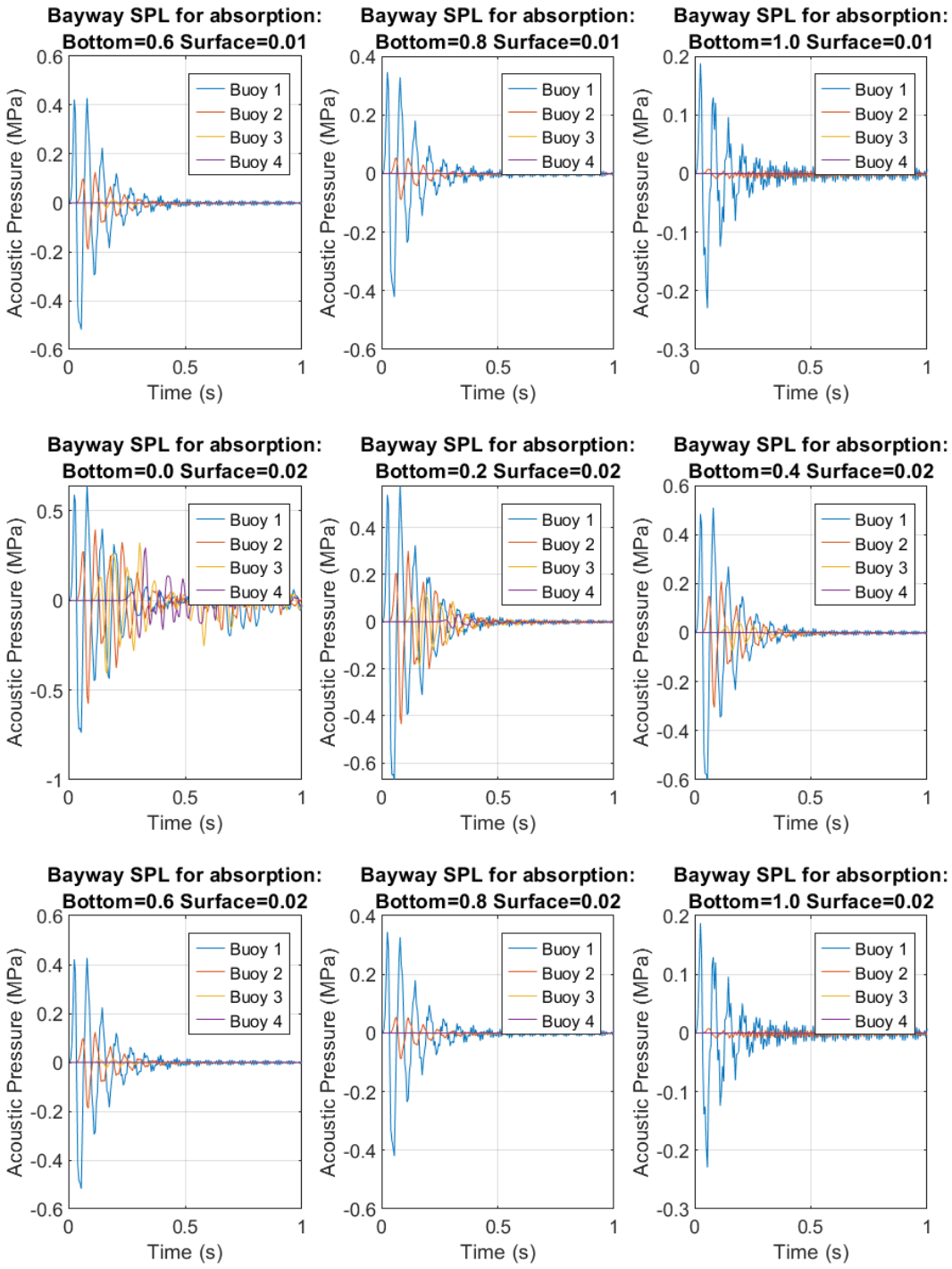

Figure A-2. Bayway SPL curves for bottom and surface combinations 10 - 18

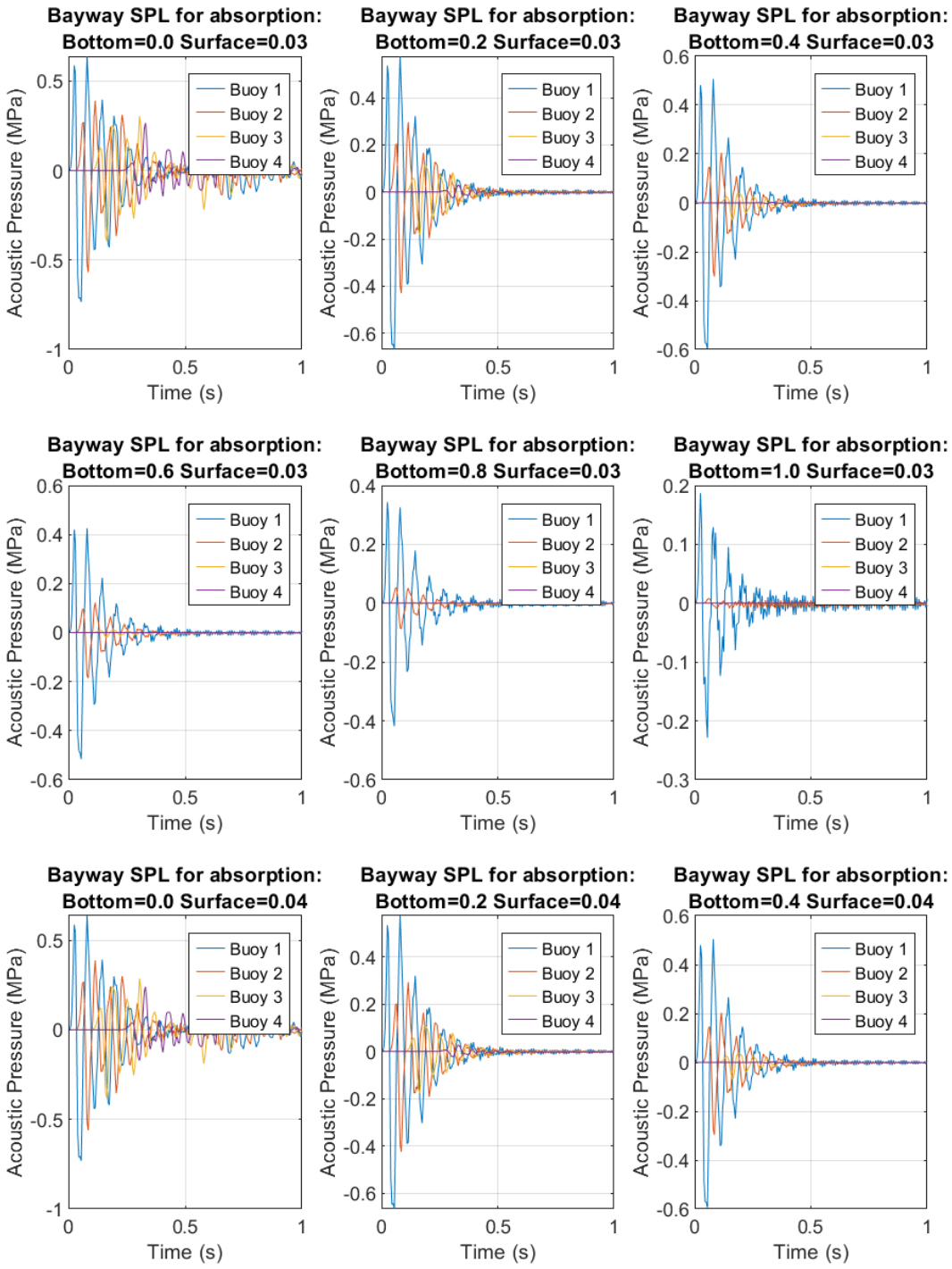

Figure A-3. Bayway SPL curves for bottom and surface combinations 19 - 27

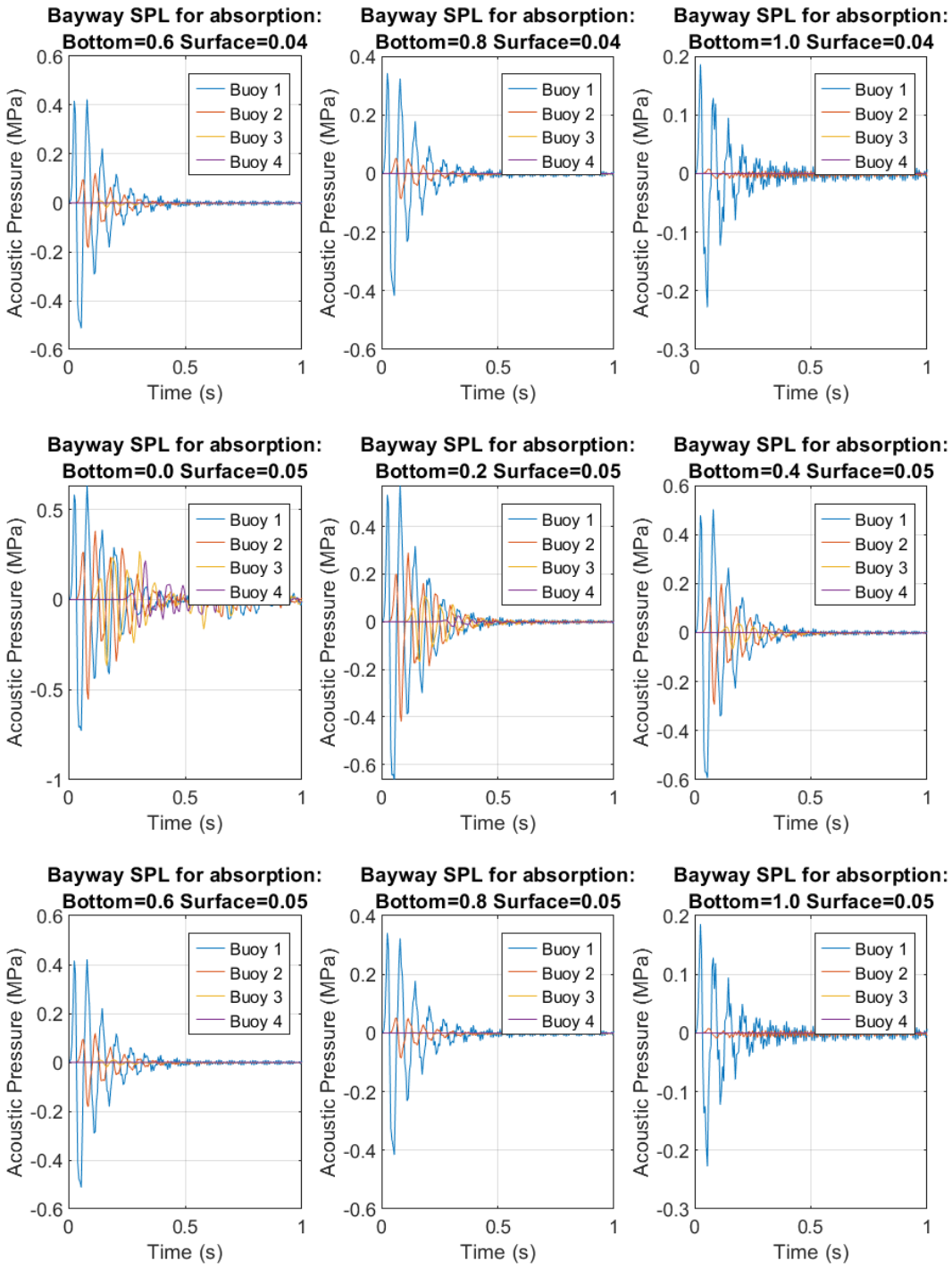

Figure A-4. Bayway SPL curves for bottom and surface combinations 28 - 36

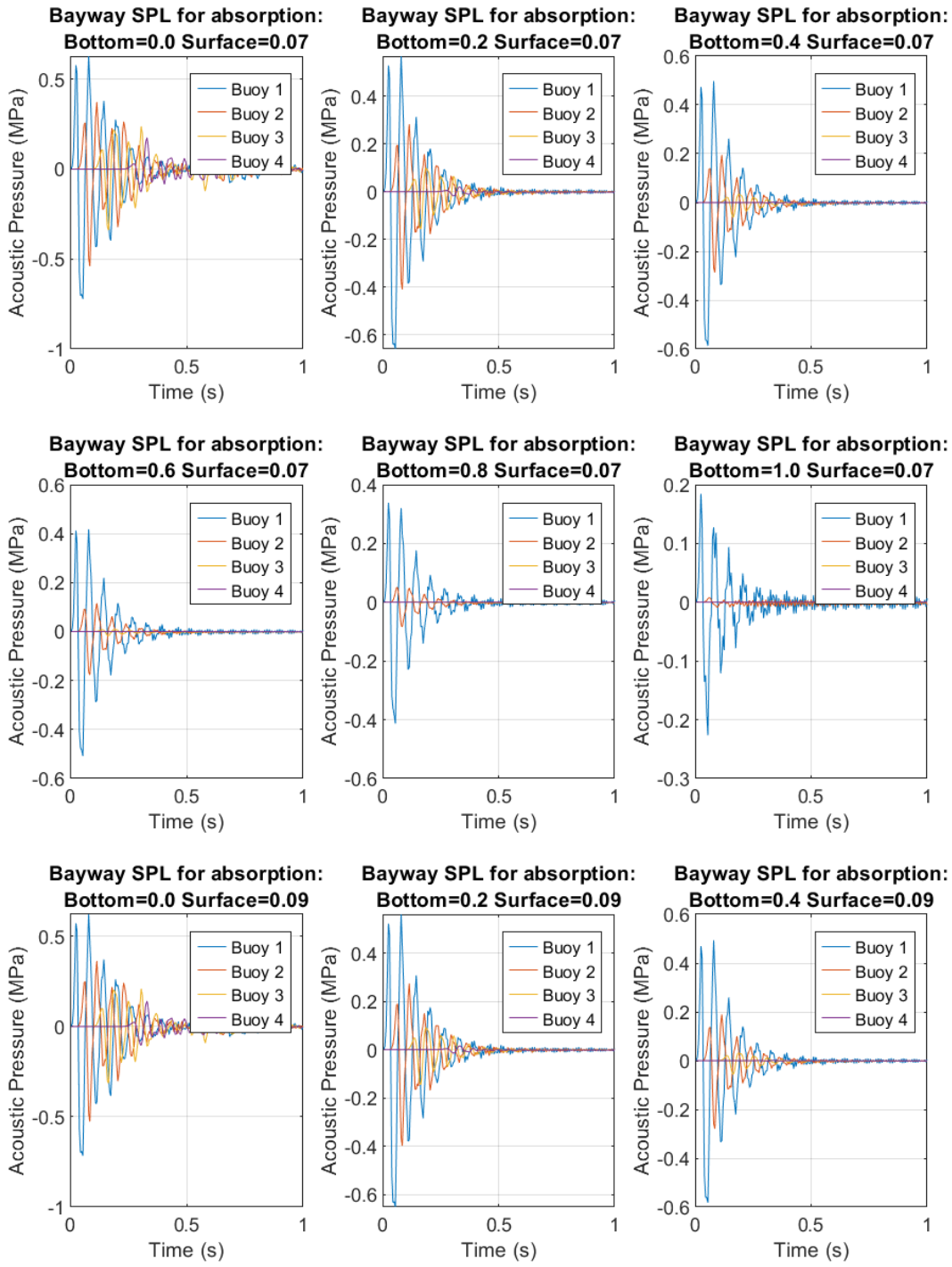

Figure A-5. Bayway SPL curves for bottom and surface combinations 37 - 45

A.2 Ribault Site CFD Simulations SPL Curves

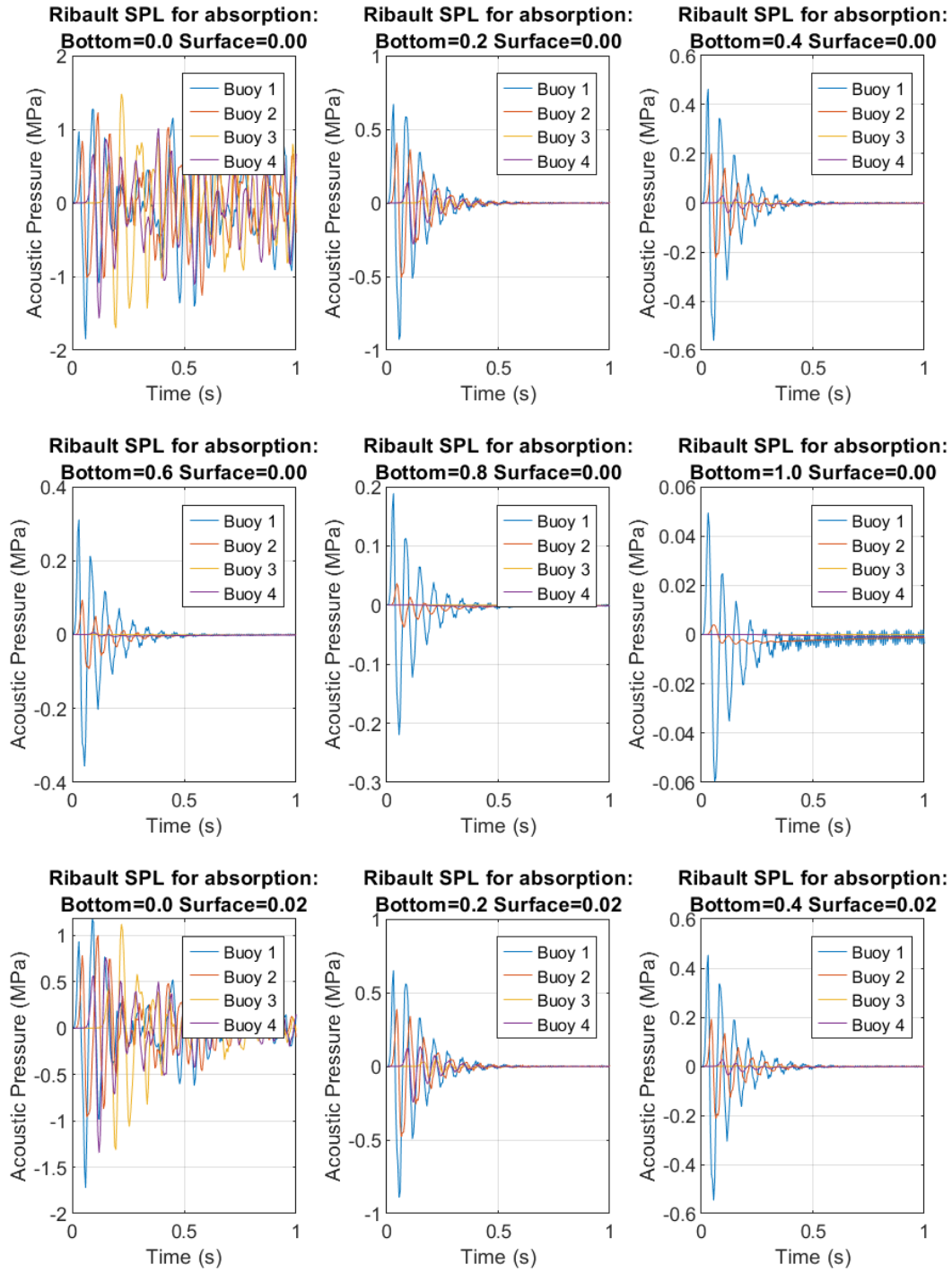

Figure A-6. Ribault SPL curves for bottom and surface combinations 1 - 9

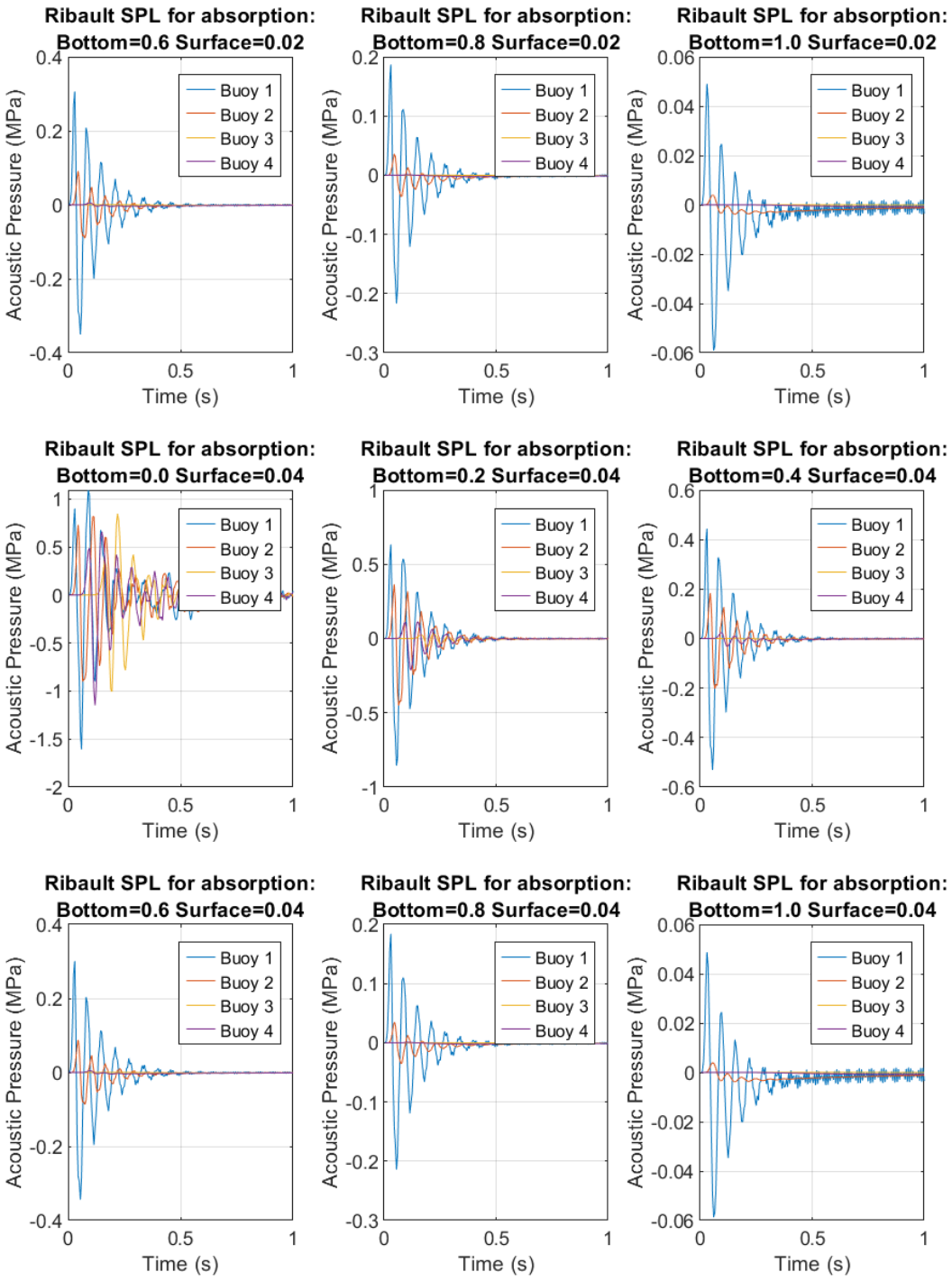

Figure A-7. Ribault SPL curves for bottom and surface combinations 10 - 18

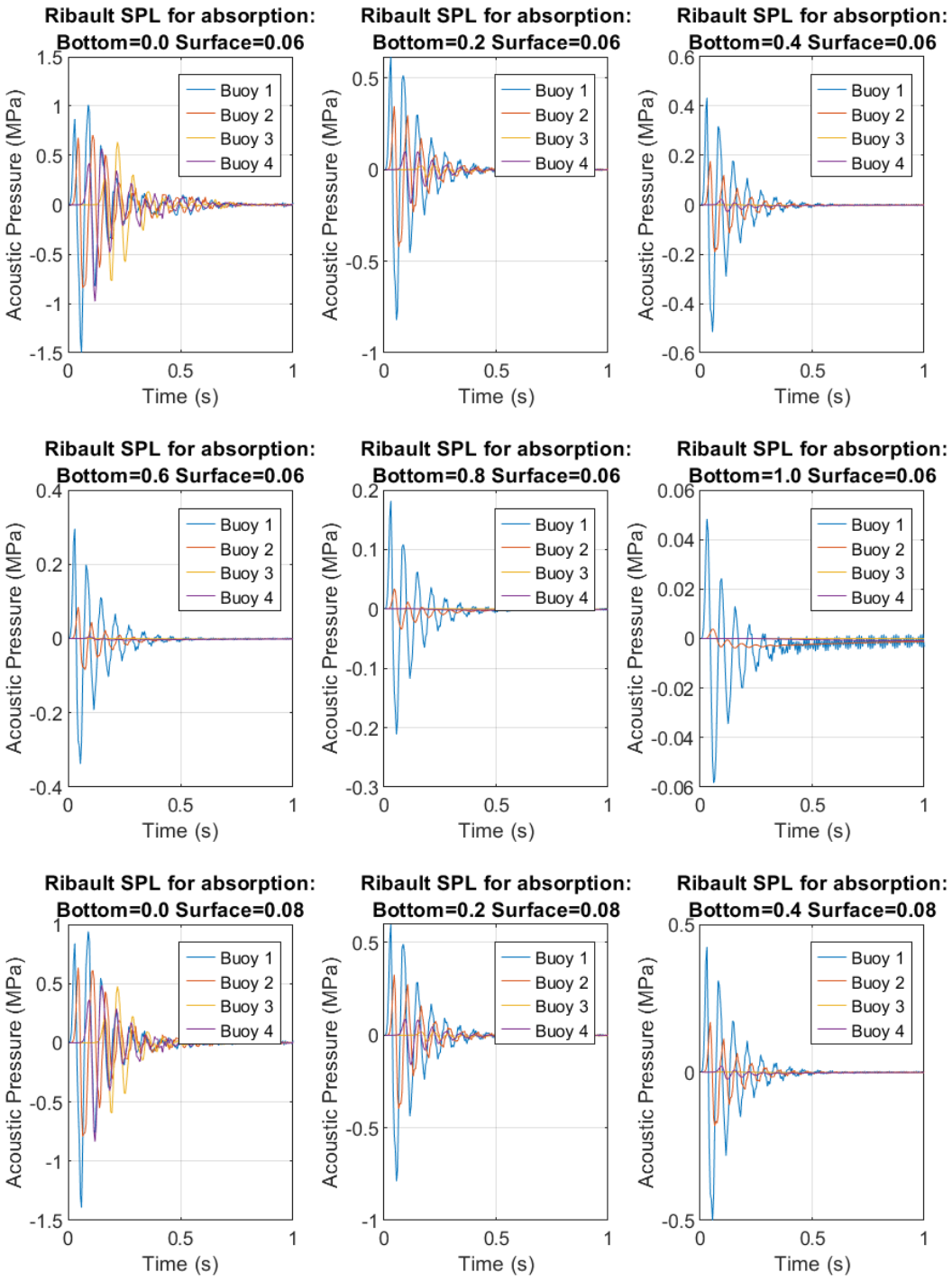

Figure A-8. Ribault SPL curves for bottom and surface combinations 19 - 27

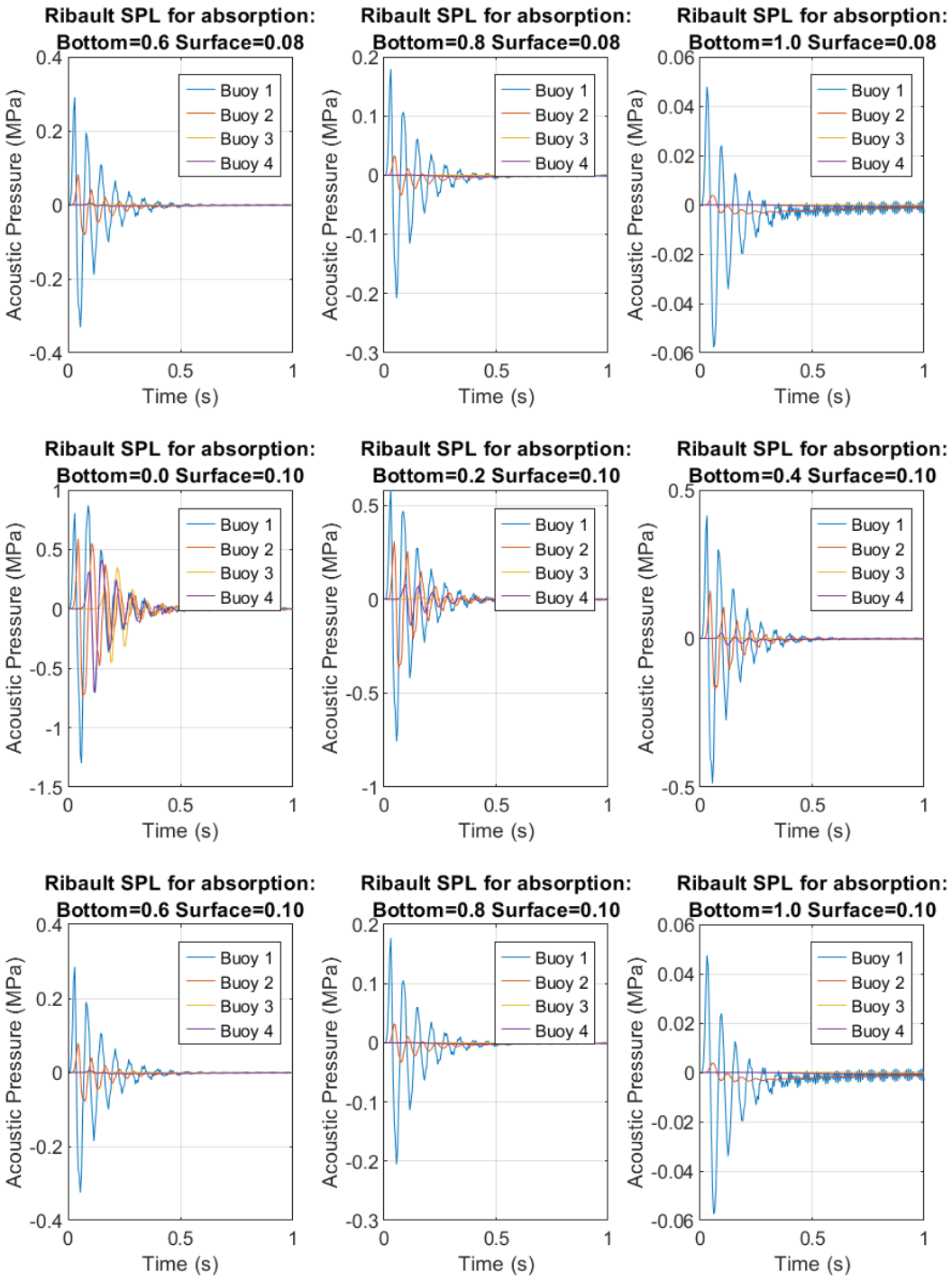

Figure A-9. Ribault SPL curves for bottom and surface combinations 28 - 36

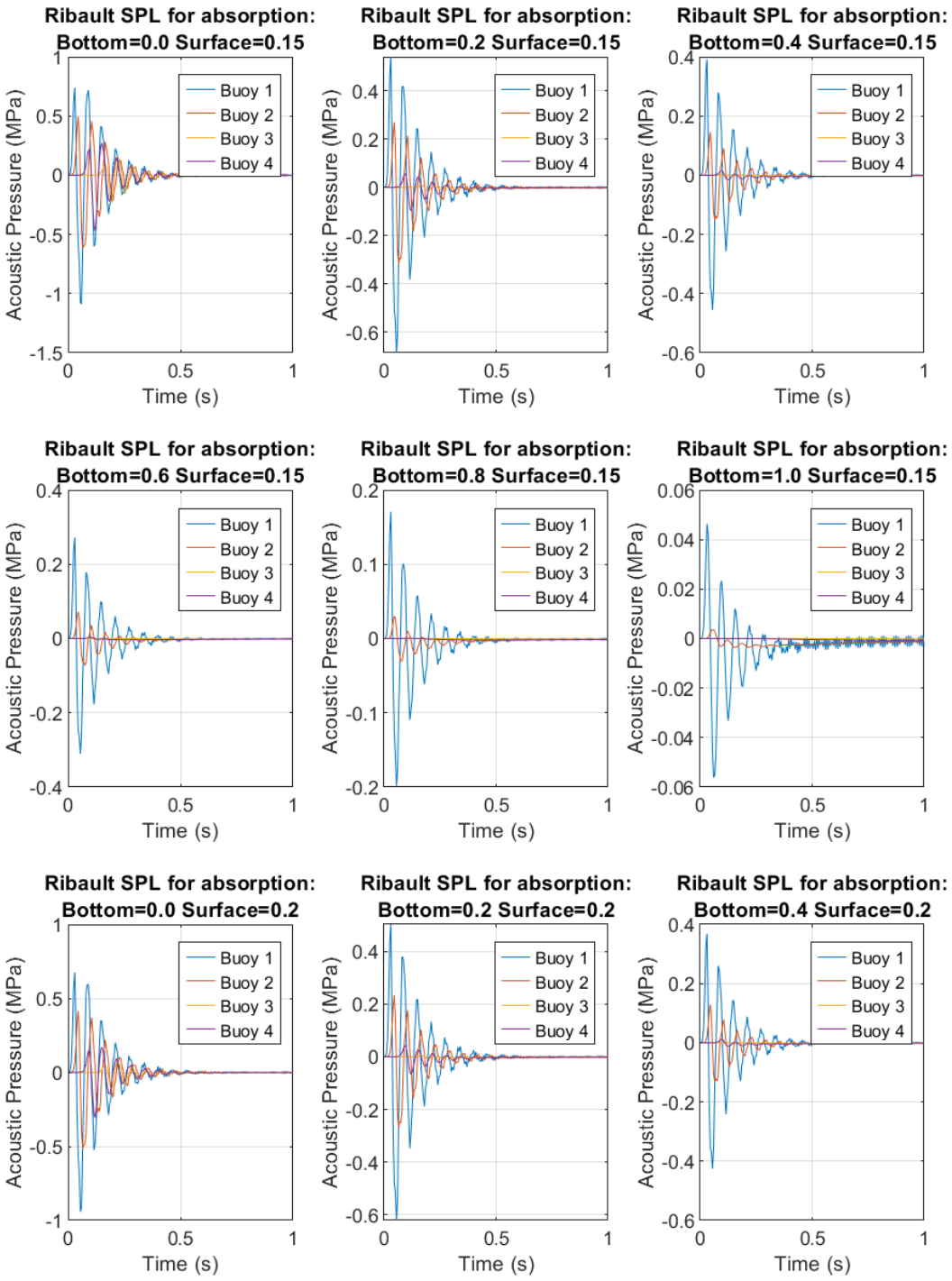

Figure A-10. Ribault SPL curves for bottom and surface combinations 37 - 45

A.3 John Sims Parkway Bridge Site CFD Simulations SPL Curves

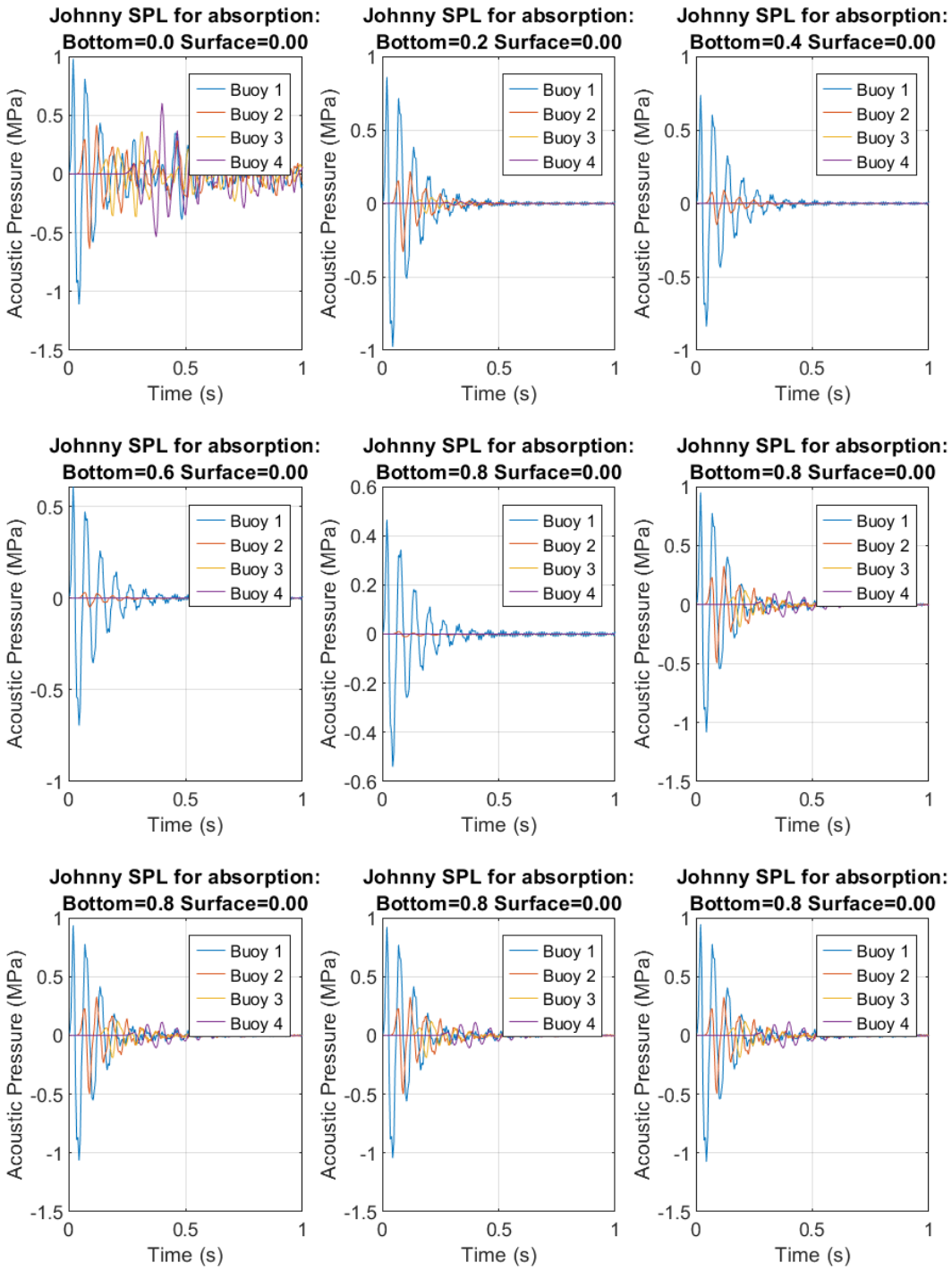

Figure A-11. John Sims Parkway SPL curves for bottom and surface combinations 1 - 9

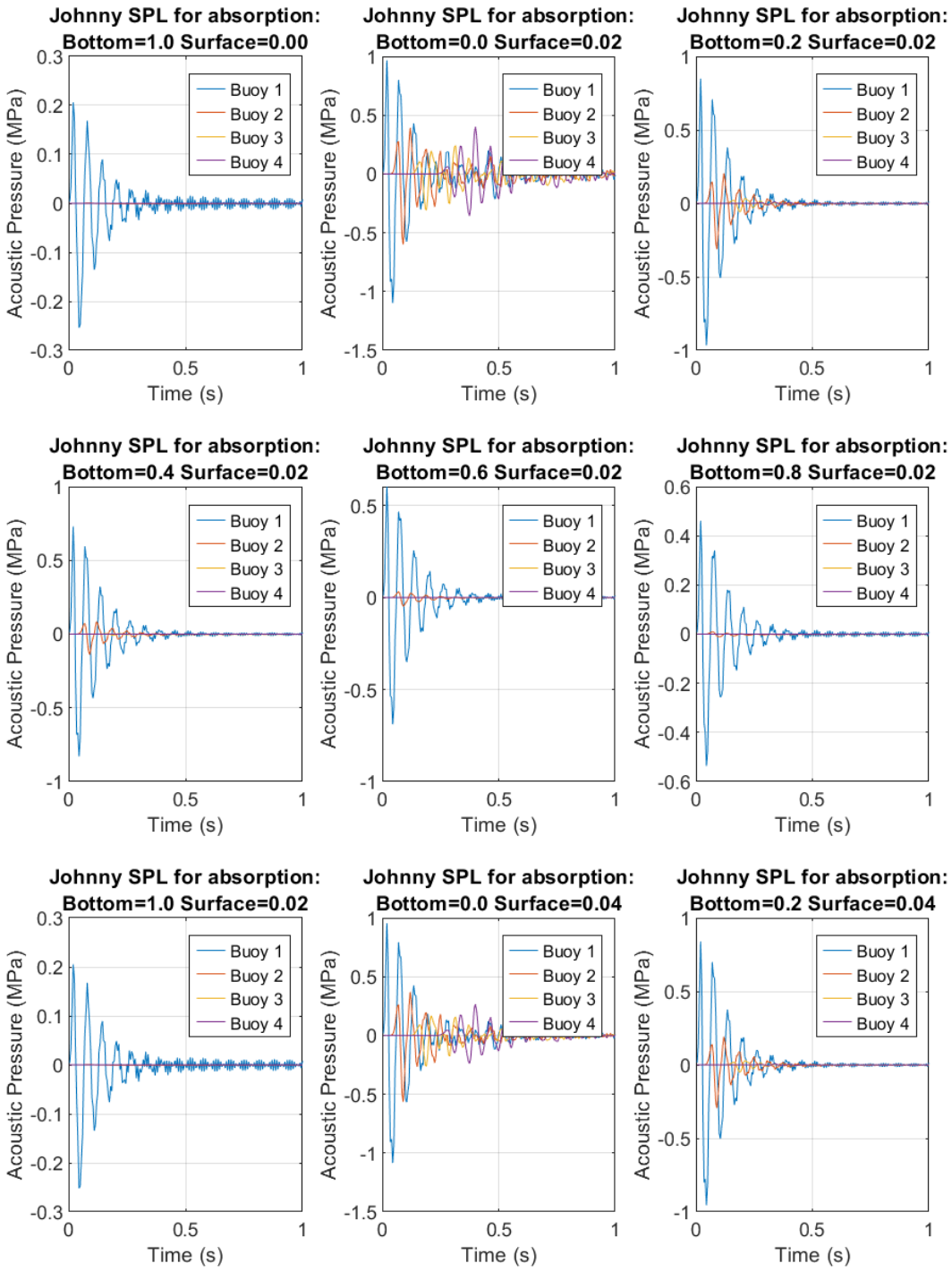

Figure A-12. John Sims Parkway SPL curves for bottom and surface combinations 10-18

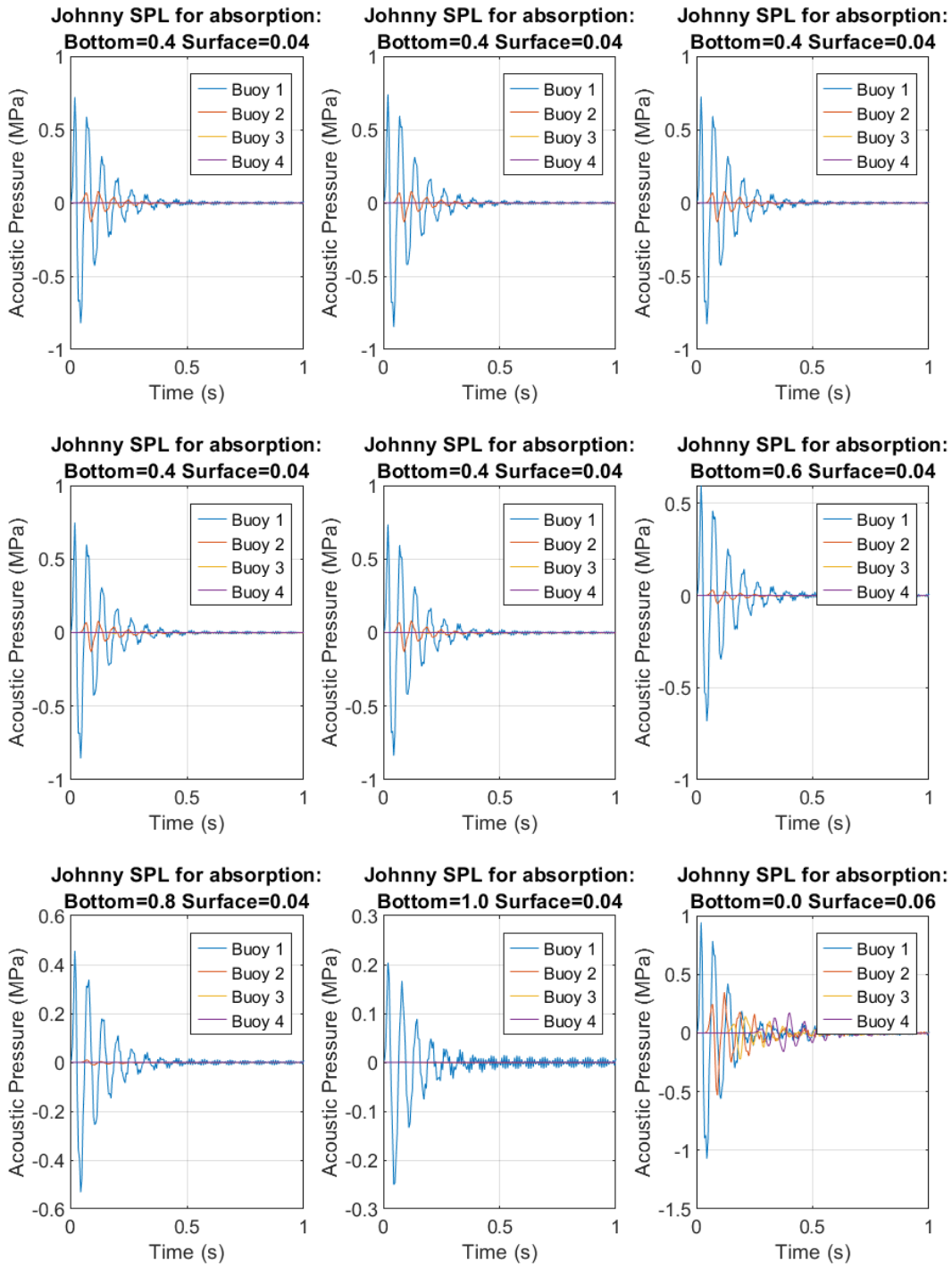

Figure A-13. John Sims Parkway SPL curves for bottom and surface combinations 19 - 27

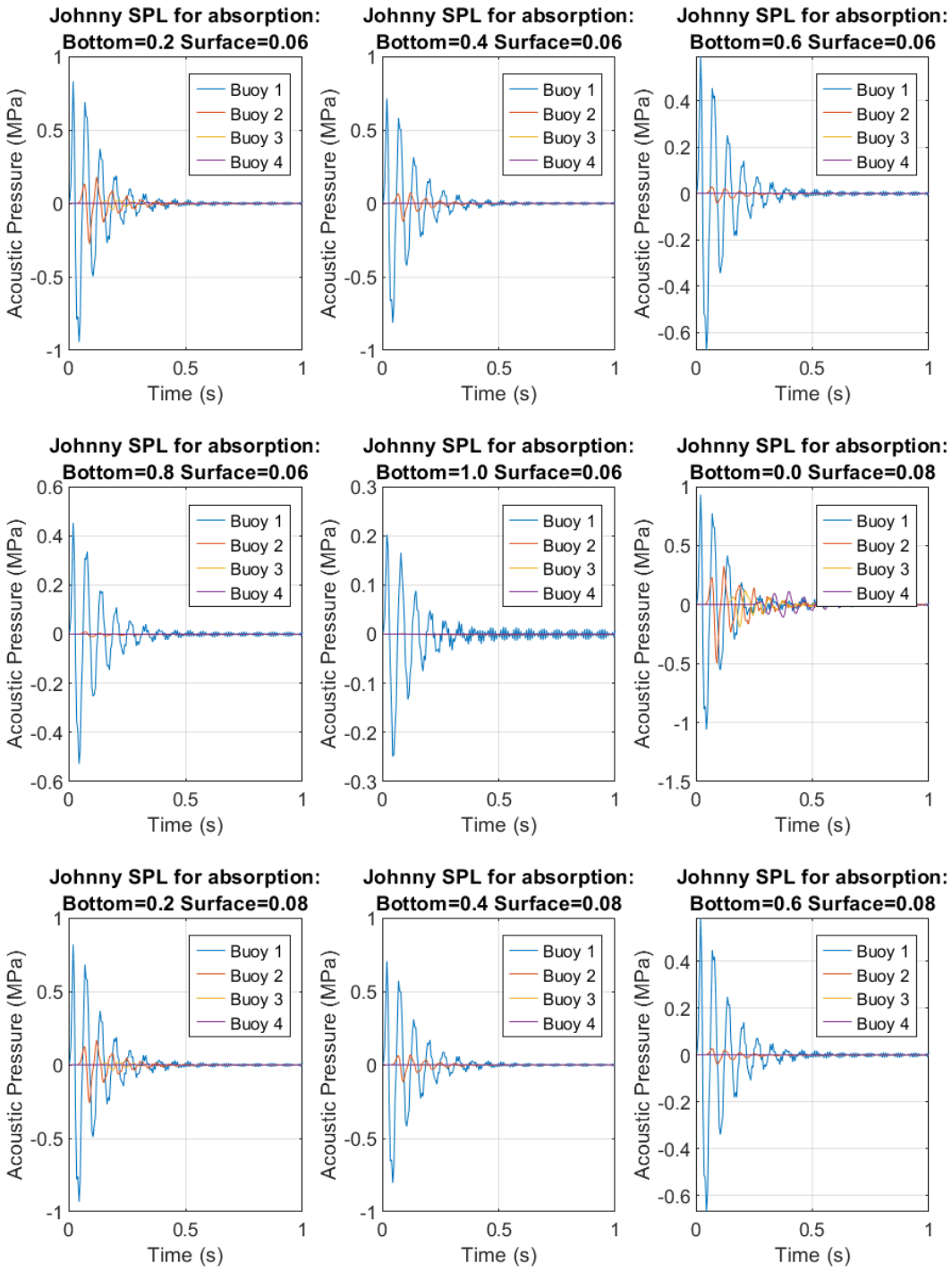

Figure A-14. John Sims Parkway SPL curves for bottom and surface combinations 28 - 36

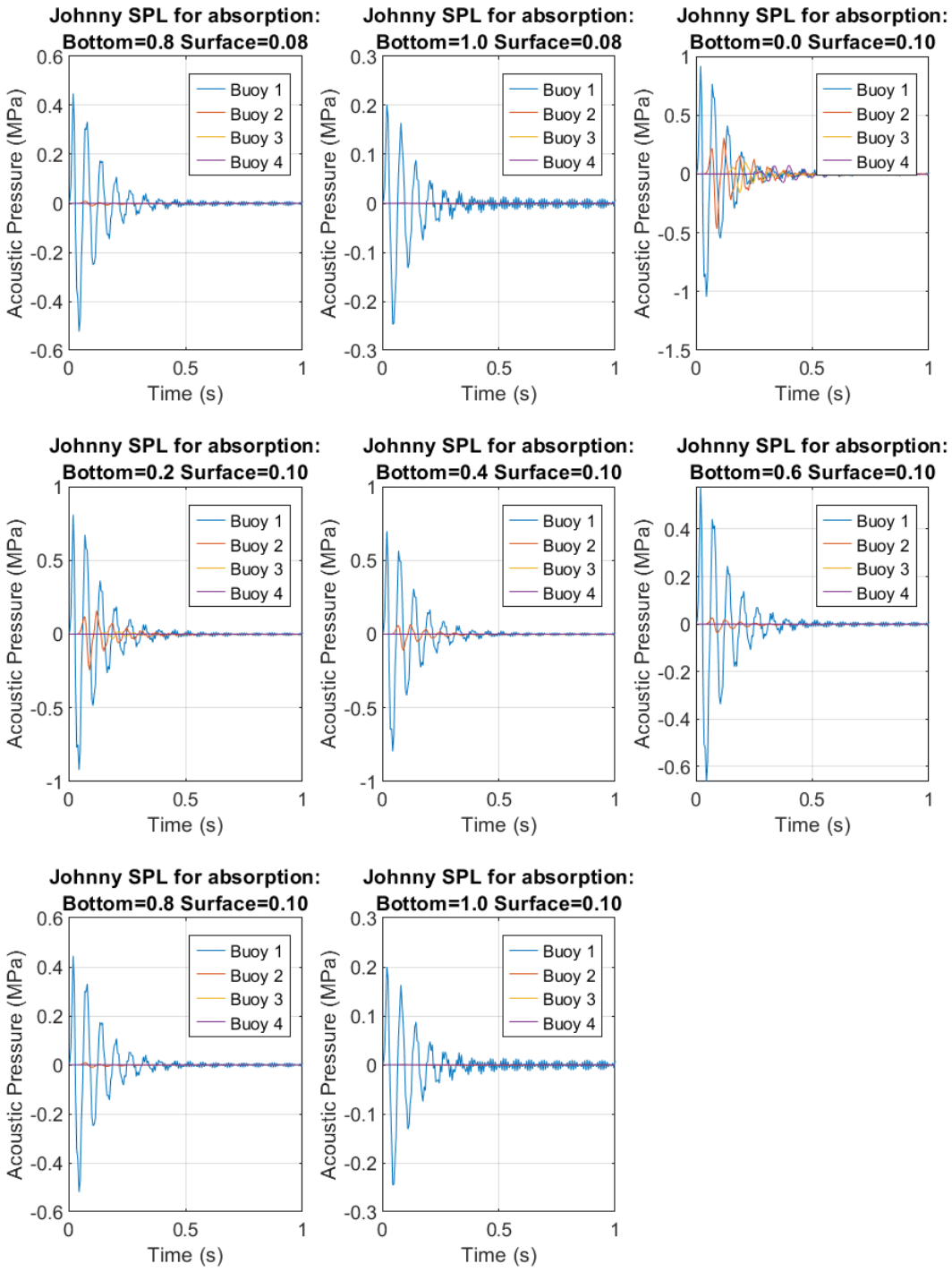

Figure A-15. Bayway SPL curves for bottom and surface combinations 37 - 44

APPENDIX B
CFD DECAY CURVES

B.1 Bayway Site CFD Simulations Curves

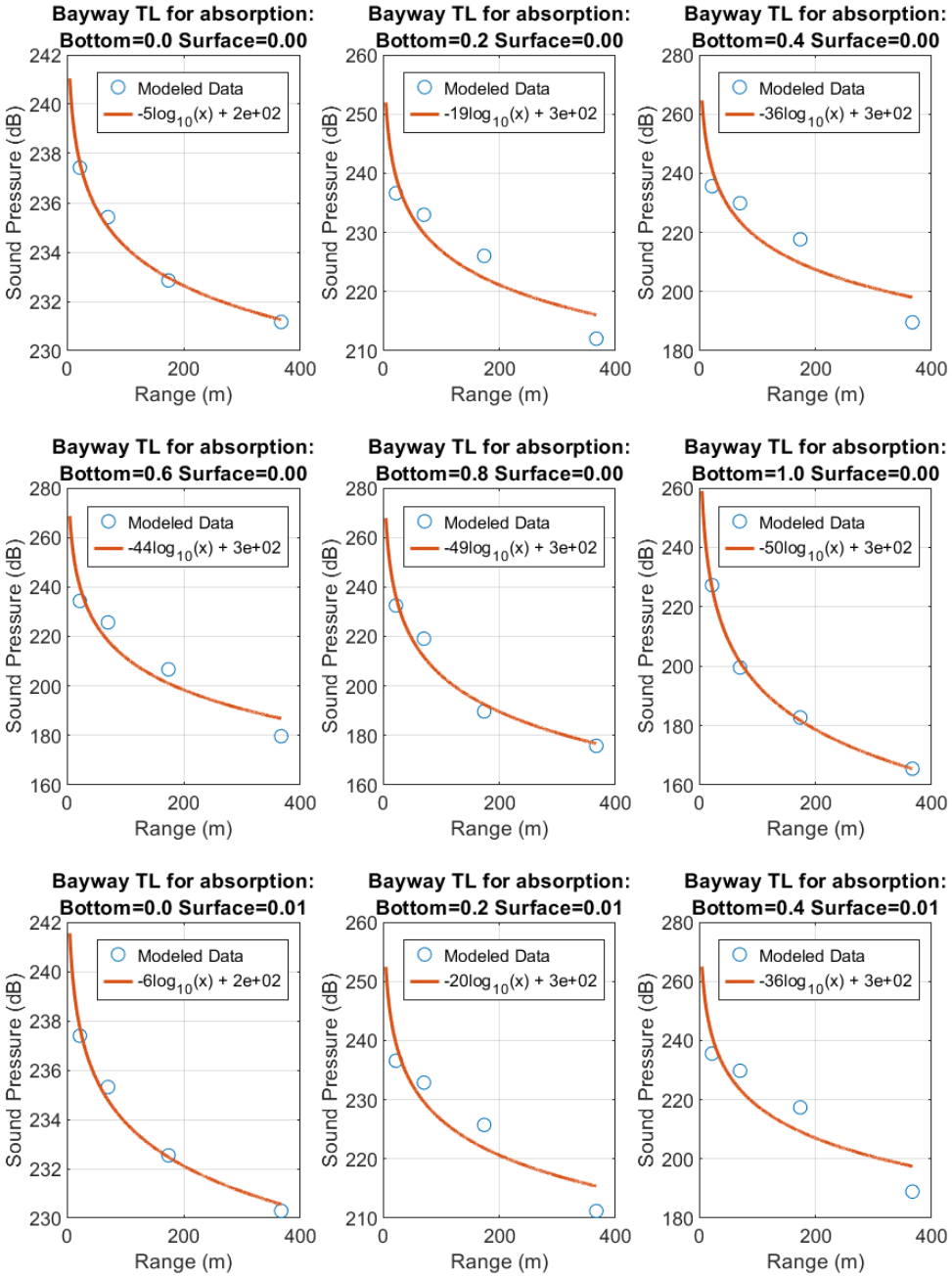

Figure B-1. Bayway TL curves for bottom and surface combinations 1 - 9

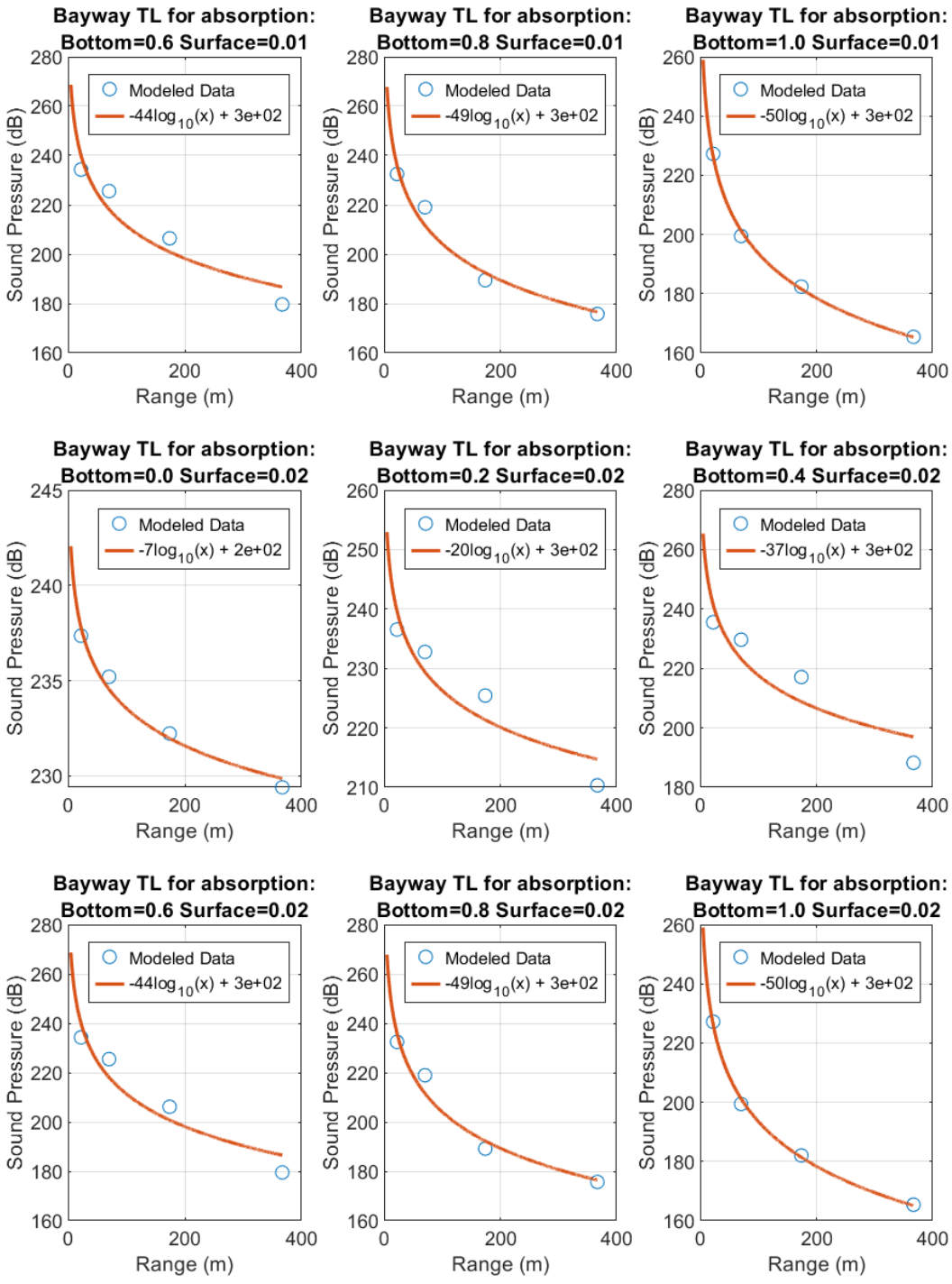

Figure B-2. Bayway TL curves for bottom and surface combinations 10 - 18

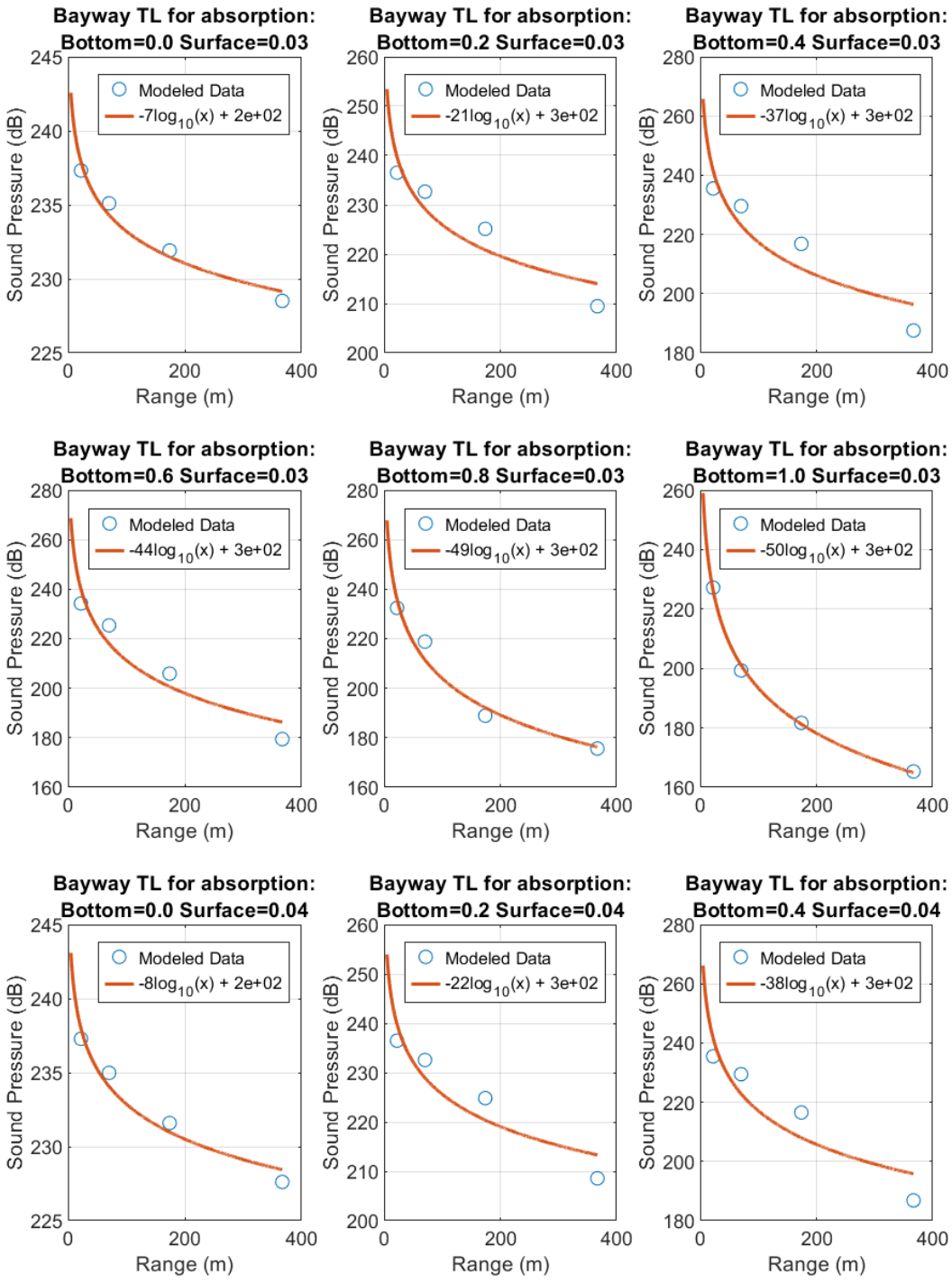

Figure B-3. Bayway TL curves for bottom and surface combinations 19 - 27

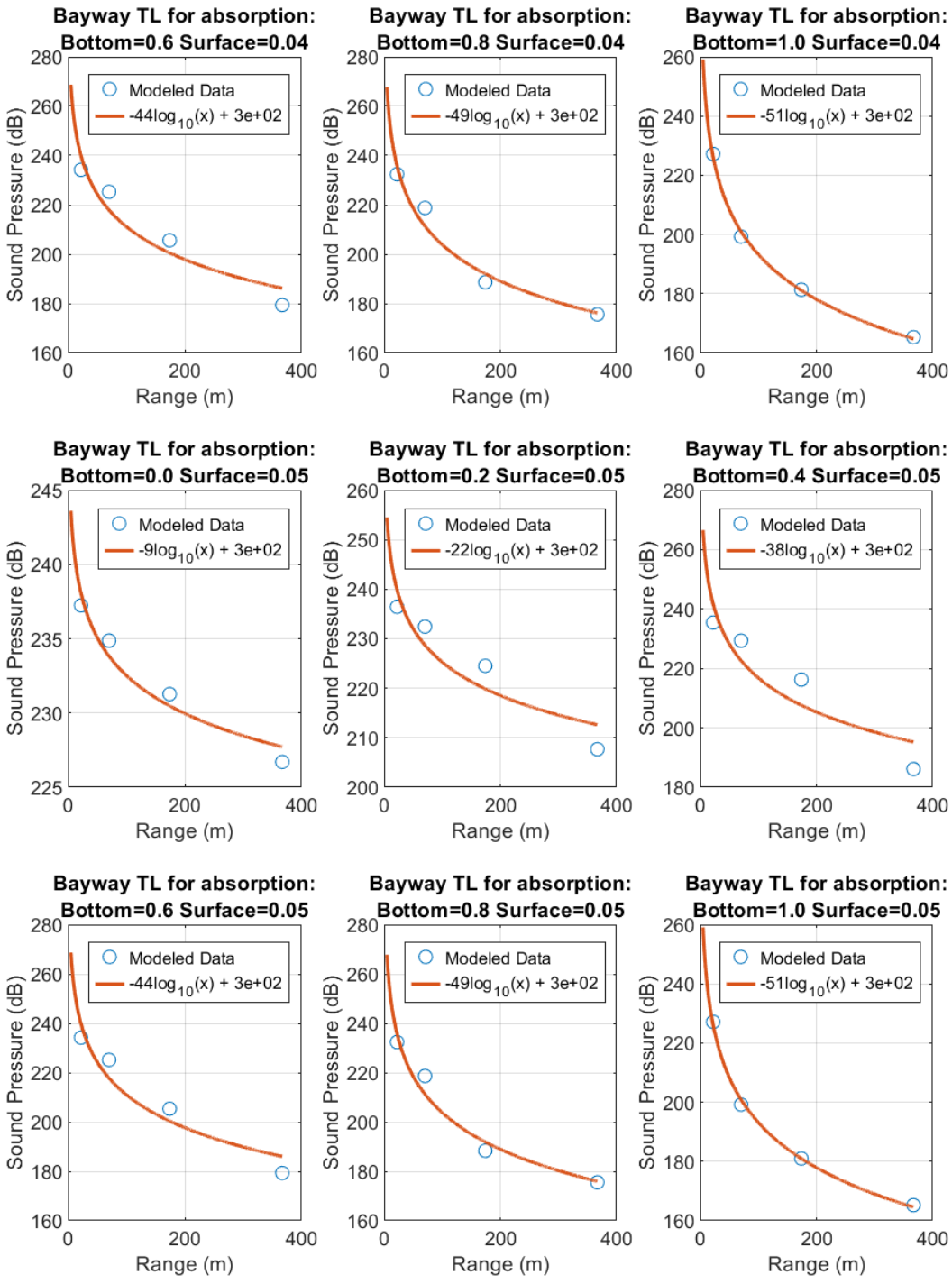

Figure B-4. Bayway TL curves for bottom and surface combinations 28 - 36

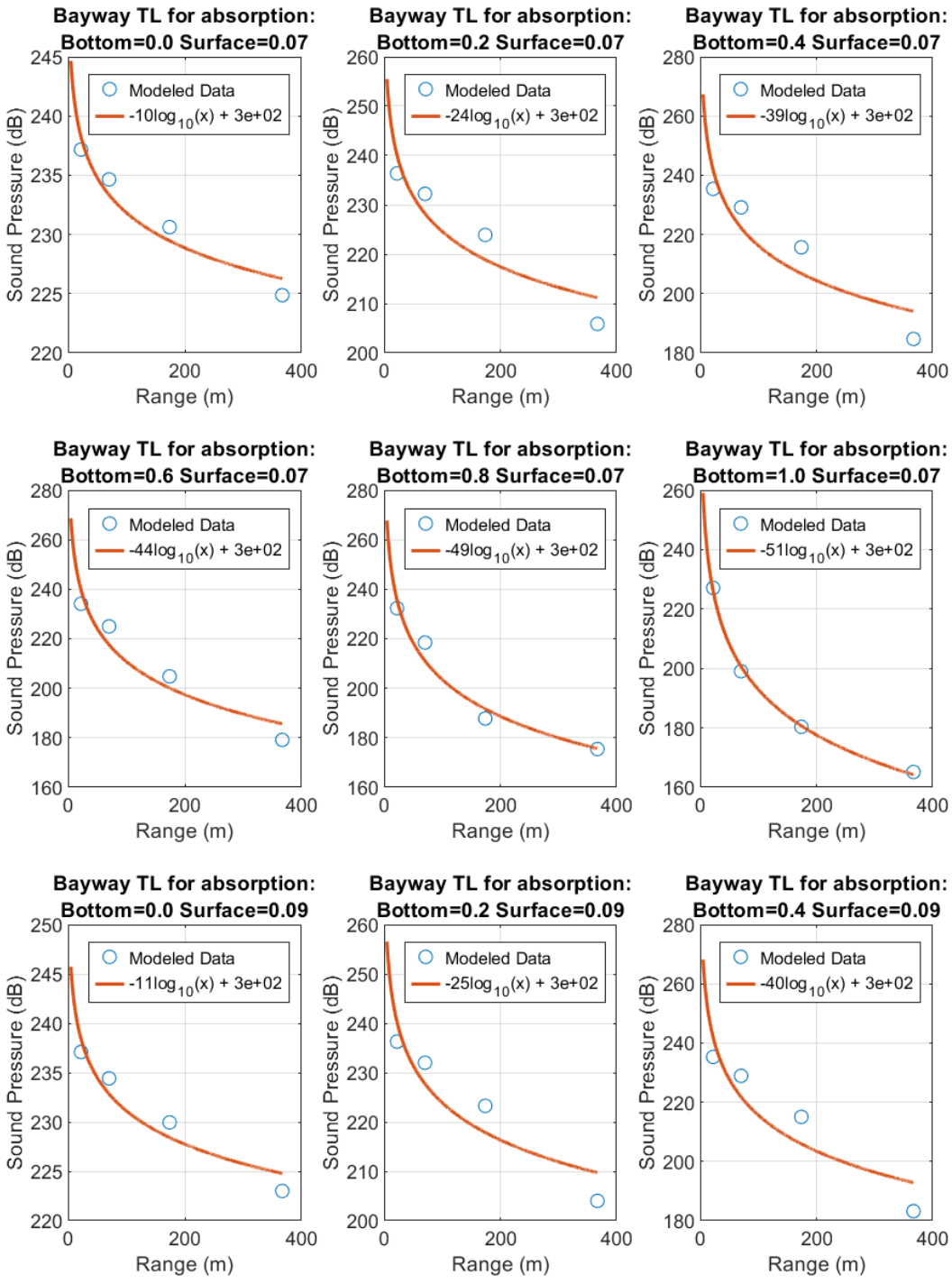

Figure B-5. Bayway TL curves for bottom and surface combinations 37 - 45

B.2 Ribault Site CFD Simulations TL Curves

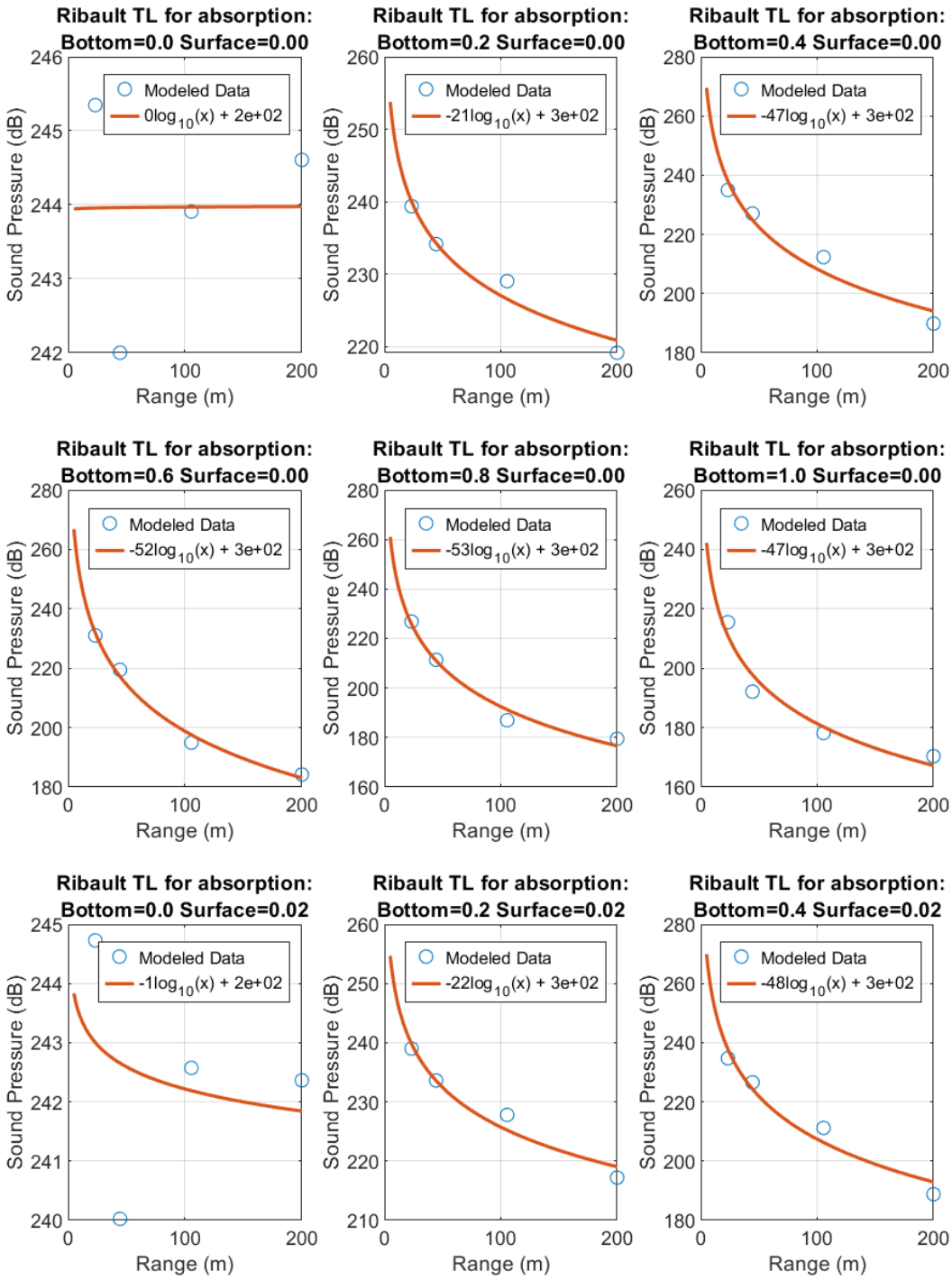

Figure B-6. Ribault TL curves for bottom and surface combinations 1 - 9

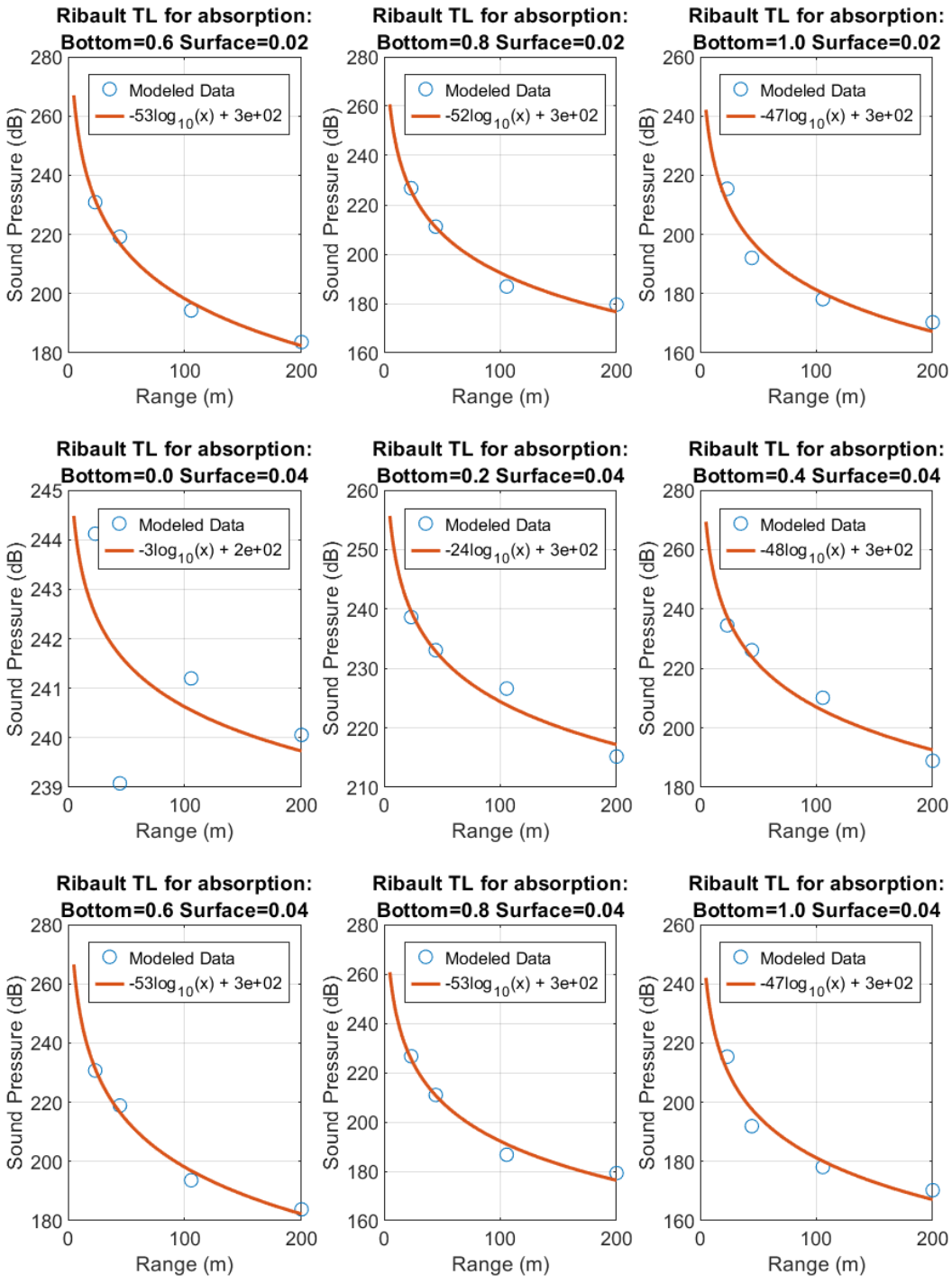

Figure B-7. Ribault TL curves for bottom and surface combinations 10 - 18

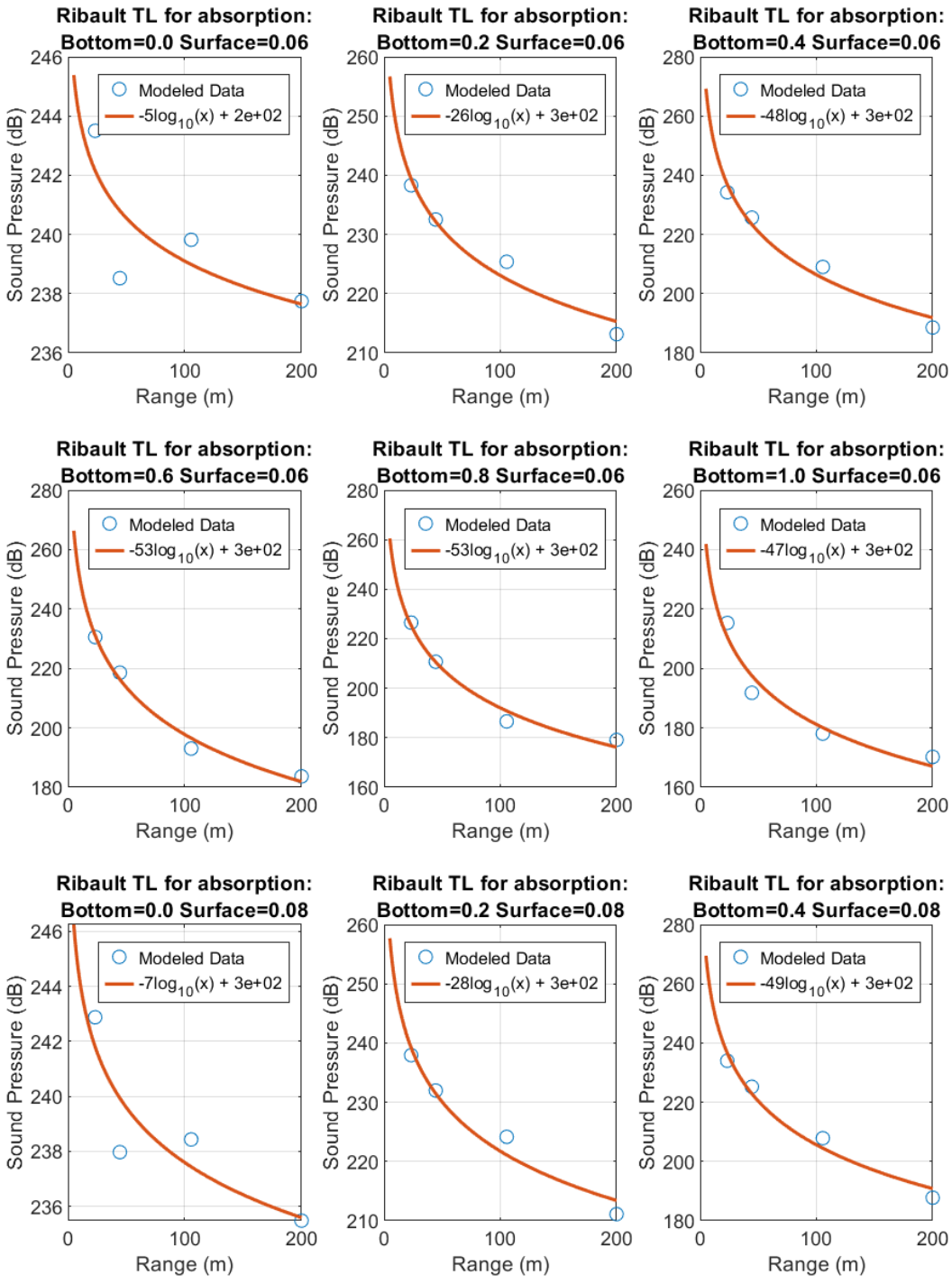

Figure B-8. Ribault TL curves for bottom and surface combinations 19 - 27

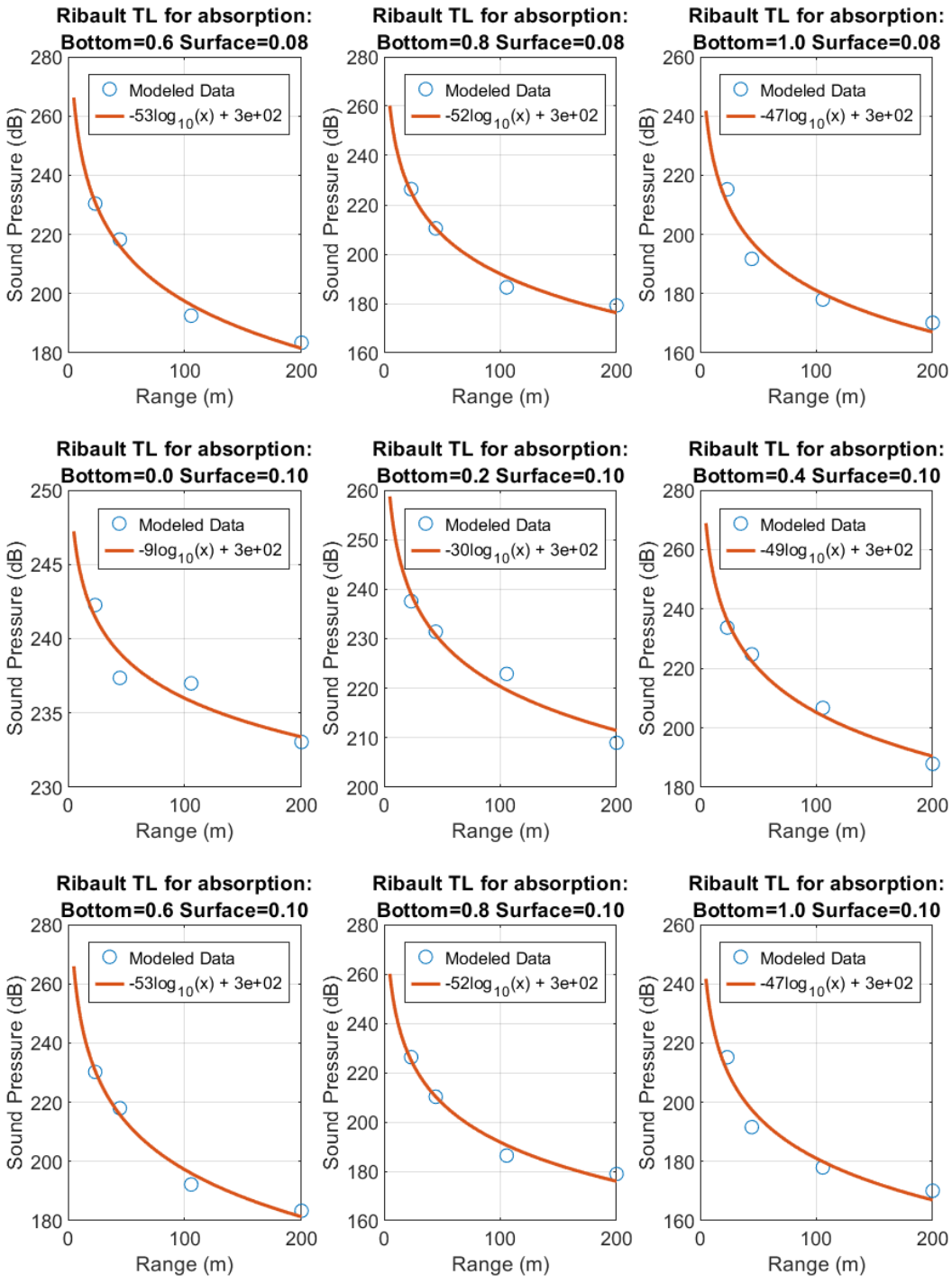

Figure B-9. Ribault TL curves for bottom and surface combinations 28 - 36

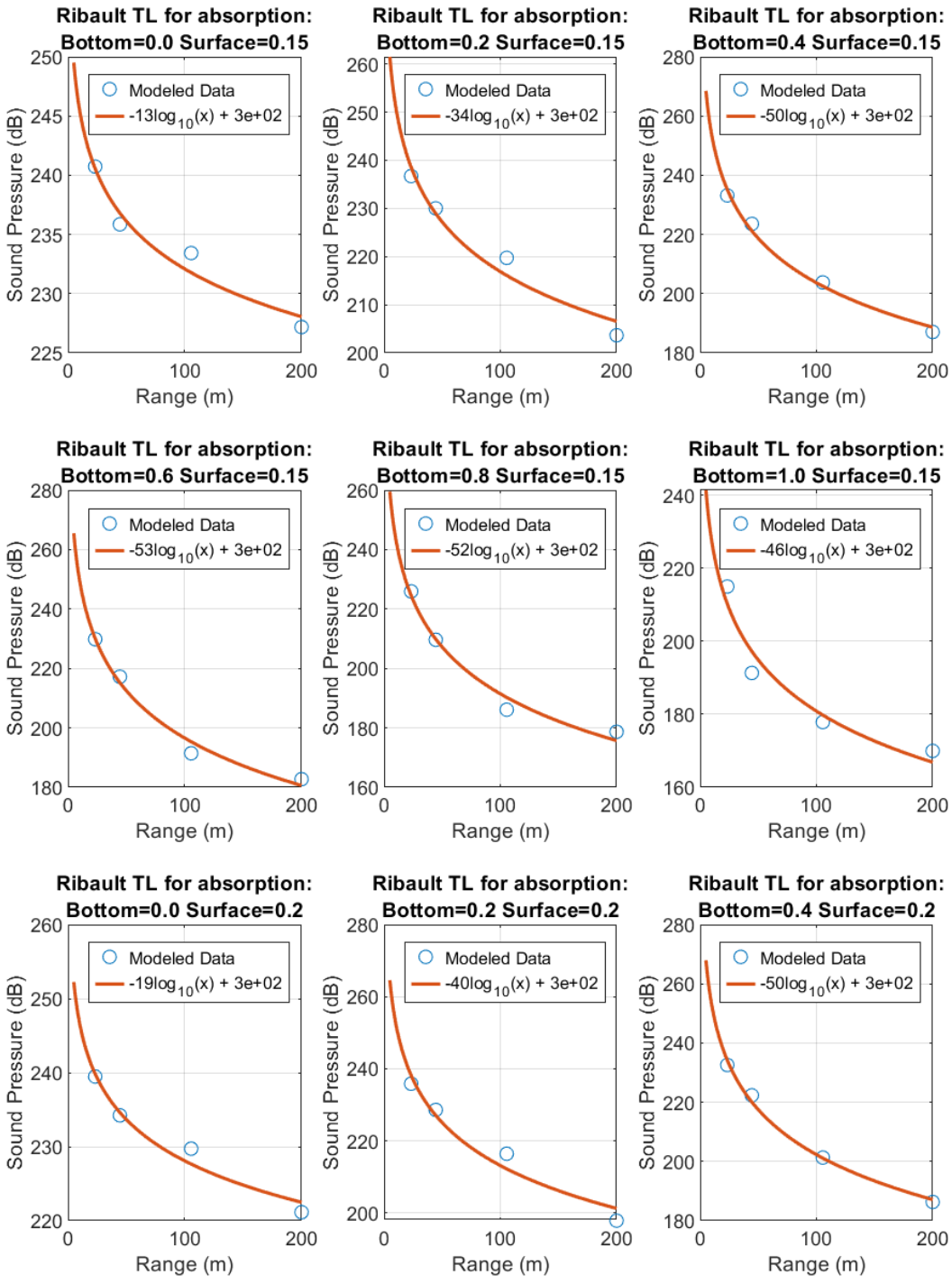

Figure B-10. Ribault TL curves for bottom and surface combinations 37 - 45

B.3 John Sims Parkway Bridge Site CFD Simulations TL Curves

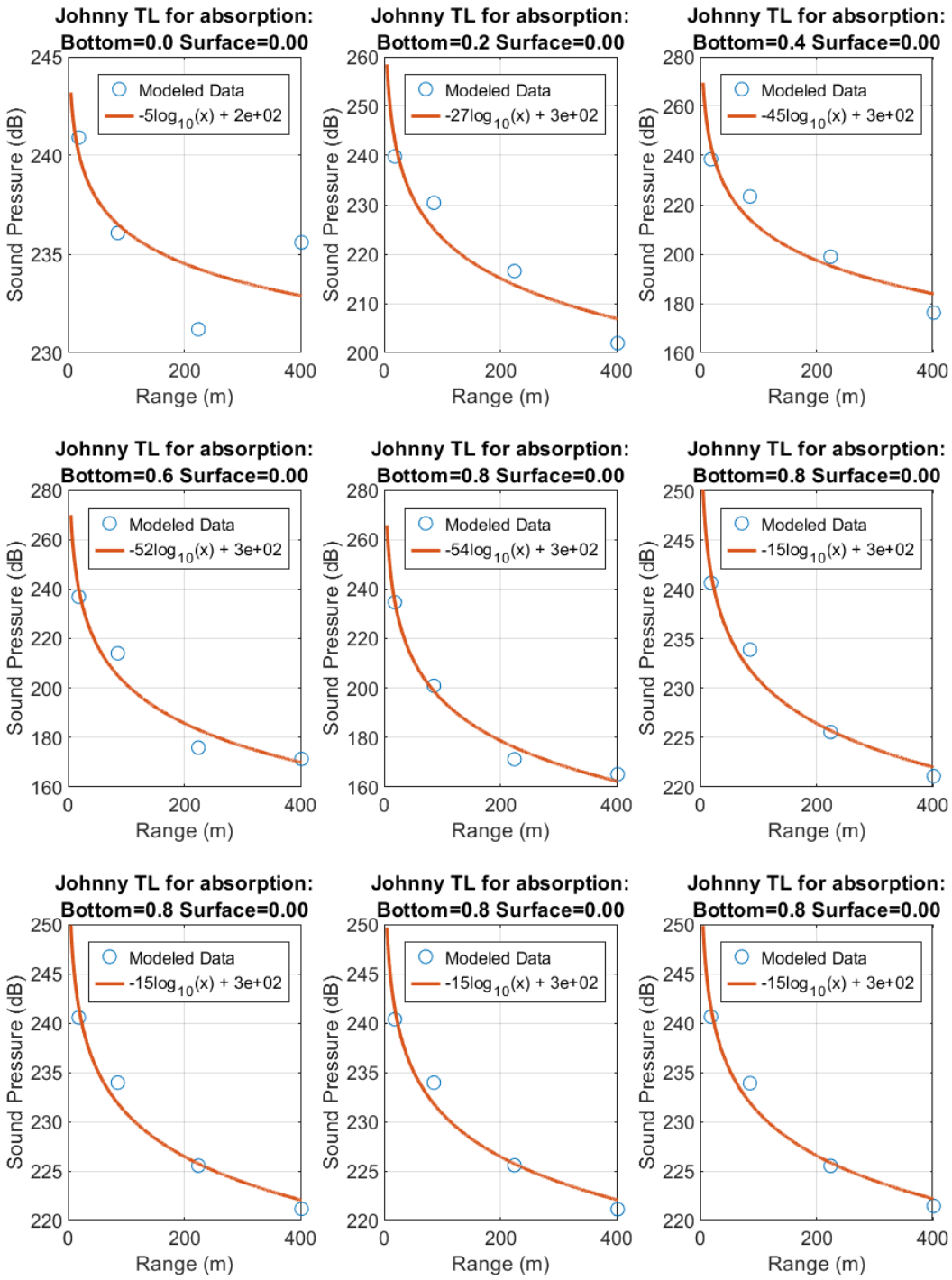

Figure B-11. John Sims Parkway TL curves for bottom and surface combinations 1 - 9

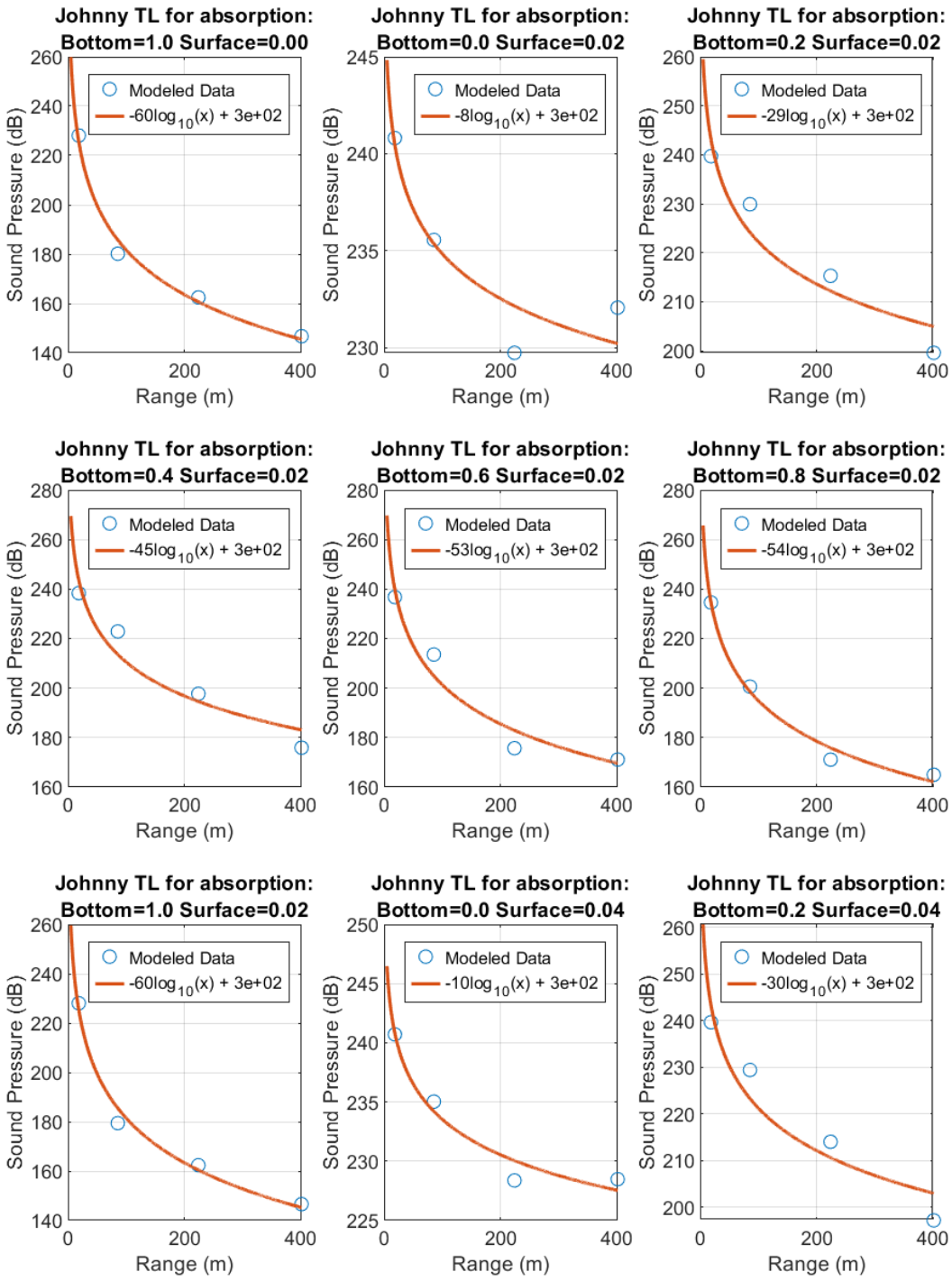

Figure B-12. John Sims Parkway TL curves for bottom and surface combinations 10 - 18

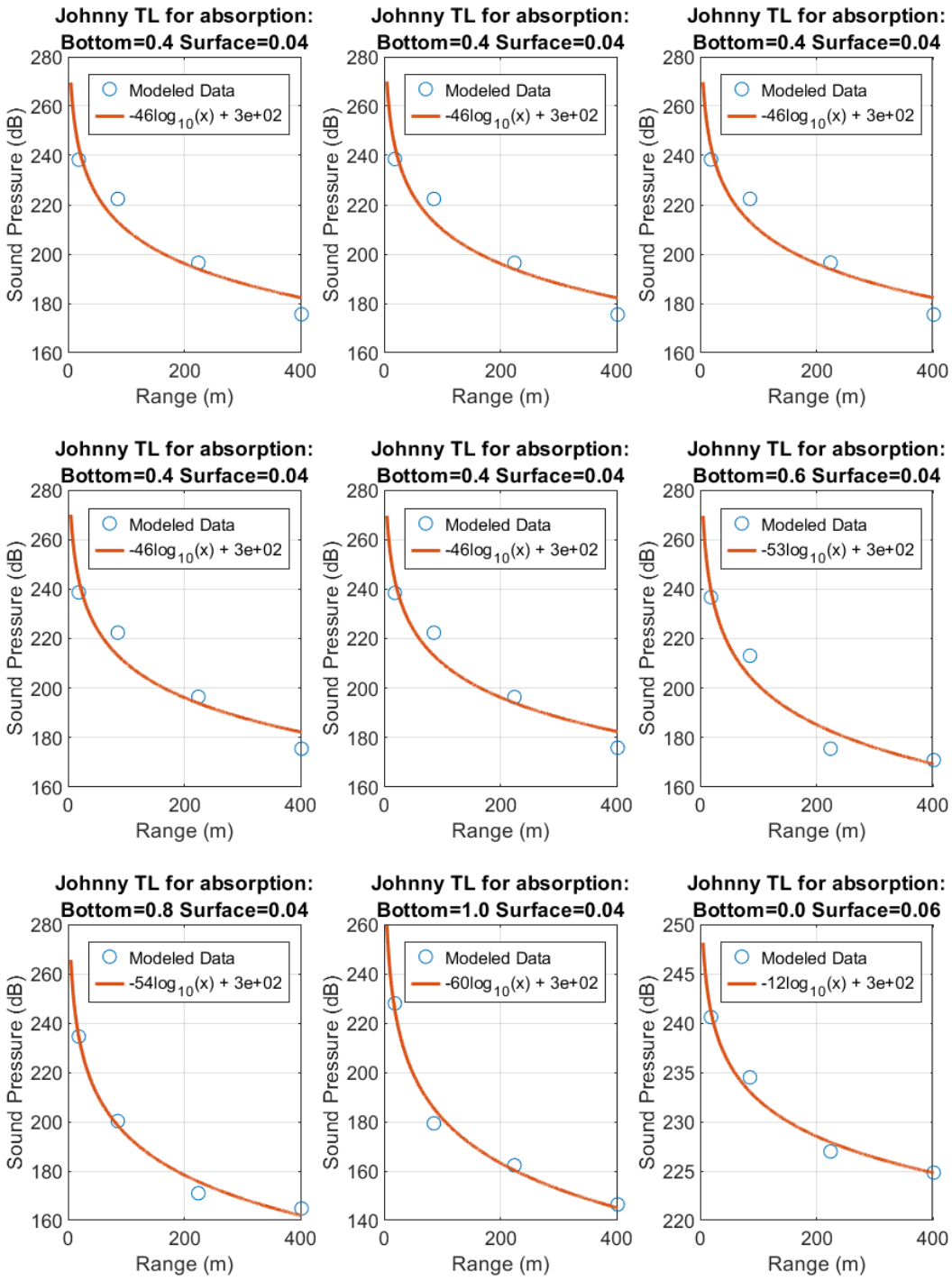

Figure B-13. John Sims Parkway TL curves for bottom and surface combinations 19 - 27

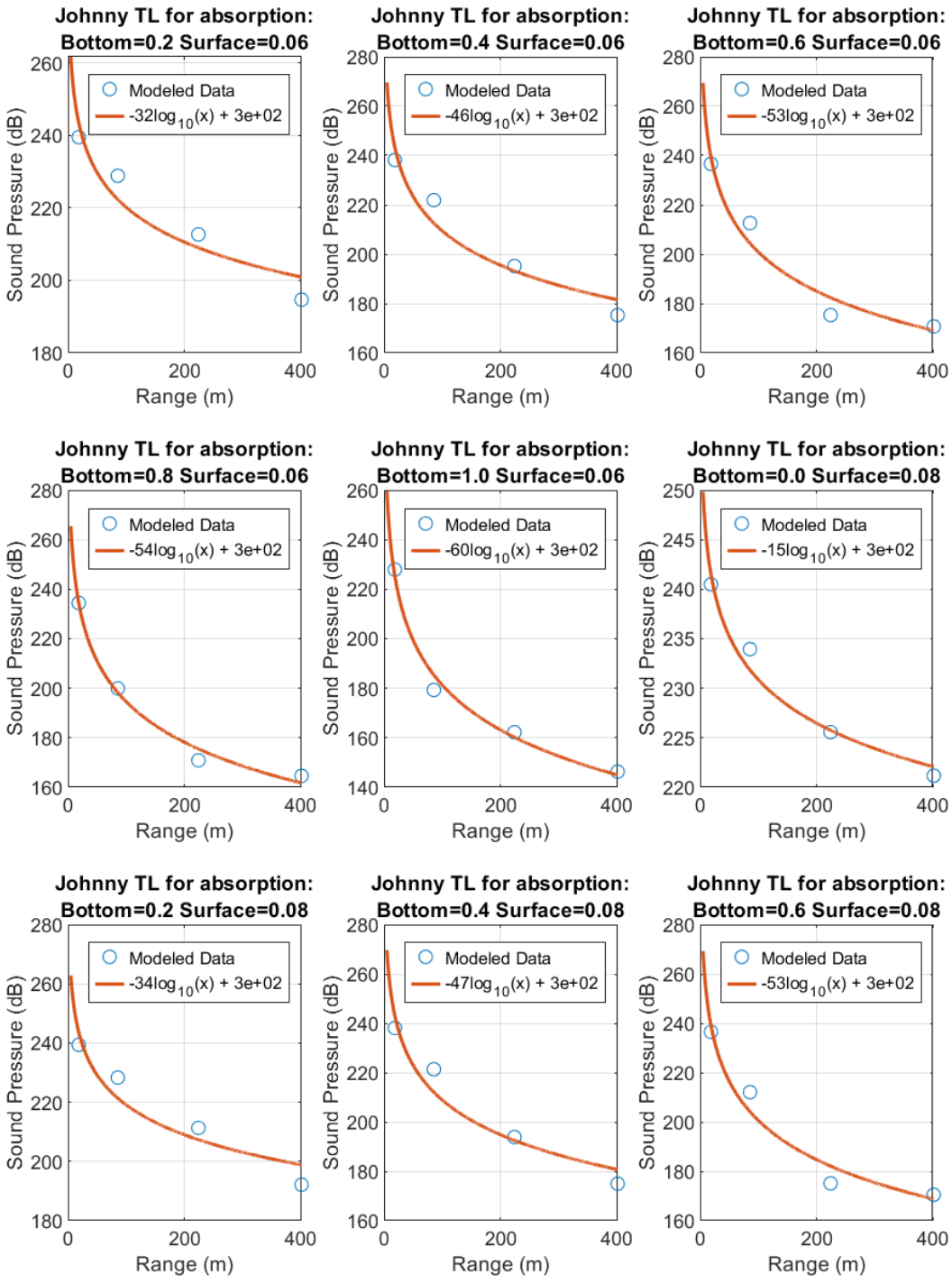

Figure B-14. John Sims Parkway TL curves for bottom and surface combinations 28 - 36

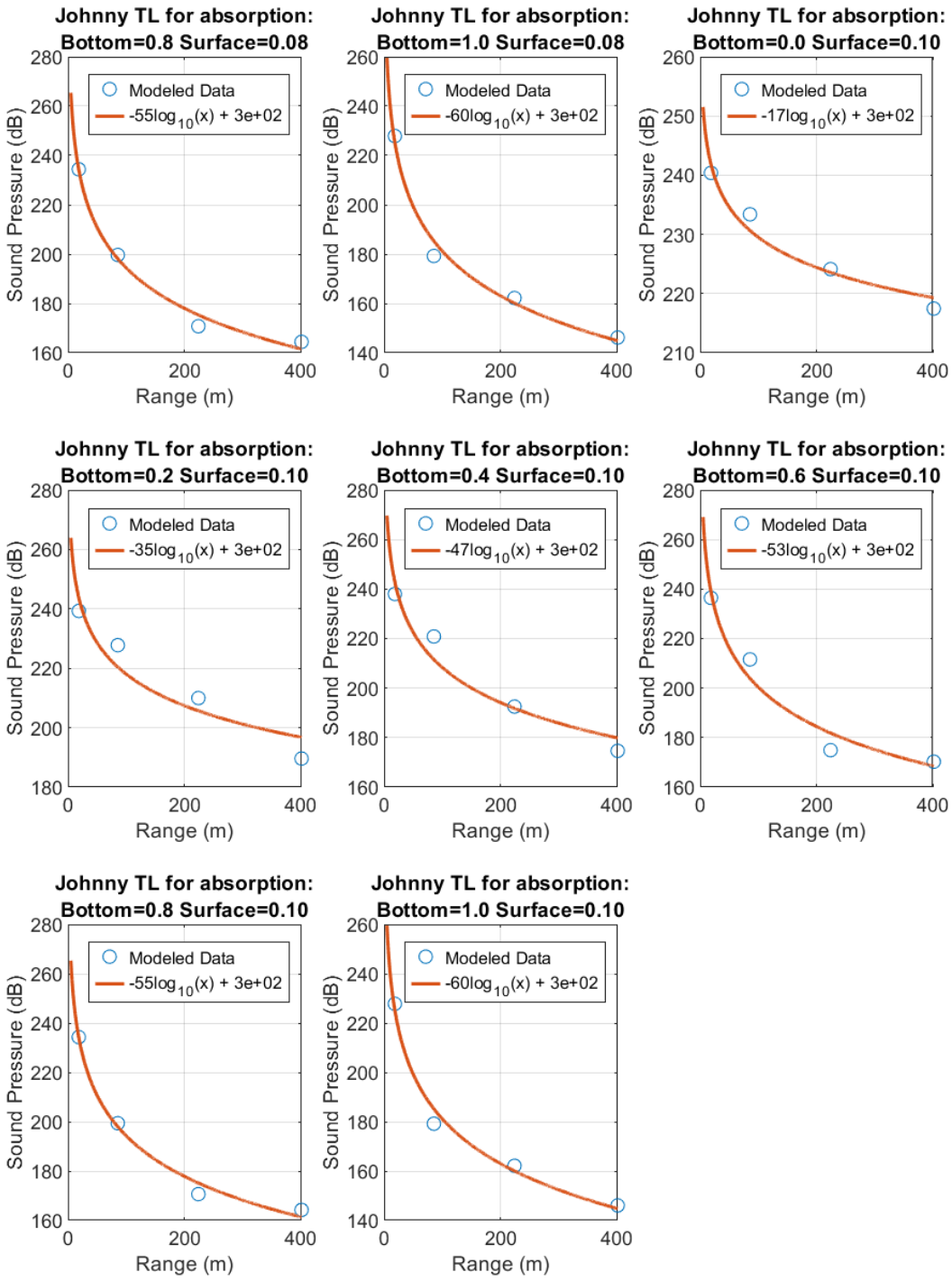

Figure B-15. John Sims Parkway TL curves for bottom and surface combinations 37 - 44

LIST OF REFERENCES

Acoustical Society of America. (2009). *Specification for Octave Band and Fractional Octave Band Analog and Digital Filter.* Melville, NY: ANSI S1. 11-2004.

Ainslie, M. A., Dahl, P. H., de Jonga, C. A., & Lawsc, R. M. (2014). Practical Spreading Laws: The Snakes and Ladders. *2nd International Conference and Exhibition on Underwater Acoustics*, 879-886.

Berube, J. (2019). *An analysis of hydro-acoustic transmission loss associated with marine pile driving. MS Thesis.* Jacksonville, FL.: University of North Florida.

Cepowski, T. (2020). ndCurveMaster 6.0. Sczecin, Poland.

Crowley, R., Berube, J., Matemu, C., Morgan, C., Kopp, B. T., Kernan, M., . . . Gelsleichter, J. J. (2020). Development of a Unique Instrumentation System to Monitor Underwater Noise Due to Pile Driving. *Geo-Congress*, 798-807.

Dawoud, W., Negm, A., Saleh, N., & Bady, M. (2016). Impact Assessment of Offshore Pile Driving Noise on Red Sea Marine Mammals. *International Journal of Enviromental Science and Development*, 10-15.

E.G., A., E., C., O.C., O., & W., S. (2017). *Rough Sea Surface Reflection Coefficient Estimation and Its Implication On Hyrdophone-Only Pre-Stack Deghosting.* PGS.

Farcas, A., & Thompson, P. M. (2015). Underwater noise modelling for enviromantal impact assessment. *Enviromental Impact Assessment Review 57*, 114-112.

FHWG (Fisheries Habitat Working Group). (2008). *Agreement in Principal for Interim Criteria for Injury to Fish from Pile Driving Activities.*

Hastrup, O. F., & Akal, T. (1980). *A Simple Formula to Calculate Shallow-water Transmission Loss By Means of a Least-Squares Surface Fit Technique.* La Spezia, Italy: North Atlantic Treaty Organization.

Jensen, F. B. (1981). Sound Propagation in Shallow Water: A detailed description of the acoustic field close to surface and bottom. *The Journal of Acoustical Society of America*, 1397-1406.

Jensen, F. B., William, K. A., Michael, P. B., & Schmidt, H. (2011). *Computatin Ocean Acoustics.* New York: Springer.

Kuperman, W. A. (1996). Acoustic Propagation Modeling in Shallow Water. *U.S. Navy Journal of Underwater Acoustics Vol. 46, No. 4*, 275-293.

Marsh, H. W., & Schulkin, M. (1962). Shallow-Water Transmission. *The Journal of the Acoustical Society of America 34*, 863-864.

NOAA. (2020, August 2). *National Centers for Enviromental Information*. Retrieved from Bathymetric Data Viewer: https://www.ncei.noaa.gov/maps/bathymetry/

Reinhall, P. G., & Dahl, P. H. (2011). *An Investigation of Underwater Sound Propagation from Pile Driving.* Seattle, Washington: Washington State Department of Transportation.

Reinhall, P. G., & Dahl, P. H. (2011). Underwater Mach wave radiation from impact pile driving: Theory and observation. *J. Acous. Soc. Am. 130 (3)*, 1209-1216.

Rogers, P. H. (1981). *Onboard Prediction of Propagation Loss in Shallow Water.* Washington, D.C.: Naval Research Laboratory.

Schulkin, M., & Mercer, J. A. (1985). *Colossus Revisited: A Review and Extension of the Marsh-Schulkin Shallow Water Transmission loss Model (1962).* Seattle: Applied Physics Laboratory University of Washington.

Tetra Tech, Inc. (2013). *Underwater Acoustic Modelling Report.* Glen Allen, Virginia: Tetra Tech, Inc.

Ville, V., Anti, H., Lars, L., Rhena, K., Jukka, T., Tuomas, S., & Timo, S. (2017). *CFD and CHA simulation of underwater noise induced by a marine propeller in two-phase flows.* Espoo, FInland: Fifth International Symposium on Marine Propulsors.

Wang, L., Heaney, K., Pangerc, T., Theobald, P., Robinson, S., & Ainslie, M. (2014). *Review of underwater propagation models.* Middlesex: Queen;s Printer and Controller of HMSO.

BIOGRAPHICAL SKETCH

Moses John Bosco is a graduate student at the University of North Florida College of Computing and Engineering. He graduated from the University of Dar es Salaam in November 2019 with a Bachelor of Science in Civil Engineering. After graduation, in January 2020 he was recruited as a graduate research assistant for the Taylor Engineering Research Institute at the University of North Florida. He has since been in the Master of Civil/Coastal Engineering program at the College of Computing and Engineering working under an FDOT project on Underwater Noise Due to Marine Pile Driving while in pursuit of his masters degree.